

The post-*Herschel* view of intrinsic AGN emission: constructing templates for galaxy and AGN emission at IR wavelengths

E. Bernhard,¹★ C. Tadhunter,¹ J. R. Mullaney,¹ L. P. Grimmer,^{1,2} D. J. Rosario³
and D. M. Alexander³.

¹*Department of Physics & Astronomy, University of Sheffield, Sheffield S3 7RH, UK*

²*Department of Statistics, School of Mathematics, University of Leeds, Leeds LS2 9JT UK*

³*Centre for Extragalactic Astronomy, Department of Physics, Durham University, South Road, Durham DH1 3LE, UK*

Accepted XXX. Received YYY; in original form ZZZ

ABSTRACT

Measuring the star-forming properties of AGN hosts is key to our understanding of galaxy formation and evolution. However, this topic remains debated, partly due to the difficulties in separating the infrared (i.e. 1–1000 μm) emission into AGN and star-forming components. Taking advantage of archival far-infrared data from *Herschel*, we present a new set of AGN and galaxy infrared templates, and introduce the spectral energy distribution fitting code `IRAGNSEP`. Both can be used to measure infrared host galaxy properties, free of AGN contamination. To build these, we used a sample of 100 local ($z < 0.3$), low-to-high luminosity AGNs (i.e. $L_{\text{bol}} \sim 10^{42-46} \text{ erg s}^{-1}$), selected from the 105-month *Swift*–BAT X-ray survey, which have archival *Spitzer*–IRS spectra and *Herschel* photometry. We first built a set of seven galaxy templates using a sample of 55 star-forming galaxies selected via infrared diagnostics. Using these templates, combined with a flexible model for the AGN contribution, we extracted the intrinsic infrared emission of our AGN sample. We further demonstrate that we can reduce the diversity in the intrinsic shapes of AGN spectral energy distributions down to a set of three AGN templates, of which two represent AGN continuum, and one represents silicate emission. Our results indicate that, on average, the contribution of AGNs to the far-infrared ($\lambda \gtrsim 50 \mu\text{m}$) is not as high as suggested by some recent work. We further show that the need for two infrared AGN continuum templates could be related to nuclear obscuration, where one of our templates appears dominated by the emission of the extended polar dust.

Key words: galaxies: active – methods: statistical – galaxies: Seyfert – galaxies: starburst – X-rays: galaxies

1 INTRODUCTION

Multiple lines of empirical evidence now suggest that the growth of supermassive black holes (SMBHs) at the centres of galaxies is connected to the growth of galaxies themselves (see Harrison 2017, for a review). For instance, a number of studies have shown that the redshift evolution of the star formation rate density of the Universe is closely related to that of the black hole accretion rate density, with both peaking at $z \sim 2$ and tracing each other, yet shifted by a factor of roughly 1500 (e.g. Aird et al. 2015). However, the precise connection between SMBH growth (observed as active galactic

nuclei, or AGN) and galaxy properties continues to be debated, in part due to contradictory results.

To better understand the connection between galaxies and AGNs, major efforts have focused on using the infrared (IR) part of the electromagnetic spectrum to measure the star-forming properties of AGN host galaxies. The reason for this is twofold. Firstly, the IR luminosity of a galaxy (i.e. integrated between 8 μm and 1000 μm ; L_{IR}) is believed to be a well-calibrated proxy of star formation rate (SFR) for star-forming galaxies (e.g. Kennicutt 1998). This is due to the ultraviolet (UV) light produced by young massive stars being re-processed by dust grains surrounding the star-forming regions within galaxies. Secondly, the thermal emission from the close proximity of AGNs (e.g. circumnuclear¹ torus) is, in theory, too hot to contaminate large portions of the IR spectrum, especially in the far-infrared (i.e. $\gtrsim 30 \mu\text{m}$; FIR; e.g. Rosario et al. 2012).

★ E-mail: e.p.bernhard@sheffield.ac.uk

The templates associated with this work are available in the supplementary material, or directly at <https://tinyurl.com/yawp96qc>. The SED fitting code `IRAGNSEP` is distributed via <https://pypi.org/project/iragnsep/>. We used the version 7.2.0 for this work.

¹ Here nuclear is used to refer to the central engine of the galaxy.

Nevertheless, the dust in the regions surrounding the AGN central engine can generate sufficient thermal emission at near-to-mid IR wavelengths to dominate over the host galaxy (e.g. [Smith et al. 2007](#); [Sales et al. 2010](#); [Lambrides et al. 2019](#)). In addition, some recent studies suggest that, in at least some cases, an AGN is able to heat dust on much larger scales (i.e. galactic scales), thereby generating thermal emission at longer wavelengths (i.e. $\lambda \gtrsim 80 \mu\text{m}$; e.g. [Tadhunter et al. 2007](#); [Schweitzer et al. 2008](#); [Dicken et al. 2009](#); [Mor et al. 2009](#); [Symeonidis et al. 2016](#)). Therefore, even in the FIR, AGN contamination potentially introduces a number of limitations and uncertainties when determining the star-forming properties of the host galaxies, which ultimately hampers the search for any connection between AGN and galaxy properties.

Recent studies have gone to some lengths in attempting to measure the properties of AGN host galaxies while accounting for AGN contamination. Some, for example, model the full (i.e. from UV to radio) spectral energy distribution (SED) of AGN host galaxies using several components that can each be attributed to either a galactic or a nuclear origin (e.g. [Noll et al. 2009](#); [Calistro Rivera et al. 2016](#); [Robotham et al. 2020](#); [Yang et al. 2020](#)). Often, however, these depend on modelled grids of templates to represent galaxy and AGN emission, which are idealised cases containing many free parameters, and hence subject to uncertainties and degeneracies.

An alternative approach involves focusing on the IR part of the spectrum and using empirical templates to account for any AGN contamination at these wavelengths. For example, [Mullaney et al. \(2011\)](#) constructed a set of empirical templates that represent galaxy and AGN emission at mid-to-far-IR wavelengths (i.e. $6 \mu\text{m}$ to $100 \mu\text{m}$), enabling the decomposition of the IR SED of AGN-hosting galaxies, and the subsequent measurement of the host galaxy SFR free of AGN contamination. To do this, they used a sample of typical X-ray AGNs (i.e. $L_X^{2-10} \sim 10^{42-44} \text{ erg s}^{-1}$, where L_X^{2-10} is the X-ray 2–10 keV luminosity) for which they had *Spitzer*–IRS spectra and *IRAS* photometry (i.e. photometry up to $100 \mu\text{m}$). The mean average AGN template of [Mullaney et al. \(2011\)](#) was found by extracting any excess in the flux observed in the IR SEDs of AGN-dominated sources once the host galaxy contribution had been removed. However, [Mullaney et al. \(2011\)](#) did not have access to wavelengths long-ward of $100 \mu\text{m}$, since at the time *Herschel*² data were not available. This is problematic, as these longer wavelengths are crucial to accurately probe the dust heated by star formation (e.g. [Ciesla et al. 2015](#)). In addition, the spatial resolution of *IRAS* data used by [Mullaney et al. \(2011\)](#) is roughly 20 times worse than that of *Herschel* at similar wavelengths, potentially leading to contamination from neighbouring sources.

More recently, using *Herschel* data, [Symeonidis et al. \(2016\)](#) suggested that AGN emission is cooler (and thus contributes more strongly to the FIR) than previously found. These findings could alter significantly the SFRs measured from FIR observations of AGN-hosting galaxies, and therefore greatly impact our understanding of AGN–galaxy co-evolution. However, we stress that the method used in [Symeonidis et al. \(2016\)](#) to derive their template is controversial, and that inconsistencies with other observations have been pointed out in several studies (e.g. [Lani et al. 2017](#); [Lyu & Rieke 2017](#); [Stanley et al. 2018](#); [Schulze et al. 2019](#)). Instead, some studies that use *Herschel* (e.g. [Lani et al. 2017](#); [Lyu & Rieke 2017](#); [Xu et al. 2020](#)) report an AGN contribution to the FIR that is similar to that

obtained by [Mullaney et al. \(2011\)](#). Most of these studies, however, focus on optically bright quasars (QSOs), which are extreme sources and do not represent the majority of the AGN population.

Here, we built upon the work of [Mullaney et al. \(2011\)](#) by constructing a new library of templates for galaxy and AGN emission at IR wavelengths that can be applied to more typical AGNs. With the availability of *Herschel* data, we can now decompose the IR SEDs into AGN and galaxy components without having to extrapolate the FIR from shorter wavelengths, as in [Mullaney et al. \(2011\)](#). In §2 we describe how we selected our sample and constructed SEDs of X-ray-selected AGNs for which we have mid-IR (MIR) spectra and FIR photometry. We then present in §3 how we defined a set of templates for the IR emission of non-AGN galaxies that we then fit to our sample of AGN IR SEDs, in doing so extracting the AGN components which we then used to define a set of templates for the IR emission of AGNs. In §4 we compare our AGN templates to those reported in previous studies and discuss some aspects of our new library of AGN templates. Finally, we present our conclusions in §5. Throughout, we adopted a WMAP–9 year cosmology ($H_0 = 69.33 \text{ km s}^{-1} \text{ Mpc}^{-1}$, $\Omega_\Lambda = 0.712$, $\Omega_b = 0.0472$, $\Omega_c = 0.2408$; [Hinshaw et al. 2013](#)) and a [Chabrier \(2003\)](#) initial mass function when calculating galaxy properties.

2 SAMPLE SELECTION AND DATA DESCRIPTION

2.1 X-ray data

To investigate the typical IR emission of AGNs and that of their host galaxies, we used a sample of X-ray AGNs selected from the 105-month *Swift*–BAT all-sky hard X-ray survey of [Oh et al. \(2018\)](#). The Burst Alert Telescope (BAT) on board the *Swift* gamma-ray burst space observatory ([Gehrels et al. 2004](#)) is conducting a uniform all-sky survey at energies 14–195 keV to unprecedented sensitivities (e.g. 90 per cent of the sky to a depth of $8.40 \times 10^{-12} \text{ erg s}^{-1} \text{ cm}^{-2}$). Although the mission was not specifically designed for AGNs (see [Barthelmy et al. 2005](#) for the mission primary goal), the energies covered by *Swift*–BAT correspond to those emitted by AGNs at wavelengths almost free from absorption. This, combined with the all-sky survey strategy, provides one of the best opportunities to define a clean sample of mostly low redshift AGNs. By cross-matching the hard X-ray detections with archival data at various wavelengths (i.e. from softer X-ray to optical), [Oh et al. \(2018\)](#) have been able to robustly classify the *Swift*–BAT sources into different types (see Table 1 in [Oh et al. 2018](#)).

Out of the 1632 sources reported in [Oh et al. \(2018\)](#), we retained Seyfert galaxies (819 sources), LINERs (6 sources), and unknown AGNs (114 sources)³. All other classes, including beamed AGNs, such as Blazars and flat-spectrum radio quasars, were discarded to avoid complications arising from the potential non-thermal contamination to the FIR⁴. In addition, after visual inspection, we removed Cygnus A which was the only source that

³ Unknown AGNs are X-ray sources associated with galaxies whose optical spectra and type classifications are not known (see [Oh et al. 2018](#)).

⁴ Discarded classes were: Unknown class I, Unknown class II, Unknown class III, Multiple, Galactic centre, Galaxy Cluster, Beamed AGN (Blazar/FSRQ), Cataclysmic Variable Star (CV), Symbiotic Star, Other Star, Open Star Cluster, Starburst Galaxy, Compact Group of Galaxies, Pulsar, Supernova Remnant (SNR), Nova, High Mass X-ray Binary (HMXB), Low Mass X-ray Binary (LMXB), Other X-ray Binary (XRB), Globular Cluster (GC), Molecular Cloud, and Gamma-ray Source.

² *Herschel* is an ESA space observatory with science instruments provided by European-led Principal Investigator consortia and with important participation from NASA.

showed obvious non-thermal contamination in the FIR. We therefore retained 938 hard-X-ray selected AGNs which constitute our parent sample, the redshifts of which span $0 < z < 4.7$, as reported by the NASA/IPAC Extragalactic Database⁵ (NED) or the SIMBAD (Wenger et al. 2000) database (Oh et al. 2018).

2.2 IR data

2.2.1 Far-IR photometry

We used FIR photometry (i.e. $70 \mu\text{m} < \lambda_{\text{obs}} < 500 \mu\text{m}$) to characterise the cold dust emission of our sample of AGNs. As we will perform SED fits to separate out the AGN contribution (see § 3.2.2), we aimed to obtain at least three FIR photometric measurements (considering 3σ detections), in addition to the *Spitzer*-IRS spectra characterising the MIR emission of our AGN sample (see § 2.2.2 for the MIR spectra). The Highly Processed Data Products^{6,7} (HPDPs) provide the most complete and uniform database of reduced fluxes for both the PACS (covering the $70 \mu\text{m}$, $100 \mu\text{m}$, and $160 \mu\text{m}$ bands; Poglitsch et al. 2010; Marton et al. 2017) and SPIRE (covering the $250 \mu\text{m}$, $350 \mu\text{m}$, and $500 \mu\text{m}$ bands; Griffin et al. 2010; Schulz et al. 2017) instruments on-board the *Herschel* Space Observatory (Pilbratt et al. 2010).

We identified FIR counterparts to the X-ray selected AGNs by cross-matching their positions using a $5''$ matching radius. We found 112 sources out of the 938 of our parent sample that followed our criteria for SED fits. However, we also found that the HPDP point source catalogues largely failed to recognise the extended nature of sources, in particular at $z \lesssim 0.3$, where our final AGN sample lies (see § 2.3 for the properties of our final AGN sample). As a consequence, the vast majority of our sources suffered from under-estimated fluxes in the HPDPs, since they had been regarded as point sources in their reduction.

To obtain accurate fluxes (i.e. accounting for extended emission, where necessary), we used *Herschel*-PACS and *Herschel*-SPIRE images from the “*Herschel* high level images” products of the NASA/IPAC Infrared Science Archive (IRSA) database (see Appendix A for more details on the images). The *Herschel* fluxes for extended sources were calculated following the method presented in Appendix A, and are reported in Table C2. Overall, we found that 30 per cent, 20 per cent, 55 per cent, 62 per cent, 58 per cent, and 45 per cent of our sources have been misclassified as point sources in the HPDPs at $70 \mu\text{m}$, $100 \mu\text{m}$, $160 \mu\text{m}$, $250 \mu\text{m}$, $350 \mu\text{m}$, and $500 \mu\text{m}$, respectively. Some fluxes showed up to a factor of 10 increase after accounting for the spatially extended emission. We also found very good agreements between our fluxes and those calculated for extended sources reported in Meléndez et al. (2014) and Shimizu et al. (2016) for *Herschel*-PACS and *Herschel*-SPIRE, respectively, for the 93 per cent of our sample which overlap with theirs (see Fig. A2).

⁵ The NASA/IPAC Extragalactic Database (NED) is operated by the Jet Propulsion Laboratory, California Institute of Technology, under contract with the National Aeronautics and Space Administration.

⁶ The explanatory supplements for the PACS point source catalogue can be found at http://archives.esac.esa.int/hsa/legacy/HPDP/PACS/PACS-P/PPSC/HPPSC_Explanatory_Supplement_v2.2.pdf

⁷ The explanatory supplements for the SPIRE point source catalogue can be found at <http://archives.esac.esa.int/hsa/legacy/HPDP/SPIRE/SPIRE-P/SPSC/SPIREPointSourceCatalogExplanatorySupplementFull20170203.pdf>

2.2.2 mid-IR spectra

As AGN-heated dust is expected to radiate significantly at MIR wavelengths, we completed the IR coverage using *Spitzer*-IRS low resolution spectra (Houck et al. 2004). The *Spitzer*-IRS is made of two separate low resolution spectrograph modules, Short-Low (SL) and Long-Low (LL), covering wavelengths from $5.3 \mu\text{m}$ to $38 \mu\text{m}$, and for which the resolution ranges between $R = \lambda/\Delta\lambda \sim 90$ –600 depending on wavelength (with shorter wavelengths having higher spectral resolution). Each of the SL and LL modules is also divided into two sub-slits SL1/SL2 and LL1/LL2 covering different wavelength ranges within the aforementioned full wavelength range (see Table 1 in Houck et al. 2004 for the properties of the *Spitzer*-IRS). When a source is observed within the sub-slits of the second order, a short section of the first order is also illuminated. Therefore, the *Spitzer*-IRS offers bonus orders at wavelengths $7.3 \mu\text{m}$ to $8.7 \mu\text{m}$ and $19.4 \mu\text{m}$ to $21.7 \mu\text{m}$ for the SL and the LL modules, respectively. These were used to improve the overlap between the first and the second orders.

The *Spitzer*-IRS spectra of all 112 of the sources in our sample that also have at least three *Herschel* FIR measurements (see § 2.2.1 for the *Herschel* photometry) were extracted from the Combined Atlas of Sources with *Spitzer*-IRS Spectra (CASSIS; Lebouteiller et al. 2011). The CASSIS pipeline offers post-basic calibrated data that can handle a large variety of sources, from barely detected to bright sources, and from point sources to extended sources (see Lebouteiller et al. 2010 for details on the tools used by CASSIS). From the CASSIS database, we downloaded the optimal spectrum for each of our AGNs that have been observed with *Spitzer*-IRS. This included optimal point source extraction for unresolved sources, and tapered column source extraction for extended sources (see Lebouteiller et al. 2010 for more details on the source extraction method).

2.3 Observed IR SEDs of AGNs

To produce observed IR SEDs we combined the *Spitzer*-IRS spectra with the *Herschel* photometry. To do this, we first corrected for flux mismatch between the SL and LL arms of the *Spitzer*-IRS spectra due to the different slit widths⁸ (the slit widths of SL1 and SL2 are $3.7''$ and $3.6''$, respectively, and those of LL1 and LL2 are $10.7''$ and $10.5''$, respectively). As the LL slit width is larger, and hence likely to contain more light from the host galaxy, we renormalised the fluxes in the SL arm to ensure continuity between the two arms. This method is referred to as stitching. To do this we fit independently smoothed splines to the two arms, and interpolated at $14 \mu\text{m}$, which corresponds to the wavelength at which the two arms connect. We then calculated the correction needed for the SL arm to join the LL arm. As the presence of large polycyclic aromatic hydrocarbon (PAH) features can challenge the accuracy of the spline fitting, we visually inspected each of the stitched spectra, and corrected roughly half of the sample by a few per cent to increase the stitching accuracy. Overall, we found a median correction factor of 1.10, with a maximum of a factor of five.

The full observed IR SED of each source was obtained by combining the *Spitzer*-IRS spectra with the *Herschel* photometry. To assess the overall normalisation of the spectra, we collected

⁸ The strategy adopted by the CASSIS team was to reduce independently the two arms of the spectrograph. Therefore, the connection between the SL and LL spectra is not guaranteed since slit losses can arise within the narrower slit (i.e. the SL arm).

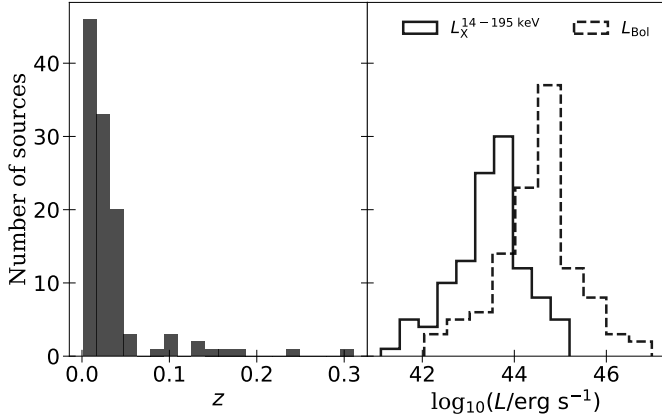


Figure 1. The redshift (left-hand panel), the *Swift*–BAT X-ray 14–195 keV luminosity (right-hand panel; continuous line distribution), and the bolometric luminosity (right-hand panel; dashed line distribution) distributions of our final sample of 112 AGNs. The latter is typical of low-to-high luminosity AGNs in the local Universe.

archival *Spitzer*–MIPS 24 μm fluxes, only considering those derived accounting for the spatially extended flux (~ 70 per cent of our sample), and compared to the synthetic 24 μm *Spitzer*–MIPS flux (calculated by convolving the synthetic *Spitzer*–MIPS 24 μm filter with the *Spitzer*–IRS spectra). We found that, on average, the observed 24 μm photometry was ~ 4 per cent lower than the synthetic photometry. Therefore, we corrected the spectra of those sources for which we had a corresponding 24 μm photometry measurement, but did not apply any corrections to the rest of the sample since the typical correction factor is negligible.

The main properties of the 112 sources in our AGN sample are reported in Table C1. We note that the sample is typical of local (i.e. $z < 0.3$, but the vast majority of the sample lies at $z < 0.1$) low-to-high luminosity AGNs with $L_X^{14-195} \sim 10^{41-45} \text{ erg s}^{-1}$ (where L_X^{14-195} is the *Swift*–BAT X-ray 14–195 keV luminosity). This roughly corresponds to bolometric luminosities of $L_{\text{bol}} \sim 10^{42-46} \text{ erg s}^{-1}$, after using the photon indices reported in Oh et al. (2018) to convert L_X^{14-195} to L_{bol} . We show in Fig 1 the redshift, *Swift*–BAT luminosity, and bolometric luminosity distributions of our AGN sample. We note that our sample could be biased toward bright IR sources since we required *Herschel* detections. In Fig. 2 we show all⁹ our SEDs normalised at rest-frame 40 μm . We note in particular the large diversity in the IR SEDs of our sample of AGNs, and that some are clearly flatter in the MIR, suggesting AGN-dominated MIR sources.

3 BUILDING LIBRARIES OF TEMPLATES FOR GALAXY AND AGN EMISSION

In this section we describe how we built sets of templates which are representative of galaxy and AGN emission at IR wavelengths. To do this, we first selected a clean sample of 55 star-forming galaxies with *Spitzer*–IRS spectra and *Herschel* photometry (see § 3.1.1), from which we extracted seven different galaxy templates that capture the full diversity of this sample of star-forming galaxies

⁹ An extra 10 AGN SEDs are not shown as they will be removed from the sample after their fits revealed some discrepancies between the *Spitzer*–IRS spectra and the *Herschel* photometry (see § 3.2.2).

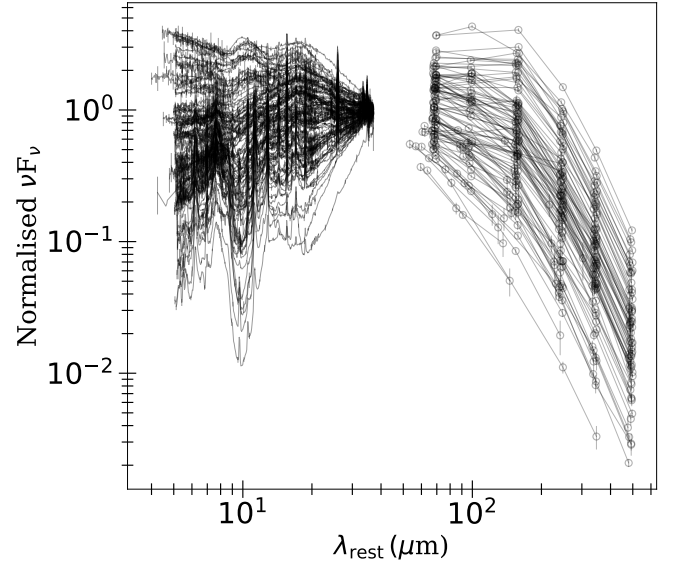


Figure 2. The IR SEDs of our full AGN sample normalised at 40 μm . These were obtained by combining the low resolution *Spitzer*–IRS spectra with corresponding *Herschel* photometry. The latter has been corrected for spatially extended emission that was largely missed in the HPDPs. The thin lines show a linear interpolation between points and serve only to guide the eyes. We note that there is a large diversity in the IR SEDs of AGNs, once normalised at 40 μm .

(see § 3.1.4). By then fitting our sample of 112 AGN SEDs (see § 3.2.2) with each of these galaxy templates and a flexible model for AGN emission (see § 3.2.1), we extracted three AGN IR templates (see § 3.2.3).

3.1 IR templates for galaxy emission

3.1.1 Sample of IR SEDs for star-forming galaxies

As previously mentioned, we carefully built a set of templates to represent galaxy emission at IR wavelengths. To do this we required a set of galaxy-dominated SEDs. Our starting point was the work from Lambrides et al. (2019), who have recently classified 2015 *Spitzer*–IRS spectra according to whether they are star-forming or AGN-dominated by using the equivalent width of the PAH emission feature at 6.2 μm ($\text{EW}_{6.2\mu\text{m}}^{\text{PAH}}$). The strength of the 6.2 μm emission feature is thought to be related to the level of star formation (e.g. Peeters et al. 2004). In the presence of an AGN, the dust heated in the central region of the galaxy enhances the underlying continuum and therefore reduces the equivalent width of the 6.2 μm feature (e.g. Nenkova et al. 2008). As a consequence, the $\text{EW}_{6.2\mu\text{m}}^{\text{PAH}}$ is thought to be a good indicator of the level of AGN contribution, at least at wavelengths close to 6 μm (e.g. Armus et al. 2007; Spoon et al. 2007; Lambrides et al. 2019).

We retained all the sources in Lambrides et al. (2019; hereafter L19) that had $\text{EW}_{6.2\mu\text{m}}^{\text{PAH}} > 0.54 \mu\text{m}$, where $\text{EW}_{6.2\mu\text{m}}^{\text{PAH}} = 0.54$ corresponds to the average value found for pure starburst galaxies (Armus et al. 2007). Above this threshold, the MIR emission of galaxies is thought to be fully dominated by star-forming processes. Amongst the 2015 sources in L19, we found 464 that satisfy this criterion (see Fig 3). However, as measuring $\text{EW}_{6.2\mu\text{m}}^{\text{PAH}}$ is challenging (e.g. the continuum must be estimated), we double-checked the values of $\text{EW}_{6.2\mu\text{m}}^{\text{PAH}}$ by cross-matching our pre-selected sample of 464 star-

forming galaxies with the sample of [Samsonyan et al. \(2016\)](#) – who have compiled $EW_{6.2\mu m}^{PAH}$ measurements from [Sargsyan et al. \(2011\)](#), [Stierwalt et al. \(2014\)](#), and the CASSIS database – finding, in total, 107 overlapping sources. In doing so, we found 53 ambiguous sources that were classified as star forming in L19, and as composite or AGN-dominated in [Samsonyan et al. \(2016\)](#). These 53 were discarded from our pre-selected sample of pure star-forming galaxies, leaving a sample of 411 star-forming galaxies selected purely on $EW_{6.2\mu m}^{PAH}$.

As recent evidence suggests that some AGNs can show $EW_{6.2\mu m}^{PAH}$ typical of star-forming galaxies (e.g. L19), we further used IR colour selection to discard other potential AGNs from our pure star-forming sample. Following [Assef et al. \(2013\)](#), AGNs can be separated from star-forming galaxies using the WISE W1 ($3.4\mu m$) and W2 ($4.6\mu m$) colours. We used the criterion from [Assef et al. \(2013\)](#) which guarantees 90 per cent completeness and ~ 80 per cent reliability at the W2 magnitudes of our sample (typically $W2 < 15$ mag; L19), and only retained sources with $W1 - W2 \leq 0.5$ (see Fig 3). The main caveat of such a selection is that we potentially retain 10 per cent of AGNs in the sample of pre-selected star-forming galaxies, as a corollary of the 90 per cent completeness reported in [Assef et al. \(2013\)](#). However, we stress that after fitting the SEDs, we will carefully discard the excess of AGNs found in the star-forming sample selected purely based on the $EW_{6.2\mu m}^{PAH}$ and the WISE colours (see § 3.1.3).

By using WISE colours we discarded 139 galaxies out of the 411 galaxies that were selected based purely on their $EW_{6.2\mu m}^{PAH}$. In addition, by considering archival K-band magnitudes, *Spitzer*-IRAC, and *Spitzer*-MIPS fluxes from L19, we also discarded one extra source which does not pass the IR colour “KIM” criterion of [Messias et al. \(2012\)](#). Finally, we discarded two more sources that were detected by *Swift*-BAT. After making the aforementioned cuts, we were left with a total 269 galaxies in our pre-selected sample of star-forming galaxies.

Amongst the 269 pre-selected star-forming galaxies, we only retained 110 that have *Spitzer*-IRS spectra and at least three *Herschel* photometric measurements from the HPDPs. As for our AGN sample, we subsequently updated the *Herschel* fluxes to account for spatially extended emission (see § 2.2.1 and Appendix A for the extended emission). The Table C4 presents some basic properties of this sample of 110 galaxies, and the Table C5 reports the *Herschel* fluxes. We show in Fig. 3 the $EW_{6.2\mu m}^{PAH}$ of our full sample of 110 pre-selected star-forming galaxies plotted against the WISE colours. The galaxy sample extends to $z \sim 1$, although most sources lie at $z < 0.3$, which is similar to that of our AGN sample (see § 2.3). To combine the *Spitzer*-IRS spectra with the *Herschel* photometry we repeated the process outlined in § 2.3.

3.1.2 Prescriptions for IR obscuration

In order to perform SED fits, we estimated the level of IR obscuration affecting the observed SEDs of our galaxies. First, we must assume a dust opacity curve which provides the relative level of obscuration per unit wavelength. We note that, in addition to significant disagreements between curves derived for the local ISM or for the Galactic centre (e.g. [Chiar & Tielens 2006](#)), disagreements are found amongst curves for the local ISM (e.g. [Kemper et al. 2002](#); [Min et al. 2007](#)). We show in Fig. 4 a number of these curves, in addition to that used in PAHfit ([Smith et al. 2007](#)), which is a fitting routine for the *Spitzer*-IRS spectra, and for which the attenuation

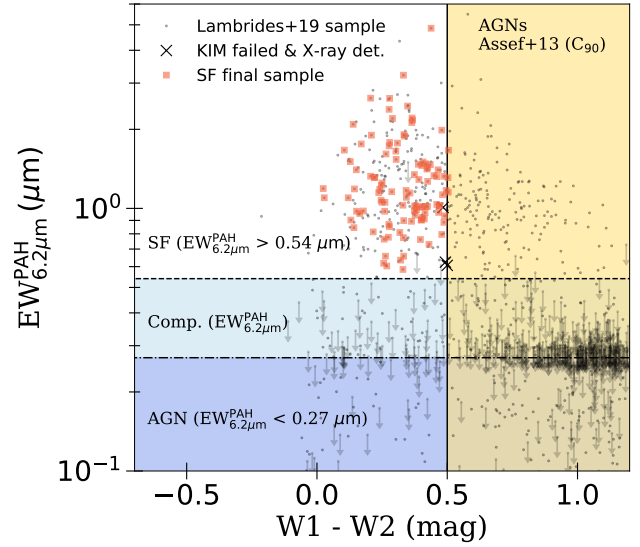


Figure 3. The $EW_{6.2\mu m}^{PAH}$ versus the WISE colours $W1 - W2$ of the sample from L19 (grey dots). The arrows indicate upper limits on $EW_{6.2\mu m}^{PAH}$. For clarity, we only show the top-left part of the full parameter space covered by the 2,015 sources from L19, where star-forming galaxies lie. Our sample of 110 pre-selected star-forming galaxies was first selected based on $EW_{6.2\mu m}^{PAH}$, where sources below the dot-dashed line are AGNs, sources above the dashed line are star-forming galaxies, and sources between these lines are composite galaxies. The values employed to define these limits are from [Armus et al. \(2007\)](#); see text). We then employed the WISE colour selection criterion of [Assef et al. \(2013\)](#), shown with a vertical black line, where star-forming galaxies lie on the left-hand side of this line. In addition, one source was discarded as it failed the MIR KIM test of [Messias et al. \(2012\)](#), and two sources were discarded since detected by the *Swift*-BAT (black crosses). The red squares show our final sample of 110 pre-selected star-forming galaxies with *Spitzer*-IRS spectra and at least three *Herschel* photometric measurements.

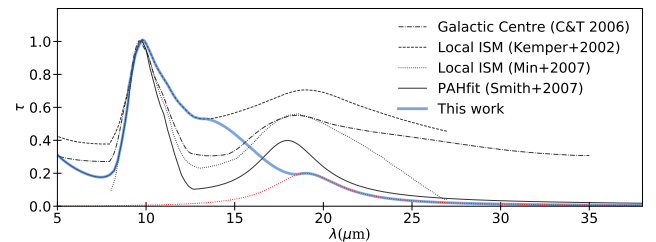


Figure 4. Dust opacity per unit wavelength (extinction curves) normalised at $9.7\mu m$, and derived for the Galactic centre ([Chiar & Tielens 2006](#), C&T 2006 in keys), for the local ISM ([Kemper et al. 2002](#); [Min et al. 2007](#)), and from PAHfit ([Smith et al. 2007](#)), as indicated in the top-right keys. The pseudo-extinction curve adopted in this work is shown with a thick blue line, and is a combination of several of these curves (see text). The dotted red line shows the re-scaled and shifted extinction curve from PAHfit reflecting the relative extinction at $18\mu m$ observed in our sample of star-forming galaxies.

curve has been derived from a combination of several curves (see [Smith et al. 2007](#) for details).

We found that none of these curves provided a satisfactory model for obscuration amongst our star-forming galaxies while fitting their SEDs (see § 3.1.3 for the fits). In particular, we noted an excess of model flux around $\sim 13\mu m$ while using the attenuation curve of PAHfit. Instead, the extinction curve of [Chiar & Tielens](#)

(2006), which had a higher level of obscuration around $\sim 13 \mu\text{m}$, provided a better fit at these wavelengths, but a deficit of model flux at longer wavelengths, when compared to observations. To reconcile these, we derived our own fully empirically-motivated extinction curve. While we assumed that the discrepancies between the observed and the model fluxes, corrected for extinction, were due to the lack of a universal extinction law, we stress that the models of galaxies used to fit our SEDs have not been calibrated against MIR spectral observations. The latter could, to some extent, also explain the discrepancies between the observed and the model fluxes. However, we note that the galaxy templates used to fit our SEDs have been successfully tested against the stacked *Spitzer*–IRS spectra of luminous and ultra-luminous IR galaxies at $z = 1$ and $z = 2$, respectively (Schreiber et al. 2018, see § 3.1.3 for the galaxy templates). Our extinction curve uses a combination of that from PAHfit and Kemper et al. (2002). At wavelengths longer than $15 \mu\text{m}$, we renormalised the extinction curve of PAHfit to match the apparent obscuration measured in our sample of galaxies, and we shifted the silicate absorption peak from $18 \mu\text{m}$ to $19 \mu\text{m}$ (see Fig. 4). We refer to this extinction curve as “pseudo-extinction curve”, as it is fully empirically motivated, and can potentially be related as much to the model used to fit our SEDs (see § 3.1.3 for the fits) as to the properties of the obscuring dust.

With the extinction curve defined, we must estimate the total amount of obscuration within the galaxy. We have that,

$$F_{\nu}^{\text{Obs}} \equiv F_{\nu}^{\text{Int}} \times \Theta(\tau_{\lambda}), \quad (1)$$

where F_{ν}^{Obs} and F_{ν}^{Int} are the observed (i.e. attenuated) and intrinsic (i.e. unattenuated) flux densities, and $\Theta(\tau_{\lambda})$ is the total attenuation at wavelength λ given the optical depth τ_{λ} . For the galaxy, we assumed a slab of uniformly mixed stars and dust (e.g. Li & Draine 2001; Smith et al. 2007). Therefore, for an observer looking perpendicular onto the screen, and in the case of pure absorption, the solution to the transfer equation leads to (e.g. Krügel 2009),

$$\Theta(\tau_{\lambda}) = \frac{(1 - e^{-\tau_{\lambda}})}{\tau_{\lambda}}. \quad (2)$$

We refer the reader to § 3.2.2 for the treatment of the AGN obscuration, as the assumption of a uniformly mixed medium breaks.

To estimate $\Theta(\tau_{\lambda})$ and correct the full SED, we first calculated the total attenuation at $9.7 \mu\text{m}$, $\Theta(\tau_{9.7})$, using the silicate absorption feature observed at that wavelength. To determine the unabsorbed flux at $9.7 \mu\text{m}$, we fit a first-order spline to the observed continuum at rest wavelengths $6.8 \mu\text{m}$ and $30 \mu\text{m}$, which shows minimum obscuration (see Fig. 4). The total attenuation at $9.7 \mu\text{m}$, $\Theta(\tau_{9.7})$, was therefore given by the ratio between the observed to the intrinsic flux at that wavelength ($F_{9.7 \mu\text{m}}^{\text{Obs}} / F_{9.7 \mu\text{m}}^{\text{Int}}$ in Eq. 1). The latter was inferred from the fit to the estimated continuum. We stress that this does not provide the *exact amount* of full obscuration, as the continuum is estimated using wavelengths that are themselves slightly affected by obscuration. Despite this, we find that it provides an overall good estimate, based on the goodness of the SED fits (see § 3.1.3).

Since we have that,

$$\Theta(\tau_{9.7}) = (1 - e^{-\tau_{9.7}}) / \tau_{9.7} \equiv F_{9.7 \mu\text{m}}^{\text{Obs}} / F_{9.7 \mu\text{m}}^{\text{Int}}, \quad (3)$$

then the optical depth at $9.7 \mu\text{m}$, $\tau_{9.7}$, was calculated using interpolation on a log-grid in steps of 0.01. Once $\tau_{9.7}$ was measured, we used the aforementioned pseudo-extinction curve to calculate the obscuration at all IR wavelengths.

3.1.3 Fit to the IR SEDs for star-forming galaxies

Our approach to building a set of typical IR templates for non-AGN-hosting galaxies is based on the work of Schreiber et al. (2018, hereafter S18; and references therein). S18 provide two independent grids of IR templates, each varying with dust temperature, T_{dust} , and corresponding to different emission mechanisms present in star-forming galaxies. The first grid represents large and small grain emission (hereafter dust continuum), where the amorphous carbon dust models of Galliano et al. (2011) were adopted, with the mass-fraction of thermalised carbonated to silicate grains fixed to the Milky Way value, and the mass fraction of the non-thermalised silicate grains fixed to zero (see § 3.1.1 in S18).

The second grid is used to model the PAH features, and was also adopted from Galliano et al. (2011), with the fraction of neutral-to-ionised molecules fixed to the Milky Way value (see § 3.1.2 in S18). The free parameter in each of these models is the radiation intensity, U , and composite SEDs have been built by assuming a distribution for U , as in Dale et al. (2001; see § 3.1.3 in S18). However, for simplicity, S18 fixed the relative contributions of intensities U (i.e. $\alpha_{\text{SF}} = 2.6$, where α_{SF} is the power law index of the distribution of U), and was left with a single parameter (T_{dust}) to control the shape of their SEDs, split in terms of PAH and dust continuum emission¹⁰.

Using this two-component model, S18 found that it is possible to reliably fit the stacked IR broadband SEDs (i.e. not including *Spitzer*–IRS spectra) of Main Sequence galaxies (i.e. typical star-forming galaxies observing a relationship between stellar mass and SFR, e.g. Schreiber et al. 2015), split in terms of redshifts and stellar masses, out to $z \sim 5$. In addition, S18 showed that this two-component model was able to fit starburst galaxy SEDs, which are galaxies experiencing a burst of star formation, and located above the MS at a given stellar mass and redshift. However, we could not use the S18 galaxy templates directly on our AGN sample because of the large number of templates, making it difficult to achieve convergence and avoid degeneracies while fitting the SEDs of AGN-hosting galaxies. To overcome this, we first used the S18 galaxy templates to fit the 110 SEDs of our pre-selected star-forming galaxy sample, and extracted a smaller, more representative set of galaxy IR templates. As we describe later in § 3.2, these templates were then used, together with a flexible model for AGN emission, to fit our sample of AGN SEDs.

The fits of S18 templates to our star-forming SEDs were performed using maximum likelihood estimation¹¹ (MLE). We incorporated the possibility of including flux upper limits in the fit so that we were able to replace the *Herschel* flux at $160 \mu\text{m}$ for galaxies at $z < 0.3$ with an upper-limit. We did this as at $z < 0.3$ the *Herschel*–PACS band at $160 \mu\text{m}$ could be contaminated by the [C II] emission line at $158 \mu\text{m}$ which can be strong in star-forming galaxies (e.g. Smail et al. 2011). Because our likelihood function includes upper limits it could not be maximised analytically. Instead, we maximised it by randomly sampling the posterior distribution of each parameter, using the affine invariant ensemble sampler of Goodman & Weare (2010) fully implemented into EMCEE¹² (Foreman-Mackey

¹⁰ The templates can be found at: <https://github.com/cschreib/s17-irlib>

¹¹ Because our SEDs include *Spitzer*–IRS spectra and *Herschel* photometry, we weighted the spectral data so that the MIR and the FIR part of the SEDs were equally fit. The weights corresponded to the inverse of the number of points in the spectrum.

¹² EMCEE is publicly available at <https://emcee.readthedocs.io/en/v3.0.2/>

et al. 2013). The median values of the posterior distributions were taken as the best-fitting parameters, and the standard deviations as their 1σ uncertainties.

We fit our sample of 110 IR SEDs of star-forming galaxies, including *Spitzer*–IRS spectra, using the combination of the dust grain continuum and the PAH emission templates of S18, independently adjusting the normalisation and the dust temperature of each of the two components. Prior to the fits, we affected the dust continuum templates by obscuration following the prescriptions presented in § 3.1.2. In fact, better fits were obtained when the PAH templates were left free of obscuration. This is in agreement with recent work providing evidence that PAHs are from more diffuse and less dense regions (e.g. Hirashita et al. 2020).

In the top panel of Fig. 5 we show an example of a best SED fit, separated between the dust continuum (dashed red line) and the PAH emissions (dot-dashed green line). However, we found that the model of S18 was able to satisfactorily fit 50 per cent of our sample of pre-selected star-forming galaxies. For the rest of the sample, significant discrepancies between the observed SEDs and the models were noted, as shown for MCG-02-01-051 in the bottom panel of Fig. 5. In particular, the majority of the failed fits were showing a MIR excess and a shallower MIR slope, which could be due to mild AGN contamination (see the filled orange area in Fig 5).

For the 50 per cent of sources that could not be fit using the model of S18, we inspected their SEDs and searched the NED database to find potential evidence for misclassification. The full analysis is presented in Appendix B (see also Table C4). Briefly, in addition to finding sources that had intrinsic issues with their SEDs (e.g. FIR fluxes contaminated by companion galaxies), the vast majority (i.e. ~ 60 per cent of the badly fit sources) showed AGN contribution to the MIR. The AGN contributions to the total IR luminosities (i.e. integrated from $8\ \mu\text{m}$ to $1000\ \mu\text{m}$) were found to be typically below ~ 10 – 20 per cent, as revealed via SED fitting (Magdis et al. 2013; Vika et al. 2017), or by combining multiple MIR diagnostics (Díaz-Santos et al. 2017; see Appendix B for more details). We note that these were identified mostly via SED fits, which in turns depend on the models used to fit the SEDs. However, by looking at the individual SEDs, we noted the presence of multiple faint high-ionisation emission lines, such as [NeV] at $24\ \mu\text{m}$ and [OIV] at $26\ \mu\text{m}$, in half of the galaxies that were poorly fit by the model of S18. This strongly suggests the presence of an AGN. Nevertheless, we cannot exclude the possibility that, at least for some of these SEDs, the reported AGN contributions result from fits based on photometric measurements affected by systematics.

We further stress that we preferred not to directly pre-select our star-forming sources in § 3.1.1 using these results as (1) the AGN fractions were often low and consistent with zero once the uncertainties accounted for, (2) we found some large discrepancies between the AGN fractions reported for the same source across studies (i.e. sometimes up to ~ 60 per cent differences), and (3) we found some SEDs with ambiguous AGN fractions reported in previous work that could be fit with the model of S18, and that would have been otherwise discarded. Instead, we preferred to keep our pre-selection based on the $\text{EW}_{6.2\mu\text{m}}^{\text{PAH}}$ and the WISE colours, and discard the sources that could not be fit using the model of S18 after finding that some potential AGN contamination was reported in previous work.

The large number of AGN interlopers, mainly revealed by attempting to fit models of pure galaxy emission, highlights the challenges in detecting faint AGN IR emission. This further supports the necessity to carefully decompose SEDs into AGN and host contribution. These sources were discarded from our sample of pure

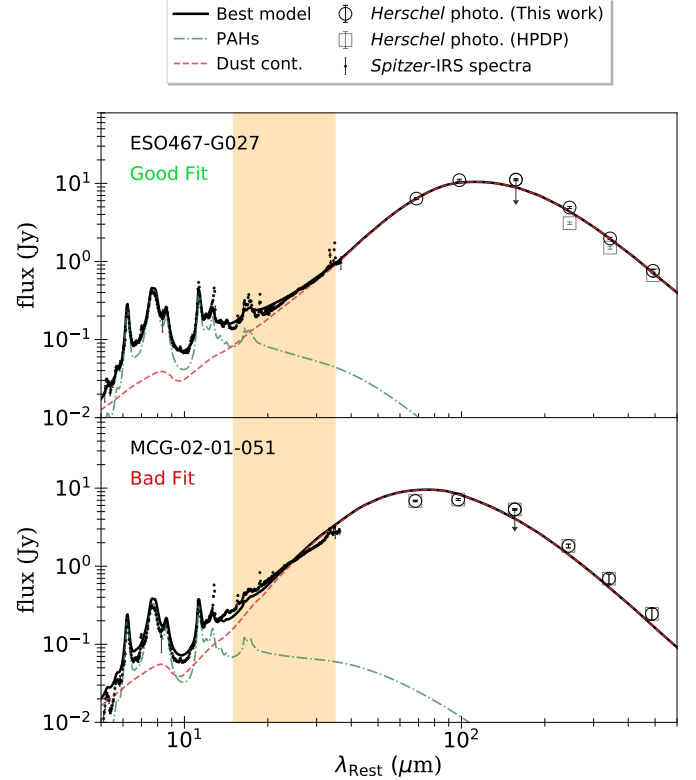


Figure 5. An example of two SED fits from our sample of star-forming galaxies. The observed *Spitzer*–IRS data are shown with small black dots, and the *Herschel* photometry, corrected for spatially extended emission, with large open circles. We also show with large open squares the *Herschel* photometry found in the HPDPs, which failed to identify the extended nature of the galaxy presented in the top panel (see § 2.2.1). The arrow on the flux at $160\ \mu\text{m}$ indicates that the flux has been included in the fit as an upper limit (see § 3.1.3). In each panel, the black line shows the best fit, decomposed into dust continuum (dashed red line) and PAH emission (dot-dashed green line). The model is affected by obscuration as explained in the text. The top panel shows an example of a good fit to the data using the model of S18, as found for 50 per cent of our sample, and the bottom panel shows an example of a poorer fit to the data, as found for the rest of the sample. The name of the two sources are indicated in the top-left hand corner of each panel. The orange area highlights the differences in the observed SEDs between the two sources, where the slope of the MIR continuum and the relative level of MIR emission differ leading to a poorer fit for MCG-02-01-051. For the latter, it was found that the MIR emission is contaminated by AGN.

star-forming galaxies, so the full sample now contains 55 sources for which we have detailed fits of their SEDs¹³. The results of the fits using the model of S18 are presented in Table C6. We stress that we demonstrate in § 3.1.5 that the galaxy templates extracted from this sample covers a wide range of observed SEDs for typical star-forming galaxies in the local Universe.

3.1.4 Templates for star-forming galaxies

We used the aforementioned 55 SED fits to build a set of templates for star-forming galaxies, based on the model of S18. To do this, we considered the PAH and the dust emission independently. For the

¹³ The full set of 55 SEDs can be found in the supplementary material, or directly at <https://tinyurl.com/ybu9jeg1>.

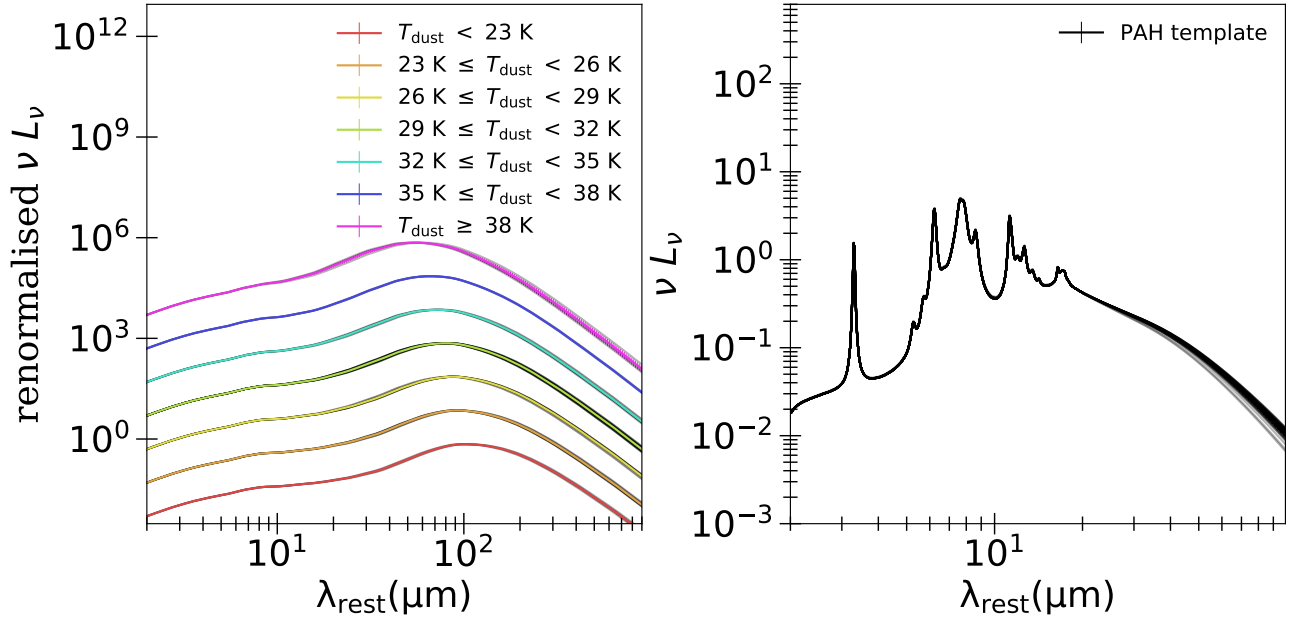


Figure 6. The eight IR SED templates for galaxies split in terms of dust continuum (left-hand side panel) and PAH emission (right-hand side panel). For the dust continuum, we split in terms of T_{dust} (see keys). For the PAHs we adopted a generic PAH template by combining all the best fits together. The thin black lines show the individual contributions of each of our galaxies.

PAH emission, we found that, once normalised to the IR luminosity (i.e. integrated from $8 \mu\text{m}$ to $1000 \mu\text{m}$; L_{IR}), a universal PAH template worked for all galaxies, consistent with some previous work (e.g. Xie et al. 2018). We constructed our typical PAH emission template by averaging over the L_{IR} normalised PAH component of our best fits. We defined 1σ uncertainties on the PAH template by measuring the standard deviation arising from combining multiple best fits (see the right-hand side panel in Fig. 6 for the PAH template).

To construct the dust continuum templates we combined together SED models in bins of T_{dust} , as T_{dust} defines the shapes of the dust continuum components in S18. We found for our best fits that $20 \text{ K} < T_{\text{dust}} < 45 \text{ K}$, with a mean at $T_{\text{dust}} \sim 33 \text{ K}$. This range of T_{dust} is consistent with that observed for general populations of galaxies, and the average T_{dust} is consistent with that measured in starburst populations (e.g. Orellana et al. 2017). We defined seven bins of T_{dust} which constitute our seven dust continuum templates, and are representative of our sample of star-forming galaxies (see the left-hand side panel in Fig. 6 for the bins of T_{dust}). As for our PAH template, we constructed our dust continuum templates by averaging over the normalised dust components of our best fits, once split in terms of T_{dust} , and calculated 1σ uncertainties. Therefore, we reduced the full set of templates from S18 to a set of eight templates, of which one represents the PAH emission and seven represent the dust continuum at various T_{dust} (see Fig. 6).

A major challenge in interpreting the emission from an AGN-hosting galaxy is being able to determine the balance between the dust heating mechanisms (i.e. AGN or stars). This often becomes heavily degenerate, in particular at wavelengths $\lambda > 70 \mu\text{m}$ where this balance is determined using SEDs that are sampled by only few photometric points. The fact that, so far, our templates are built using fully independent dust continuum and PAH emission templates can increase the degeneracies while fitting AGN SEDs. We show in Fig. 7 that there is a correlation between the IR luminosity of the dust continuum (L_{dust}) and that of the PAHs (L_{PAH}) when considering

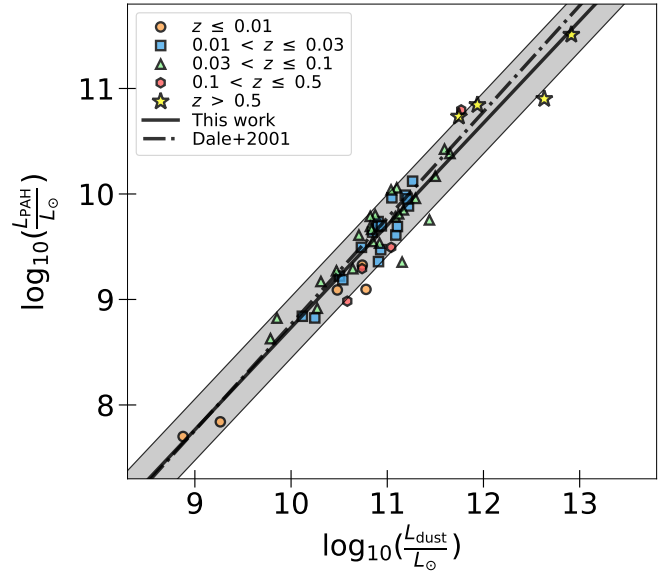


Figure 7. The relationship between the luminosity of the dust continuum and of the PAH observed while – independently – fit to our sample of star-forming galaxies. We split in terms of redshift bins (see keys) to verify that this relationship was not a consequence of the Malmquist bias. The black line shows the average best fit represented by Eq. 4, and the greyed area shows the scatter of 0.3 dex. The dot-dashed black line shows the relationship between the PAH and the dust expected in Dale et al. (2001).

both these components independently. We tried splitting in terms of redshifts to test whether this is a consequence of the Malmquist bias, and found that this relationship holds, at least at $z \lesssim 1$ where our sample lies. In addition, we note that there is no evidence of a dependence with the total luminosity (i.e. $L_{\text{IR}} \equiv L_{\text{PAH}} + L_{\text{dust}}$),

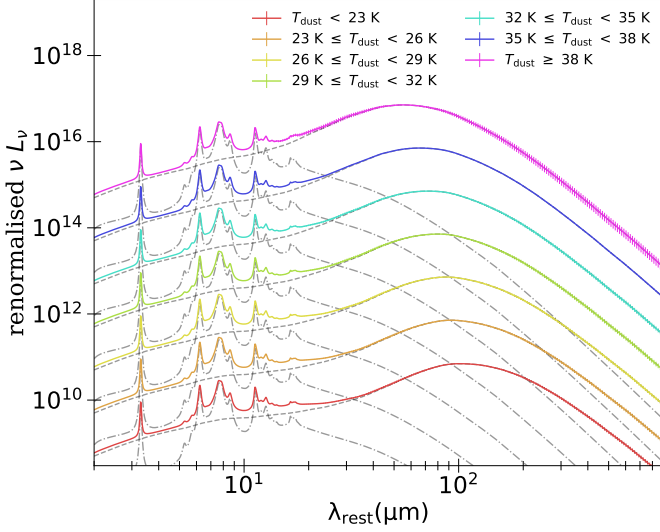


Figure 8. Our set of seven templates for galaxies where Eq. 4 was used to calculate the normalisation of the PAHs assuming $L_{\text{dust}} = 10^{11} L_{\odot}$. The different colours correspond to different dust continuum templates (see keys). The dashed and dot-dashed lines correspond to the dust continuum and PAH emission components, respectively.

and our relationship appears to be valid from $L_{\text{IR}} \sim 10^9 L_{\odot}$ to $L_{\text{IR}} \sim 10^{13} L_{\odot}$.

In light of the this, we defined the relationship between L_{PAH} and L_{dust} expressed as:

$$\log_{10}\left(\frac{L_{\text{PAH}}}{L_{\odot}}\right) \equiv 0.97 \times \log_{10}\left(\frac{L_{\text{dust}}}{L_{\odot}}\right) - 0.95. \quad (4)$$

This relationship is shown in Fig. 7, where we also show that it is fully consistent with that reported in Dale et al. (2001). In addition, to allow our PAH and dust continuum templates to combine with more extreme relative luminosities, we assumed a normally distributed scatter of $\sigma = 0.3$ dex on Eq. 4, as observed in our sample of star-forming galaxies, and shown in Fig. 7. The relationship defined in Eq. 4 and its scatter will be used while fitting the SEDs of our AGN sample (see § 3.2). We show in Fig. 8 the seven templates for star-forming galaxies after using Eq. 4, assuming $L_{\text{dust}} = 10^{11} L_{\odot}$, to connect the dust continuum to the PAH emission.

To summarise, our full set of galaxy templates contains eight individual templates spanning the wavelength range $1 \mu\text{m} < \lambda < 1000 \mu\text{m}$, of which seven represent the dust continuum at different T_{dust} , and one represents a generic PAH emission. Eq. 4 can be used to constrain the dust-to-PAH luminosity ratio, allowing for a scatter of 0.3 dex. We re-fit our sample of 55 star-forming galaxies with this set of templates and find good fits to all of these galaxies' SEDs.

3.1.5 Comparison between our non-AGN galaxy templates to previous work

In this section we compare our new galaxy SED templates to some previous widely used libraries. To do this, we first compare in Fig. 9 the νL_{ν} shapes of our templates to those from Rieke et al. (2009), Mullaney et al. (2011) and Dale et al. (2014; hereafter, R09, M11, and DH14, respectively) for which different methods were used to extract the galaxy templates. We then plot in Fig. 10 the *IRAS* F_{100}/F_{60} , F_{25}/F_{12} colour-colour space for each set of templates,

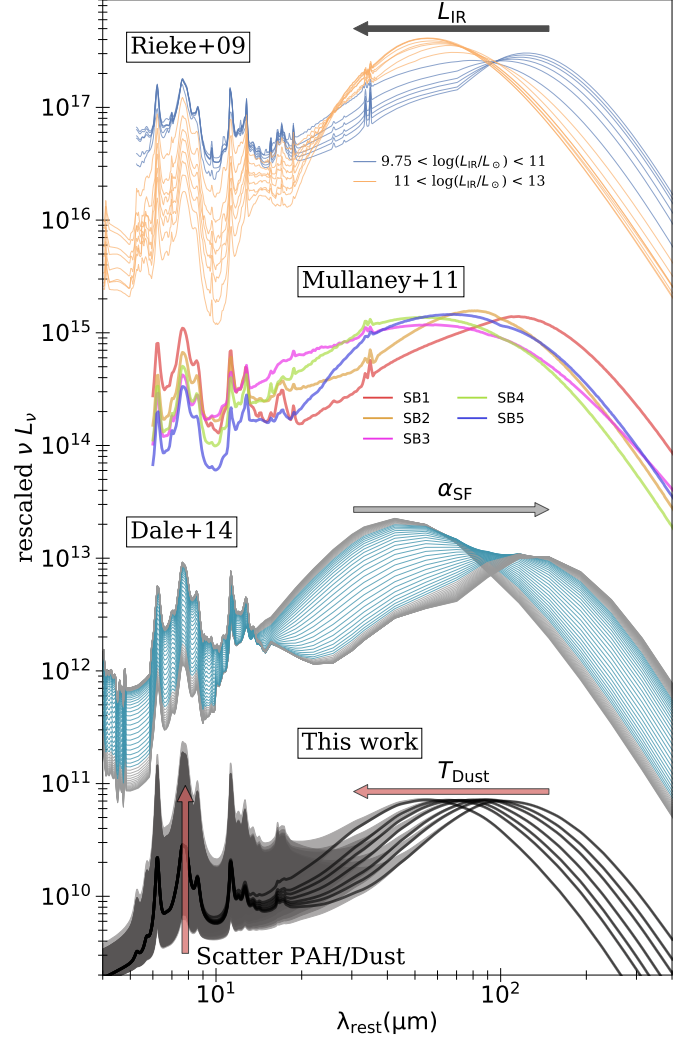


Figure 9. Comparison between our newly derived set of seven galaxy templates and several widely used libraries of templates for star-forming galaxies. *From top to bottom:* the set of templates of Rieke et al. (2009) for LIRGs and ULIRGs shown with blue and orange lines, respectively, and where L_{IR} controls the shape of the SEDs in the range $L_{\text{IR}} = 10^{9.75-13} L_{\odot}$ (see the black arrow at the top of the figure); the set of templates of Mullaney et al. (2011), colour coded by their individual names (see corresponding keys); the set of templates of Dale et al. (2014), where α_{SF} controls the shape of the SEDs between $0.0625 < \alpha_{\text{SF}} < 4$ (see the grey arrow), and where the templates representing the majority of the star-forming galaxies are highlighted in blue; and our set of templates controlled by T_{dust} (see the horizontal red arrow at the bottom of the figure), assuming $L_{\text{dust}} = 10^{11} L_{\odot}$, and where Eq. 4 was used to calculate the relative amount of PAHs, and the grey area shows the 3σ scatter (see the vertical red arrow at the bottom left-hand side of the figure).

where F_{12} , F_{25} , F_{60} , and F_{100} are the *IRAS* fluxes at $12 \mu\text{m}$, $25 \mu\text{m}$, $60 \mu\text{m}$, and $100 \mu\text{m}$, respectively, and compare against the Revised Bright Galaxy Sample (RBGS) of Sanders et al. (2003). We do this as the *IRAS* colours provide a simple way to quantify the mid-to-far-IR differences observed in Fig. 9.

In R09, 11 luminous and ultra-luminous IR galaxies (LIRGs and ULIRGs, respectively) with MIR spectra (i.e. from *Spitzer* or *ISO*), mid-to-far-IR photometry (i.e. from *Spitzer*-IRAC and *Spitzer*-MIPS out to $70 \mu\text{m}$), and radio 1.4 GHz were used to con-

struct 11 individual templates (see R09 for details). We note that R09 had to rely on a modified black-body curve to extrapolate the FIR, as *Herschel* was not available at the time. Using this set of 11 templates, and aided by previous IR SED templates (see R09 and references therein), R09 built a new set of average templates for (U)LIRGs, defined as having $L_{\text{IR}} = 10^{9.75-13} L_{\odot}$, and shown at the top of Fig. 9, where LIRGs and ULIRGs are separated by different colours as derived using different prescriptions (see R09 for more details).

To derive a set of five templates for the IR emission of galaxies, M11 used a sub-sample of 10 star-forming galaxies taken from Brandl et al. (2006) which, in turn, were extracted from the RBGS, plus four other “cold” galaxies, aiming to sample the full *IRAS* colour-colour space, and with L_{IR} ranging from $\sim 2 \times 10^{10} L_{\odot}$ to $\sim 2 \times 10^{11} L_{\odot}$. Similarly to R09, M11 used a modified black-body curve to extrapolate the FIR beyond the $100 \mu\text{m}$ *IRAS* photometry. These are shown as second from the top in Fig. 9.

The DH14 IR templates are originally from Dale et al. (2001) and Dale & Helou (2002). In DH14 they updated the MIR to the star-forming spectra of Spoon et al. (2007). The templates have been built using a series of local SEDs from dust exposed to a wide range of heating intensities, and calibrated on a sample of 69 star-forming galaxies. The parameter which controls the shape of the SED is the power-law index, α_{SF} , defining the relative contribution of each of the heating components (i.e. the hardness of the field), which is also proportional to F_{60}/F_{100} . In essence, the method used to derive this set of templates is the closest to that of used here, since models of galaxy emission have been used. The full set of templates from DH14 is shown as third from the top in Fig. 9.

At the bottom of Fig. 9, we show our set of seven average IR SED galaxy templates, for which we used Eq. 4 to determine the relative amount of PAHs assuming $L_{\text{dust}} = 10^{11} L_{\odot}$. In addition, we added the grey areas which show the effect of the scatter on Eq. 4. To show the extended effect that the scatter has on the shape of our templates, Fig. 9 shows a 3σ scatter of 0.9 dex. By design, our average templates correspond to different T_{dust} , from $T_{\text{dust}} \sim 20$ K to $T_{\text{dust}} \sim 40$ K (see § 3.1.4).

We find some differences between the various sets of templates, particularly when R09 and M11 are compared to DH14 and the templates defined in this work. Perhaps one of the most striking differences is at mid-to-far-IR wavelengths (i.e. from $20 \mu\text{m}$ to $70 \mu\text{m}$), where the templates from R09 at lower L_{IR} , and some of the M11 templates (e.g. “SB3”), have significantly flatter νL_{ν} . In fact, some peculiar galaxies (e.g. strongly starbursting galaxies or Wolf-Rayet galaxies) are known to show such flatter MIR νL_{ν} . By considering the scatter on the PAH-to-dust continuum ratio, some of our templates show a flatter νL_{ν} (see Fig. 9). One feature of our set of templates is that, at a given T_{dust} , they offer a continuous range of MIR slopes (to within the PAH-to-dust continuum scatter), in contrast with previous templates that offered a unique MIR slope once the free parameter fixed.

By comparing our set of templates to the higher luminosity ones of R09, we note that the latter are strongly affected by dust obscuration (i.e. large absorption feature are $9.7 \mu\text{m}$; see Fig. 9). This is a direct consequence of R09 using observed spectra, including highly obscured galaxies such as Arp220, which have not been corrected for obscuration. The effect of obscuration is also seen in some of the templates from M11 (e.g. “SB5”). In contrast, we have considered obscuration separately, such that, SEDs that are strongly affected by obscuration can also be reproduced by our set of templates after applying our prescriptions (see § 3.1.2). Again, this

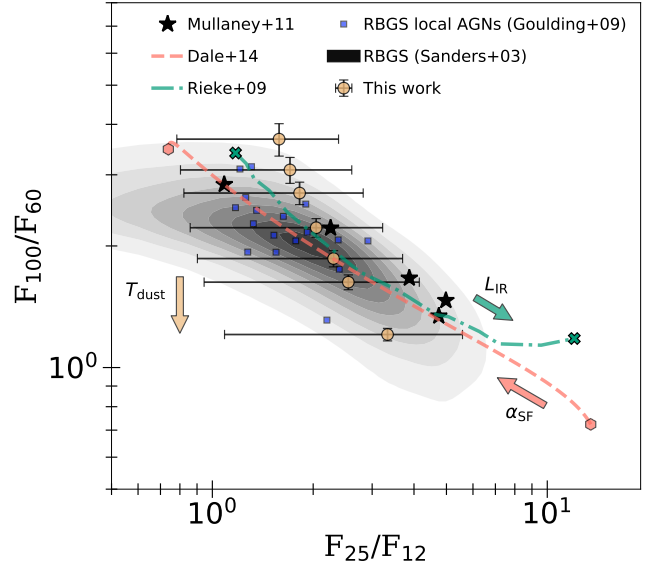


Figure 10. Plot showing the *IRAS* colour-colour parameter space, where the RBGS sample of Sanders et al. (2003) is shown as a kernel density estimation. The colour-colour parameter space covered by our set of average templates are shown with filled orange circles. The error bars illustrate departures from these average values once assuming the scatter on the PAH-to-dust continuum relationship. For illustrative purposes, we show the 3σ scatter of 0.9 dex. The black filled stars show that of Mullaney et al. (2011), the dot-dashed green line, terminated by green filled crosses, shows that of Rieke et al. (2009), for $L_{\text{IR}} = 10^{9.75-13} L_{\odot}$, and the dashed pink line, terminated by pink filled hexagons, shows that of Dale et al. (2014), with $0.0625 < \alpha_{\text{SF}} < 4$. The arrows indicate the direction of change in the *IRAS* colours when the parameter controlling the shape of each of the corresponding set of templates is changed. The small filled blue squares show the *IRAS* colours of galaxies hosting AGNs in the complete volume limited sub-sample of Goulding & Alexander (2009).

has the advantage of offering a much larger range of SED shapes compared to R09 or M11.

We find that our set of average templates is broadly consistent with that of DH14, although the latter appears to offer a wider range of FIR dust emission. However, we stress that the majority of normal star-forming galaxies have $1 < \alpha_{\text{SF}} < 2.5$ (Dale & Helou 2002), corresponding to the blue coloured DH14 templates in Fig. 9, and in better agreement with our set of average templates. Another difference is that in DH14 the mid-to-far-IR balance changes with α_{SF} , as some suppression of PAHs in harsher environments has been implemented. However, our set of templates offer a wider, more continuous range of mid-to-far-IR balance via the scatter on the PAH-to-dust continuum relationships.

In Fig. 10 we show the locations of the different sets of galaxy templates on the *IRAS* colour-colour parameter space, overlaid on the full RBGS sample of Sanders et al. (2003), the latter shown as a kernel density estimation (grey contours in Fig. 10). For each set of templates, we varied the parameter controlling the SED shapes, when necessary, and calculated the corresponding synthetic flux in each of the *IRAS* filters. For our set of templates, we assumed $L_{\text{dust}} = 10^{11} L_{\odot}$, and calculated the corresponding amount of PAHs using Eq. 4, allowing for a 3σ scatter of 0.9 dex, as shown by the error bars in Fig. 10.

We note that, by design, the M11 templates are representative of the RBGS sample since they were selected to cover most of this parameter space. However, since M11 only considered a small set of

five fixed galaxy templates, their SEDs can only accommodate for a small number of shapes. In contrast, while our average templates cover a smaller fraction of the *IRAS* colour-colour parameter space when compared to M11, the scatter in the PAH-to-dust continuum ratio allows our templates to take a large variety of shapes, and to represent most of the RBGS sample.

When compared to the galaxy templates of R09, we also find that our templates cover a larger fraction of the *IRAS* colour-colour space, due to the flexibility in terms of SED shapes. We note that the highest L_{IR} templates of R09 cover a wider range of F_{25}/F_{12} colours, which are not covered by any of our galaxy templates, even after accounting for the scatter in the relationship between the PAH and the dust continuum (see Fig. 10). However, we stress that the highest L_{IR} templates in R09 are generally affected by obscuration (see Fig. 9). This results in an artificially depleted flux at $12\ \mu\text{m}$, relative to the other *IRAS* wavelengths that are less affected by obscuration. Our templates are able to reach such extreme MIR *IRAS* flux ratios once our prescriptions for obscuration is applied (see § 3.1.2 for the obscuration prescriptions).

Our set of templates also covers a larger part of the RBGS colour-colour space than the DH14 templates. We note in Fig. 10 that for $\alpha_{\text{SF}} \sim 0.1$, the colour-colour “sequence” of the DH14 templates extend to the bottom right-hand corner, which is not covered by our templates. However, we stress that model SEDs with $\alpha_{\text{SF}} < 1$ in DH14 are atypical, since the majority of normal star-forming galaxies have $1 < \alpha_{\text{SF}} < 2.5$ (Dale & Helou 2002), which is consistent with the coverage of the *IRAS* colour-colour space probed by our galaxy templates.

Finally, we note that the *IRAS* colours of our average galaxy templates, taken as an ensemble, seem to deviate from the bulk of the RBGS sample of galaxies, while the other sets of templates closely follow the central density (see Fig 10). In fact, the RBGS sample also contains AGNs, while our sample of star-forming galaxies have been carefully built by discarding potential IR AGNs via a series of stringent selections (see § 3.1.1 and Appendix B for the selection of our sample of star-forming galaxies). In Fig. 10 we also show results from Goulding & Alexander (2009), where a volume-limited ($D < 15\ \text{Mpc}$) complete sub-sample of galaxies (regardless of whether they host an AGN or not) was selected from the RBGS, and used to investigate the ubiquity of AGNs in star-forming galaxies. To find AGNs, Goulding & Alexander (2009) used the detection of the high-ionisation emission line [NeV]. The location of these AGNs is shown with filled blue squares in Fig. 10. It appears that the selections applied to define our sample of star-forming galaxies have naturally avoided *IRAS* colours consistent with the bulk of these local AGNs found in the RBGS sample by Goulding & Alexander (2009). However, we stress that local AGN-free galaxies in Goulding & Alexander (2009) partly occupy the same locus as the local AGNs on the *IRAS* colour plot (not shown in Fig. 10 for clarity). We further emphasise that our templates are able to represent these galaxies via the inclusion of the scatter on the PAH-to-dust continuum ratio.

3.2 IR templates for AGN emission

In § 3.1 we defined a set of templates for (non-AGN) star-forming galaxy IR SEDs based on the results of L19 and S18. In this section, we explain how we used this set of templates to fit the IR SEDs of our sample of local AGNs defined in § 2.3 (see also Table C1). The AGN emission was accounted-for with a flexible IR model (see § 3.2.1), which we combined with our galaxy templates to construct an SED representing the whole system (i.e. galaxy + AGN; see § 3.2.2). We

then used the results from the fits to build three generic templates which are representative of AGN emission at IR wavelengths (see § 3.2.3).

3.2.1 A flexible model for AGN IR emission

To account for the possibility of AGN emission in our observed IR SEDs, we defined a model which is flexible enough to fit a diverse range of SED shapes. In fact, previous studies have found a wide variety of SED shapes to represent the IR emission of AGNs, depending on whether their focus was on bright QSOs (e.g. Richards et al. 2006; Netzer et al. 2007; Schweitzer et al. 2008; Lani et al. 2017; Symeonidis et al. 2016; Lyu et al. 2017; Lyu & Rieke 2018), or more typical Seyfert galaxies (e.g. Mullaney et al. 2011; Mor & Netzer 2012).

3.2.1.1 AGN IR continuum The AGN IR continuum can have a complex shape as a result of the various dusty structures on different scales that might be illuminated by the AGN. In particular, dust close to the centre (e.g. the inner part of the dusty torus) will emit at shorter IR wavelengths, while dust located farther away from the centre (e.g. in the narrow line region, or even at galactic scales) will emit at longer IR wavelengths (e.g. Schweitzer et al. 2008; Hönig et al. 2013; Lyu & Rieke 2018). In fact, the connection between these emitting regions is far from clear. Therefore, we defined a model to represent the AGN continuum which can easily account for such complexity. We adopted three smoothly-connected broken power-laws. Each of these is expressed as,

$$B_{\nu} = \lambda^{\alpha_i} \times \left(1 + \left(\frac{\lambda}{\lambda_{\text{break}}} \right)^{|\alpha_j - \alpha_i| \times s} \right)^{\frac{\text{sgn}(\alpha_j - \alpha_i)}{s}}, \quad (5)$$

where B_{ν} is the flux density, α_i and α_j are the slopes before and after the break, respectively, λ_{break} is the position of the break, s is a smoothing factor, and $\text{sgn}(\alpha_j - \alpha_i)$ is the sign of the difference between the slopes after and before the break, respectively.

The positions of the breaks were fixed to $11\ \mu\text{m}$ and $18\ \mu\text{m}$ for the first and the second broken power-laws, respectively, and free to change at $\lambda > 30\ \mu\text{m}$ for the third broken power-law. To ensure continuity, the slopes were defined such that, if we call the slopes of the first broken power-law $\alpha_i = \alpha_1$ and $\alpha_j = \alpha_2$ in Eq. 5, then $\alpha_i = \alpha_2$ and $\alpha_j = \alpha_3$, and $\alpha_i = \alpha_3$ and $\alpha_j = \alpha_4$ in Eq. 5, for the second and the third broken power-laws, respectively.

By defining the positions of the breaks at $11\ \mu\text{m}$, $18\ \mu\text{m}$, and $\lambda > 30\ \mu\text{m}$, for the first, the second and the third broken power-laws, respectively, we allow our model for the AGN continuum to adopt different relative contributions of the hot, warm and cold dust. The choice of fixing the positions of the breaks to wavelengths corresponding to the peak of the silicate emission (see below for the model of the silicate emission) was purely empirical, yet allowed our model for the continuum to have extra flexibility at these particular wavelengths, and avoid over-estimating the strength of the silicate emission. More importantly, the break at $18\ \mu\text{m}$ for the second broken power-law was to account for the “IR bump” observed in some AGNs (e.g. Deo et al. 2009), and now believed to be related to some extended AGN-heated dust emission (e.g. Hönig et al. 2013; Lyu & Rieke 2018). The latter remains poorly explored, and should not be confused with the silicate emission peak at $18\ \mu\text{m}$ (e.g. Deo et al. 2009; Prieto et al. 2010). We note that shifting the positions of the fixed breaks by a few microns do not have any impacts on our results. Finally, λ_{break} for the third broken power-law was free to

change at $\lambda > 30 \mu\text{m}$ as there is no consensus on the universality of this value (e.g. Richards et al. 2006; Mullaney et al. 2011; Lani et al. 2017; Symeonidis et al. 2016).

The slopes α_1 , α_2 and α_3 were free to change, and we fixed the last slope to $\alpha_4 = -3.5$. The latter was to mimic the Rayleigh-Jeans tail of a modified black body with $\beta = 1.5$. We do this to reduce degeneracies, as the flexibility of our AGN continuum model is such that over-fitting could arise at longer wavelengths if no PAH emission were available to better constrain the dust continuum. The value of $\alpha_4 = -3.5$ was adopted as this is the value that is often empirically assumed in studies characterising the IR emission of AGNs (e.g. Mullaney et al. 2011; Symeonidis et al. 2016). This is also consistent with the slope at longer wavelengths found by radiative transfer applied to dusty torus in AGNs (e.g. Siebenmorgen et al. 2005).

The full model for AGN IR continuum was defined by connecting these three broken power-laws, at $14.5 \mu\text{m}$ for the first and the second broken power-law, and at $24 \mu\text{m}$ for the second and the third broken power-laws. These were chosen to fall between the breaks (i.e. in the linear regime of each of the broken power-laws) to ensure a smooth connection. The full model for AGN continuum was then normalised at $14.5 \mu\text{m}$. The overall normalisation, the slopes α_1 , α_2 , α_3 , and the position of the break for the last broken power-law are the free parameters. We show in Fig. 11 with dot-dashed blue lines a few examples of the various shapes that our model for the AGN IR continuum can take.

3.2.1.2 AGN silicate emission In the case of some AGNs, two main MIR silicate emission features have been observed, one around $\sim 10\text{--}11 \mu\text{m}$, and another around $\sim 17\text{--}18 \mu\text{m}$, and there is no consensus to the exact wavelength at which each of these silicate emission features peak (e.g. Hao et al. 2005; Sturm et al. 2005; Hao et al. 2007; Schweitzer et al. 2008; Hatziminaoglou et al. 2015; Martínez-Paredes et al. 2020). Hereafter, we refer to the silicate features at shorter and longer wavelengths as the $11 \mu\text{m}$ and $18 \mu\text{m}$ features, respectively. Although these silicate emission features have been extensively observed, their exact shapes are largely unknown, and vary depending on the models (see e.g. Martínez-Paredes et al. 2020, and references therein). In addition, the determination of the exact shape of the $18 \mu\text{m}$ silicate emission feature is made more difficult by the presence of some continuum features observed at similar wavelengths (e.g. Deo et al. 2009; Hatziminaoglou et al. 2015).

To account for the silicate emission features, we adopted a profile that was inspired by previous work (Schweitzer et al. 2008; Hatziminaoglou et al. 2015). Because the silicate emission at $11 \mu\text{m}$ is easily noticeable, we defined the shape of the silicate emission based on that at $11 \mu\text{m}$, and assumed that the $18 \mu\text{m}$ feature had the same shape. Based on previous work, and using the SEDs in our sample for which the *Spitzer*-IRS spectrum was clearly dominated by silicate emission (e.g. Ark120, ESO548-81, Mrk50, Fairall9, and some PG QSOs), we found that the silicate emission at $11 \mu\text{m}$ was best reproduced when we used a broken power-law (i.e. Eq. 5) peaking at $11 \mu\text{m}$, and with $\alpha_i = 18$, $\alpha_j = -5$, and $s = 0.6$. The silicate emission at $18 \mu\text{m}$ was reproduced by using a broken power-law with the same parameters as that at $11 \mu\text{m}$, but shifting the peak to $18 \mu\text{m}$.

In addition, in the fits, we will also allow for the peaks of the silicate emission to shift from their native values of $11 \mu\text{m}$ and $18 \mu\text{m}$, by a maximum of $\pm 1 \mu\text{m}$, which is consistent with observations, though currently unexplained (e.g. Hatziminaoglou et al. 2015). The same shift was applied to both the $11 \mu\text{m}$ and the

$18 \mu\text{m}$ silicate features, as there is no reason to why they should be different. We show in Fig. 11 with dot-dashed green lines a few examples of shapes for the silicate emission, where the only free parameters are the normalisations of the silicate emission features, and the shift of the peaks.

3.2.1.3 Full AGN model Our full model for AGN emission was therefore defined by the sum of our AGN continuum model and our silicate emission features. So far, this model contains in total eight free parameters, which are: the overall normalisation for the continuum (defined at $14.5 \mu\text{m}$), the three slopes of the continuum (α_1 , α_2 , and α_3), the position of the break at longer wavelengths (λ_{break}), the two normalisations for the silicate emission, and the shift of the peaks of the silicate emission. This AGN model is referred to as our “full AGN model”, to distinguish it from our AGN templates defined in § 3.2.3.

3.2.2 Fits to the AGN SEDs

Our approach to extracting the intrinsic AGN emission was to fit our AGN SEDs with each of our galaxy templates defined in § 3.1 combined with our full AGN model (see § 3.2.1). We stress that we used a fitting approach (as opposed to simply subtracting the host contribution to extract the AGN emission), as the IR can be a complicated mixture of each of these contributions, and these can “play off” against each other. So far, our whole model (i.e. galaxy + AGN) contains ten free parameters. In particular, two parameters correspond to the galaxy emission (i.e. one normalisation for the galaxy templates and one for the normalisation of the PAH template, see § 3.1), and eight correspond to our full AGN model (see § 3.2.1).

To find the best fit parameters we employed an MLE approach of a similar design to that presented in § 3.1. As for our galaxy sample, we replaced fluxes at $160 \mu\text{m}$ with upper limits in the fits for sources at $z < 0.3$ (see § 3.1.3). Prior to the fits, we measured the level of obscuration present in the AGN SEDs by using the observed $9.7 \mu\text{m}$ silicate absorption feature, as described in § 3.1.2. However, the assumption of a uniformly mixed absorbing and emitting material, as used for the galaxy (see § 3.1.2), does not hold for the AGN obscuration. Instead, for the AGN system, we used a more appropriate assumption which is a source behind a screen of dust, and for which the solution to the transfer equation is given by (e.g. Calzetti 2001; Krügel 2009),

$$\Theta(\tau_\lambda) = e^{-\tau_\lambda}, \quad (6)$$

instead of eq. 2. Therefore, while we assume that the system AGN and galaxy are affected by the same amount of obscuration at $9.7 \mu\text{m}$ (defined by the ratio between the observed to the intrinsic fluxes at $9.7 \mu\text{m}$), the optical depth of the two systems, $\tau_{9.7}$, are different. In addition, we found significantly better fits to the AGN SEDs, when we used the extinction curve of PAHfit (Smith et al. 2007), instead of that defined for the galaxy in § 3.1.2.

To summarise, the level of obscuration in the whole system (AGN + galaxy) was calculated using the ratio of the observed to the intrinsic fluxes at $9.7 \mu\text{m}$. Subsequently, the optical depth at $9.7 \mu\text{m}$, $\tau_{9.7}$, was calculated by using Eq. 1, where $\Theta(\tau_\lambda)$ was substituted by the expression in Eq. 2 (i.e. assuming uniformly mixed absorbing and emitting materials) and that in Eq. 6 (i.e. assuming a screen of dust), for the galaxy and the AGN, respectively. Then, the pseudo-extinction curve presented in § 3.1.2 was used on the galaxy dust continuum templates, within the context of a uniformly mixed obscuring and emitting material, and using the corresponding

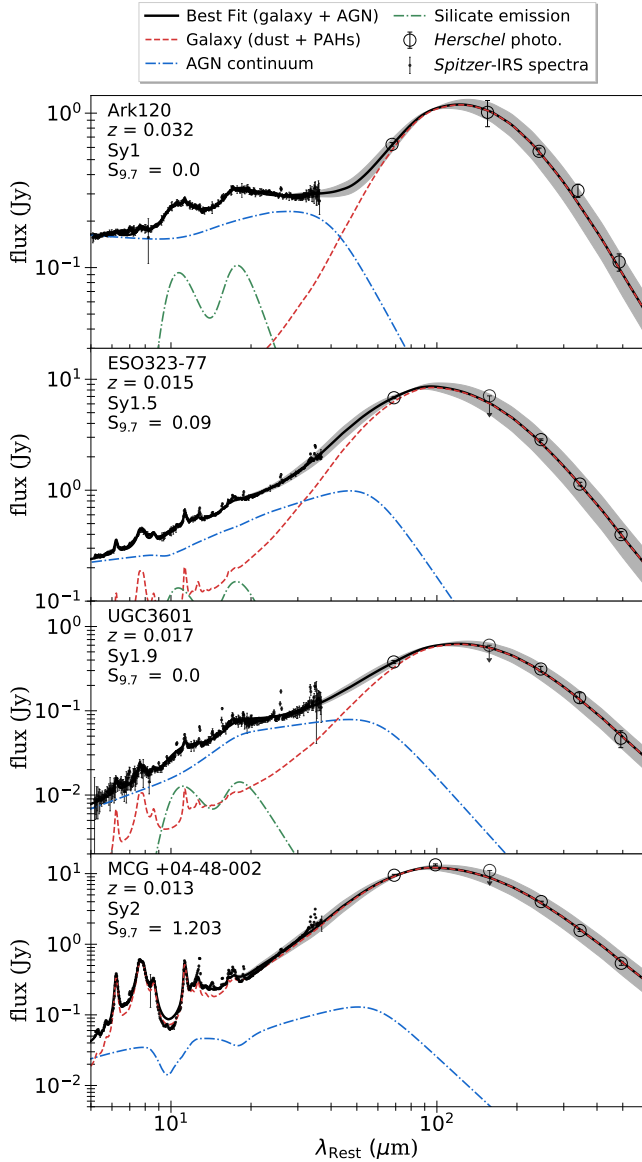


Figure 11. Examples of four best fits of AGN IR SEDs using a combination of our galaxy templates (see § 3.1) and our full AGN model (see § 3.2.1). The observed *Spitzer*–*IRS* data are shown with small black dots and the *Herschel* photometry with large open circles. The arrow on the flux at 160 μm indicates that it has been set as an upper limit in the fits (not due to non-detection, but instead due to the possible boosting by [CII]; see § 3.1.3). In each panel, the black line shows the attenuated full weighted model (i.e. galaxy + AGN; see § 3.2.2), the red dashed line shows the attenuated galaxy contribution, and the dot-dashed blue and green lines show the attenuated AGN continuum and silicate emission, respectively. The grey area shows the weighted uncertainties carried forward from the galaxy templates. The names of the sources, the redshifts, the optical types, and the absorption at 9.7 μm (see Eq. 7 for $S_{9.7}$) are indicated in the top-left corner of each panel.

value of $\tau_{9.7}$ (we recall that the PAHs are assumed to be free of obscuration; see § 3.1.3). Similarly, the extinction curve of PAHfit was used on the AGN model (continuum and silicate emission), within the context of a screen of dust, and using the corresponding $\tau_{9.7}$. This allows our model to fit SEDs displaying a large amount of obscuration, as is the case for “MCG+04-48-002”, which is shown in the bottom panel of Fig. 11. In addition, we note that our model

was able to fit the SED of the peculiar Mrk 231, which is classified as an optically unobscured source, yet shows a large silicate absorption feature at 9.7 μm . The latter was not in our original sample of AGNs.

Due to the large number of free parameters in the AGN model, we must define some boundaries (i.e. priors) to avoid degeneracies while fitting the AGN SEDs. In particular, we found that if the position of the break (λ_{break}) was unconstrained at longer wavelengths (i.e. at $\lambda > 30 \mu\text{m}$), then a number of fits became fully degenerate. This was particularly true for SEDs whose MIR emission is dominated by silicate emission, and which lacked PAH features. By using fits in which we had no significant degeneracies, we found, on average, that $\lambda_{\text{break}} = 40 \mu\text{m}$. In light of this, we constrained λ_{break} by using a normally-distributed prior centred at $\lambda_{\text{break}}^{\text{prior}} = 40 \mu\text{m}$ and with a standard deviation of $\sigma_{\text{break}}^{\text{prior}} = 10 \mu\text{m}$. We stress that this prior is weak enough to accept fits with $\lambda_{\text{break}} > 40 \mu\text{m}$ when required by the data. In doing so, we find that the value of the break can extend out to $\lambda_{\text{break}} \sim 100 \mu\text{m}$ in the case of some of our AGNs.

We also placed boundaries and prior information on the slopes α_1 , α_2 , and α_3 to remove non-physical regions of parameter space and avoid over-fitting. We defined $-3.5 < \alpha_1 < 3.5$, $-3.5 < \alpha_2 < 3.5$, and $-3.5 < \alpha_3 < 1$. These are in agreement with the range of values observed in previously measured AGN SEDs (e.g. Mullaney et al. 2011; Lyu et al. 2017; Xu et al. 2020), or in models of dusty torus emission (e.g. Siebenmorgen et al. 2005; Hönig & Kishimoto 2010).

We assumed that the strengths of the silicate features at 11 μm and 18 μm are identical by using a single normalisation for both. This choice was made to avoid over-fitting that at 18 μm , since found to be blended with some continuum features. In fact, relatively little attention has been paid to the silicate emission at 18 μm (e.g. Hatziminaoglou et al. 2015). However, some recent studies that carefully decomposed the *Spitzer*–*IRS* spectra of Type-I QSOs showed that the strengths of the two features are consistent to within the uncertainties (Martínez-Paredes et al. 2020), supporting our assumption. In addition, this reduces the number of free parameters of our full AGN model (see § 3.2.1 for the AGN model) from ten to nine.

The relationship between the relative level of PAHs to dust continuum (see § 3.1) was incorporated by using Eq. 4. To do this, we set a normally distributed prior, centred on the value returned by Eq. 4 for a given L_{dust} , and with a standard deviation of 0.3 dex. As such, values of L_{dust} and L_{PAH} which deviate from Eq. 4 are less likely. The inclusion of such relationship between the PAH and the dust continuum reduced degeneracies, and helped the determination of the level of FIR emission of dust heated by regions of star formation when PAH features were observed in the *Spitzer*–*IRS* spectra.

We fit each of our AGN SEDs separately, with each of our galaxy templates plus our full AGN model. To test whether the AGN component was necessary, we also independently fit our AGN SEDs with each of our galaxy templates alone (i.e. without including the AGN model). We therefore performed a total of 14 possible fits for each source, seven of which included an AGN component (i.e. one for each galaxy component). To select the best fit amongst these various attempts, we used the Akaike Information Criterion (e.g. Akaike 1973, 1994, AIC). The AIC is a function of the log-likelihood returned by the fit, and enables the comparison of models that have a different number of free parameters. The best model has the minimum AIC, and each model can be weighted accordingly using the Akaike weight (e.g. Akaike 1973, 1994). Therefore, in-

stead of using the best fits (i.e. minimum AIC), and if not otherwise stated, all our results are based on a weighted sum of the 14 models.

We show in Fig. 11 four examples of best weighted fits, split in terms of galaxy and AGN contributions. We note that our full AGN model is able to accommodate a large variety of AGN SEDs, whether the AGN contribution is minimal or dominates, and allows for different levels of AGN continuum to silicate emission¹⁴.

Out of our full sample of 112 AGNs, we found two sources for which the *Herschel*-SPIRE fluxes were contaminated by nearby companions (i.e. MCG-1-24-12 and NGC2992), potentially affecting their SED fits. We discarded these two sources from further analysis to avoid biasing the construction of our IR AGN templates (see § 3.2.3 for the AGN templates). In addition, we found ten SEDs that were poorly fit by our model¹⁵. Amongst those, six showed potential inconsistencies in the *Herschel* photometry, perhaps arising from the images used to calculate their fluxes (these are flagged with a dag in Table C2). Furthermore, we found that the ten sources that were poorly fit are the most spatially extended, and we suspect that their *Spitzer*-IRS observations only captured the nuclear emission dominated by the AGN. In such cases, the simple re-scaling of the *Spitzer*-IRS spectra to match the photometry is not sufficient, as substantial PAH emission from the galaxy could have been missed. Therefore, we also discarded these ten sources from further analysis, and only considered the remaining 100 AGNs for which we have detailed SED fits.

3.2.3 Constructing IR templates for AGN emission

In § 3.2.1 we defined a flexible model for the IR emission of AGNs which, once combined with our galaxy templates, was able to fit the IR SEDs (consisting of a combination of *Spitzer*-IRS spectra and *Herschel* photometry) of our AGN sample. We now explain how we used the results of these fits to build our three AGN templates. The individual AGN contributions were defined by the best fitting parameters, which were calculated using a linear sum of all of the possible model attempts, weighted by their respective Akaike weights, as described in § 3.2.2, and considering the AGN continuum and the silicate emission separately, as there no strong evidence for a relationship between the two (e.g. Deo et al. 2009; Hatziminaoglou et al. 2015).

The extinction-corrected models for the continuum of our sample of 100 AGNs (free of silicate emission) are shown as thin lines in Fig. 12. In each case we have normalised the SEDs to L_{IR} (i.e. integrated from $8 \mu\text{m}$ to $1000 \mu\text{m}$). This shows the large diversity found in the continuum emission of AGNs at IR wavelengths. In particular, we find that the position of the break, λ_{break} , ranges from $\sim 11 \mu\text{m}$ ¹⁶ to $\sim 100 \mu\text{m}$ with a mean position of $\sim 54 \mu\text{m}$. We recall, however, that we placed a constraint on λ_{break} for which values at $\lambda > 40 \mu\text{m}$ were less likely (see § 3.2.2). We further find that the MIR slope (α_{MIR}), defined by the average value of α_1 and α_2 in our full AGN model (see § 3.2.1 for the AGN model), can take a large range of values, effectively producing a diverse range of SEDs, from flatter ones with $\alpha_{\text{MIR}} \sim 0$ to steeply rising ones with $\alpha_{\text{MIR}} \sim 3$.

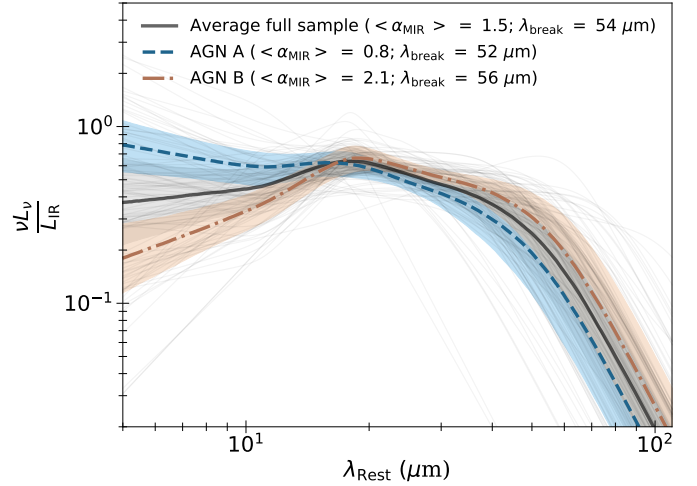


Figure 12. Our two AGN continuum templates, free of silicate emission, were built by combining the best fitting AGN contributions of our SEDs. The divide between the two was based on the MIR slope, α_{MIR} (see § 3.2.3). The dashed blue and the dot-dashed brown lines are our “AGN A” and “AGN B” templates, respectively. We also show with shaded blue and brown areas an estimation of the 1σ uncertainties for our “AGN A” and “AGN B” templates, respectively. The black line shows the average AGN continuum SED of the full sample of 100 AGNs, and the grey area shows an estimation of the 1σ uncertainties. The thin black lines show each individual AGN continuum used to construct our templates. The main parameters of each of the templates are indicated in the keys.

The mean α_{MIR} is found to be ~ 1.5 , and is slightly higher than the average value of 1.2 reported in Mullaney et al. (2011; averaging their Γ_1 and Γ_2).

To build a set of templates for the AGN continuum, we separated our best fits into two bins using the slope α_{MIR} (see § 4.2 for the motivation). By splitting our sample at the average value of $\alpha_{\text{MIR}} = 1.5$, we defined two template SEDs for the AGN continuum emission: “AGN A” and “AGN B”. We note that the mean α_{MIR} for the “AGN A” and the “AGN B” templates are 0.8 and 2.1, respectively, while the mean λ_{break} for the “AGN A” and “AGN B” templates are $52 \mu\text{m}$ and $56 \mu\text{m}$, respectively. In Fig. 12 we plot the “AGN A” template as a dashed blue line, and the “AGN B” template as a dot-dashed brown line. The uncertainties on the AGN templates were estimated using the first and the third quartiles of 5000 realisations, randomly drawing the best parameters defining our AGN templates to within 1σ uncertainties. The average AGN SED for the whole sample is shown with a black line in Fig. 12.

By design, the silicate emission at $11 \mu\text{m}$ and $18 \mu\text{m}$ are similar (see § 3.2.1 and § 3.2.2). We find that the average shift is $\lambda_{\text{shift}}^{\text{Si}} \sim 0.1 \mu\text{m}$, such that, the silicate features peak at $\sim 11 \mu\text{m}$ and ~ 18 , consistent with previous work (e.g. Hatziminaoglou et al. 2015). To build a template for the silicate emission, we simply averaged over the full sample, after normalising to L_{IR} , to extract the typical silicate emission observed in AGNs. The uncertainties on the average template for the silicate emission were built as for those on our AGN continuum templates.

We have, therefore, a total of three AGN templates, two of which correspond to AGN continuum (“AGN A” and “AGN B”) and one of which corresponds to silicate emission. We note that to build these templates we adopted a simple flexible model for the AGN continuum and silicate emissions. In fact, detailed investigations of the AGN contribution to the near-to-mid-IR reveals a rather complex dust geometry and composition (e.g. hot graphite dust, dusty narrow

¹⁴ The individual fits for each of our AGN SEDs are available at <https://tinyurl.com/1f7lrd7t>

¹⁵ These are: ESO511-30, Mrk1018, NGC3147, NGC788, NGC2655, NGC4258, NGC4939, NGC4941, NGC7682, and Z121-75

¹⁶ We note that the position of the break was limited to $\lambda_{\text{break}} > 30 \mu\text{m}$. However, some of our fits showed a steeply decreasing α_2 and α_3 , which is equivalent to a break at $\lambda = 11 \mu\text{m}$.

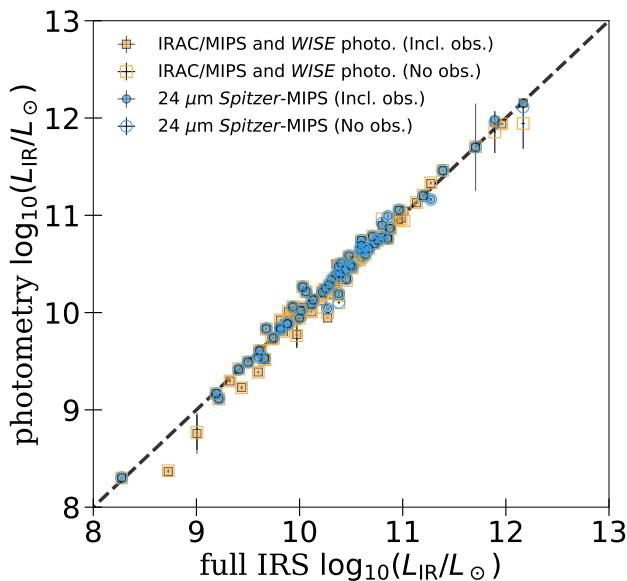


Figure 13. Comparison between the host galaxy (i.e. after removing any AGN contamination) IR luminosities of our sample when our fit includes *Spitzer*–IRS spectra, against when we fit to photometric data alone. The blue circles show results obtained when we replaced *Spitzer*–IRS spectra with 24 μm *Spitzer*–MIPS photometry alone, while the orange squares show those obtained when we replaced *Spitzer*–IRS spectra with 5 μm and 8 μm *Spitzer*–IRAC, 12 μm and 22 μm *WISE*, and 24 μm *Spitzer*–MIPS photometry. For both, filled and open symbols correspond to when obscuration was accounted for, to when ignored, respectively (the open and filled symbols generally overlap). Irrespective of what photometry we replaced the *Spitzer*–IRS data with, and whether obscuration was accounted for, we find very good agreements between luminosities derived from when we included the *Spitzer*–IRS spectra versus when we did not. The dashed black line shows the 1:1 relationship.

line regions, hollow cone; e.g. [Schweitzer et al. 2008](#); [Mor & Netzer 2012](#); [Hönig 2019](#)). However, we stress that for this work, we are only interested in accurately removing the AGN contribution to the IR, rather than performing a detailed analysis of the various dust components observed in AGNs.

3.2.4 Comparing results from our AGN templates to our full AGN model

We now have a set of IR templates for AGNs, built using the best SED fits that includes *Spitzer*–IRS spectra and *Herschel* photometry. This set of templates can be used to fit AGN SEDs for which less rich datasets are available (e.g. photometry alone instead of IR spectra). In this section, we test that our set of templates (i.e. galaxy and AGNs) could, indeed, recover the host IR properties of our AGN sample when the data are reduced to only include photometry. To do this, we replaced the *Spitzer*–IRS spectra of our AGN sample with photometric data at MIR wavelengths. We used the *WISE* photometric fluxes at 12 μm and 22 μm , the *Spitzer*–IRAC photometric fluxes at 5.8 μm and 8 μm , and the *Spitzer*–MIPS photometric flux at 24 μm , all collected from the IRSA database. We then re-fit the AGN sample (after replacing the *Spitzer*–IRS spectra with photometry) with a combination of each of our galaxy and AGN templates. Our fitting routine was of a similar design to that used when fitting our full AGN model (see § 3.2.2), but replacing the six free parameters of the latter with a single normalisation for the

AGN continuum and a single normalisation for the silicate emission. As we have measured the level of obscuration using the *Spitzer*–IRS spectra for our sample of AGNs, we subjected the templates to obscuration using the prescriptions of § 3.1.2 (see also § 3.2.2).

In Fig. 13 we show that the host IR luminosities (L_{IR}) inferred from photometric fits only, using our set of AGN and galaxy templates, are in very good agreements with those inferred from detailed fits (see § 3.2.1 for the full AGN model) in which *Spitzer*–IRS spectra were included (filled orange squares in Fig. 13). On average, the ratio between the two L_{IR} is one, and the standard deviation is 0.4. We note that the average standard deviation is dominated by a handful of sources which significantly deviates from the one-to-one relationship between the two inferred L_{IR} . These latter cases lack *Spitzer*–MIPS photometry, potentially reducing the accuracy of the fits. The standard deviation between the two inferred L_{IR} is reduced to 0.2 when only including sources that have measured *Spitzer*–MIPS photometry in addition to *Spitzer*–IRAC and *WISE* photometry.

To test our templates further, we also considered fits where the minimal amount of data is available by replacing the full *Spitzer*–IRS spectra by a single observed *Spitzer*–MIPS 24 μm flux. We find that, even in these minimal conditions, the AGN-free L_{IR} inferred from the photometric fits are in very good agreements with those measured in the detailed fits that included the *Spitzer*–IRS spectra, and the L_{IR} are also recovered to within 20 per cent (see Fig. 13).

To test the importance of obscuration, we re-performed the two aforementioned photometric fits, this time ignoring obscuration. As shown in Fig. 13, this has no significant effect on the recovered L_{IR} for the vast majority of sources. In fact, the obscuration has a significant effect on the inferred L_{IR} only for the rare sources in our sample with large levels of obscuration, such as NGC3079. However, we stress that the difference is at most a factor of two. The lack of importance of the obscuration is likely related to the minimal effect of obscuration at most IR wavelengths, when compared to, for instance, optical wavelengths. Therefore, although accounting for obscuration is preferred when aiming to model the detailed features observed in the *Spitzer*–IRS spectra, it has no significant effects on the integrated properties of the hosts.

Finally, when performing fits with a *single photometric measurement* in the MIR, we have removed the silicate emission template as there were not enough data to constrain the galaxy (continuum + PAHs), the AGN continuum, and the silicate emission features. Nevertheless, this has no impact on the inferred L_{IR} , as shown in Fig. 13.

3.3 IRAGNSEP: a fitting code to decompose AGN IR SEDs

For the purpose of this work, we have developed IRAGNSEP which performs IR SED fits to separate AGN and galaxy contributions. Using IRAGNSEP, one can extract the host galaxy properties, such as SFRs, free of AGN contamination. The advantage of IRAGNSEP is that, in addition to fitting observed photometric fluxes, it also allows spectra to be incorporated in the fits which, if available, can greatly improve the robustness of the AGN–galaxy separation.

For the galaxy component IRAGNSEP uses the library of seven templates built from the sample of local star-forming galaxies described and presented in § 3.1 (see also Fig. 8). In terms of the AGN contribution, if the input dataset is a mixture of spectral and photometric data, then IRAGNSEP uses our full AGN model presented in § 3.2.1. If, instead, the dataset contains photometric data alone, the AGN contribution is accounted-for using our library of three AGN templates presented in § 3.2.3. The models can be corrected

for obscuration, either calculated by IRAGNSEP when spectral information in the MIR is provided, or set by the user (see § 3.1.2 for the method). The user can also easily modify the parameter space explored by IRAGNSEP by controlling the priors on each of the parameters defining the galaxy and the AGN emissions.

The advanced fitting techniques used by IRAGNSEP (i.e. MLE optimised with MCMC, see § 3.1.3 and § 3.2.2) combined with the powerful model comparison tests (i.e. AIC, see § 3.2.2) allow IRAGNSEP to provide a statistically robust interpretation of IR SEDs in terms of AGN–galaxy contributions. IRAGNSEP also uses NUMBA (Lam et al. 2015) wrappers which translate Python functions to the LLVM compiler library, offering speeds that can approach those of C or FORTRAN, therefore allowing IRAGNSEP to be applied to a large number of sources. We stress, however, that IRAGNSEP has been designed on a sample of local ($z < 0.3$), low-to-high X-ray luminosity AGNs (i.e. $L_{\text{bol}} \sim 10^{42-46} \text{ erg s}^{-1}$; see § 2), with bright FIR emission. As such, care must be taken when applying these templates to higher z and/or fainter FIR sources. Future work aims at testing IRAGNSEP on such sources.

IRAGNSEP is freely available at <https://pypi.org/project/iragnsep/>. We used the version 7.2.0 for this work. The templates associated with this work are available in the supplementary material, or directly at <https://tinyurl.com/yawp96qc>.

4 RESULTS AND DISCUSSION

In this work, we have carried out a post-*Herschel* investigation of the intrinsic AGN emission at IR wavelengths using a sample of local ($z < 0.3$), low-to-high X-ray luminosity (i.e. $L_{\text{bol}} \sim 10^{42-46} \text{ erg s}^{-1}$) AGNs. First, from a sample of local star-forming galaxy SEDs, we built a set of seven templates representing galaxy emission (see § 3.1). Then, the IR contribution to the SEDs of AGN was extracted by successfully fitting the total SEDs with a combination of one of our galaxy templates and our full AGN model (see § 3.2.2). Finally, using these best fits, we constructed a set of three IR templates to represent the AGN emission. Two of these three correspond to AGN IR continuum (coined “AGN A” and “AGN B”), while the third corresponds to silicate emission (see § 3.2.3).

In this section, we compare our templates to previous work, and discuss the implications of our new library of templates. In § 4.1, we compare our AGN continuum templates to previous work. In § 4.2, we discuss the intrinsic differences of our two AGN continuum templates, which appear to be related to the level of nuclear obscuration along the line of sight. Finally, in § 4.3 we investigate the relationship between AGN luminosity and FIR emission.

4.1 Comparison with previous IR templates for AGNs

In Fig. 14 we compare our two AGN continuum templates against those obtained in previous studies. We recall that our AGN templates have been corrected for obscuration, following prescriptions presented in § 3.1.2 (see also § 3.2.2; although see § 4.2 for a discussion on the obscuration), and that the silicate emission has been considered separately, so Fig. 14 shows the “intrinsic” AGN continua found in this work, free of silicate emission. To ease comparison, we chose to renormalise each of the templates to L_{IR} (i.e. integrated from $8 \mu\text{m}$ to $1000 \mu\text{m}$), after extrapolating at shorter and/or longer wavelengths when necessary. We stress, however, that the extrapolations were only used to calculate L_{IR} , and to renormalise the templates, and Fig. 14 shows the templates within the range of wavelengths defined by the corresponding authors. This

choice of normalisation allows us to directly compare the relative mid-to-far-IR output power amongst AGN templates. In Fig. 14, we further separate our “AGN A” and “AGN B” templates into two panels for clarity.

We find that our “AGN A” template, and its uncertainties, is fully consistent with some recent average SEDs derived for Type-I AGNs (Mor & Netzer 2012), Type-I QSOs (Xu et al. 2020), and the hot dust deficient (HDD) and warm dust deficient (WDD) QSOs of Lyu et al. (2017; see left-hand side panel in Fig. 14). The latter are populations of QSOs which appear to have lower emission in the near-to-far-IR, and the mid-to-far-IR, respectively, when compared to the typical QSO template of Elvis et al. (1994). However, we note that, once normalised to L_{IR} , the HDD and WDD appear very similar, though with MIR whose is consistent with the upper band of the 1σ uncertainties of our “AGN A” template (see Fig. 14).

More importantly, our “AGN A” template agrees well with studies finding hotter AGN SEDs (less contribution to the FIR), and do not show evidence supporting the recent claims that the IR emission of QSOs is cooler than previously thought (i.e. Symeonidis et al. 2016; Lani et al. 2017). In fact, Fig. 14 shows that our average “AGN A” template offers even less FIR contribution than the hottest QSO SEDs of Mor & Netzer (2012) and Xu et al. (2020). Nevertheless, we note that the differences in the FIR (i.e. integrated at $\lambda > 70 \mu\text{m}$) is typically below a few per cent. This is consistent with the largest discrepancies found in the average QSO SEDs of Xu et al. (2020) while testing various libraries for galaxy emission.

To construct a library for AGN IR emission, Xu et al. (2020) used a grid of AGN templates built on the phenomenological torus model of Siebenmorgen et al. (2015), which represents a completely different approach to that presented here. In particular, the grid of AGN models constructed in Xu et al. (2020) contains AGN templates which show a very large AGN contribution to the FIR, including that reported in Symeonidis et al. (2016), which is the template that, like-for-like, has the largest relative contribution to the FIR. Nevertheless, the average quasar template from Xu et al. (2020) also shows a hotter SED, consistent with our “AGN A” template.

By contrast, our “AGN B” template shows a different distribution of power, where most of the IR output is coming from cooler dust when compared to our “AGN A” template (i.e. $20 \mu\text{m} < \lambda < 50 \mu\text{m}$). The MIR emission of our “AGN B” template is consistent with that previously reported for more typical, less luminous AGNs of Mullaney et al. (2011). In particular, we note the presence of a strong IR bump at $\lambda \sim 18 \mu\text{m}$, consistent with that found in Mullaney et al. (2011) at $\sim 19 \mu\text{m}$. However, we find that our “AGN B” template is hotter, and produces less relative FIR output than found in Mullaney et al. (2011). We note that Mullaney et al. (2011) did not have readily available access to *Herschel* data, and as such their FIR SED is based on an extrapolation from shorter wavelengths.

One of the major challenges in extracting the AGN contribution to the FIR, and which could potentially explain the differences between AGN templates, is to accurately estimate, and preferably remove, that arising from the host galaxy. A popular method used in previous studies consisted of selecting optically bright QSOs, and assuming that the full IR SEDs is dominated by emission from the AGN, as in Elvis et al. (1994), or to rely on generic host-to-SMBH relationships to estimate and remove the *minimum* host contamination, as in Richards et al. (2006). Both these methods tend to significantly over-estimate the AGN contribution to the FIR, as shown by Xu et al. (2015), who corrected the Elvis et al. (1994) AGN SED for contribution from the host galaxy.

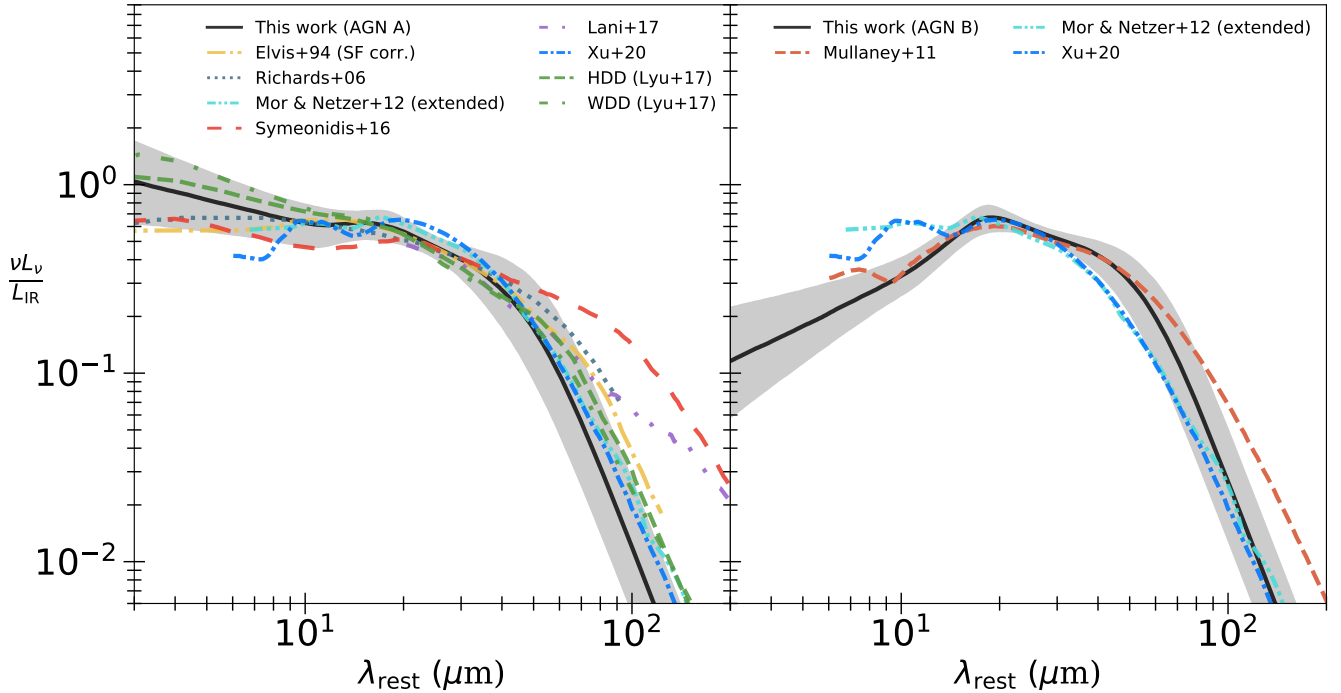


Figure 14. Our two AGN continuum templates, defined in § 3.2.3, compared to templates taken from previous studies. *Left panel:* Our “AGN A” template compared against the AGN templates for QSOs of [Elvis et al. \(1994\)](#); corrected for host contribution by [Xu et al. \(2015\)](#), [Richards et al. \(2006\)](#), [Symeonidis et al. \(2016\)](#), [Lani et al. \(2017\)](#), and [Xu et al. \(2020\)](#), the template for optically selected Type-I AGNs of [Mor & Netzer \(2012\)](#); extended at $\lambda > 35 \mu\text{m}$ by [Netzer et al. \(2016\)](#), and the templates for the hot dust deficient (HDD) and the warm dust deficient (WDD) QSOs of [Lyu et al. \(2017\)](#). The grey area shows the 1σ uncertainties of our “AGN A” template. *Right panel:* Our “AGN B” template compared against AGN templates for the more typical, less luminous AGNs of [Mullaney et al. 2011](#), the template for optically selected Type-I AGNs of [Mor & Netzer \(2012\)](#), and the template for Type-I QSOs of [Xu et al. \(2020\)](#). The grey area shows the 1σ uncertainties of our “AGN B” template. Each of the AGN templates presented in this figure has been renormalised to L_{IR} (i.e. integrated from $8 \mu\text{m}$ to $1000 \mu\text{m}$) to avoid comparison biases due to the choice of the normalisation.

Another popular method of removing the host contribution is to rely on the observed PAH features, since they are believed to be associated with star formation, and use star-forming galaxy templates to estimate the host contribution to the FIR (e.g. [Xu et al. 2015](#); [Symeonidis et al. 2016](#); [Lani et al. 2017](#)). However, the accuracy of this method strongly depends on the quality of the MIR spectra, as well as the library of galaxy templates used to extrapolate to the FIR ([Lyu & Rieke 2017](#); [Xu et al. 2020](#)). In fact, [Xu et al. \(2020\)](#) showed that by using a library of galaxy templates which does not account for the silicate trough at $9.7 \mu\text{m}$ (e.g. [Chary & Elbaz 2001](#); [Dale & Helou 2002](#); [Dale et al. 2014](#)), the host contribution to the FIR is systematically under-estimated by a factor of ~ 1.6 -to- 1.8 , leading to larger estimates of the AGN contribution to the FIR. Our templates (galaxy and AGN) are less likely to be affected in such a way since we have factored-in obscuration. However, we note that the treatment of obscuration alone cannot fully explain the differences in the shapes of AGN SEDs in the FIR, as [Lyu et al. \(2017\)](#) and [Xu et al. \(2020\)](#) both considered silicate absorption, yet found slightly cooler SEDs.

Finally, we note that the observed differences between ours and others’ FIR AGN template contribution to the FIR cannot also solely be attributed to the differences in galaxy templates. In fact, both [Netzer et al. \(2016\)](#), which is a FIR extension of the [Mor & Netzer \(2012\)](#) template, and [Lani et al. \(2017\)](#) used the galaxy library of [Chary & Elbaz \(2001\)](#), and found significantly different AGN contributions to the FIR (see Fig. 14). However, while [Lani et al. \(2017\)](#) used a sample of local bright QSOs with $L_{\text{bol}} \sim 4 \times 10^{43-46} \text{ erg s}^{-1}$, [Netzer et al. \(2016\)](#) focused on a sample of very luminous optically selected AGNs with $L_{\text{bol}} \gtrsim 2 \times 10^{47} \text{ erg s}^{-1}$ at $2 < z < 3.5$, which could explain the differences between the two. In addition, the modelling conducted by [Netzer et al. \(2016\)](#) required that the galaxy dominates over the AGN at wavelengths around $60 \mu\text{m}$. This is, in essence, very similar to our prior on the position of the break, implemented in our modelling, and which slowly drops at $\lambda_{\text{break}} > 40 \mu\text{m}$ (see § 3.2.2). This could explain the similarities in the FIR between our AGN templates and that of [Mor & Netzer \(2012\)](#), but also bias the typical AGN SED toward a smaller contribution to the FIR (i.e. hotter SED).

Another popular method of removing the host contribution is to rely on the observed PAH features, since they are believed to be associated with star formation, and use star-forming galaxy templates to estimate the host contribution to the FIR (e.g. [Xu et al. 2015](#); [Symeonidis et al. 2016](#); [Lani et al. 2017](#)). However, the accuracy of this method strongly depends on the quality of the MIR spectra, as well as the library of galaxy templates used to extrapolate to the FIR ([Lyu & Rieke 2017](#); [Xu et al. 2020](#)). In fact, [Xu et al. \(2020\)](#) showed that by using a library of galaxy templates which does not account for the silicate trough at $9.7 \mu\text{m}$ (e.g. [Chary & Elbaz 2001](#); [Dale & Helou 2002](#); [Dale et al. 2014](#)), the host contribution to the FIR is systematically under-estimated by a factor of ~ 1.6 -to- 1.8 , leading to larger estimates of the AGN contribution to the FIR. Our templates (galaxy and AGN) are less likely to be affected in such a way since we have factored-in obscuration. However, we note that the treatment of obscuration alone cannot fully explain the differences in the shapes of AGN SEDs in the FIR, as [Lyu et al. \(2017\)](#) and [Xu et al. \(2020\)](#) both considered silicate absorption, yet found slightly cooler SEDs.

4.2 Intrinsic differences between our “AGN A” and “AGN B” templates

Once normalised to L_{IR} , our “AGN B” template is cooler (i.e. shows a stronger relative FIR emission) than our “AGN A” template (see Fig. 14). In this sub-section we investigate the potential reasons behind such an anisotropy. This could arise either from an excess of relative extinction, or by an “intrinsic dust emission anisotropy” resulting from the torus shape of the dusty structure around the AGN, and unified via the AGN unification scheme ([Antonucci 1993](#); [Urry & Padovani 1995](#)). We stress that for the former, although we have removed to some extent the extinction along the line of sight, it is possible that some degrees of extinction remain due to the complexity of the dusty structures in AGNs.

Several physical mechanisms are at work, each affecting the

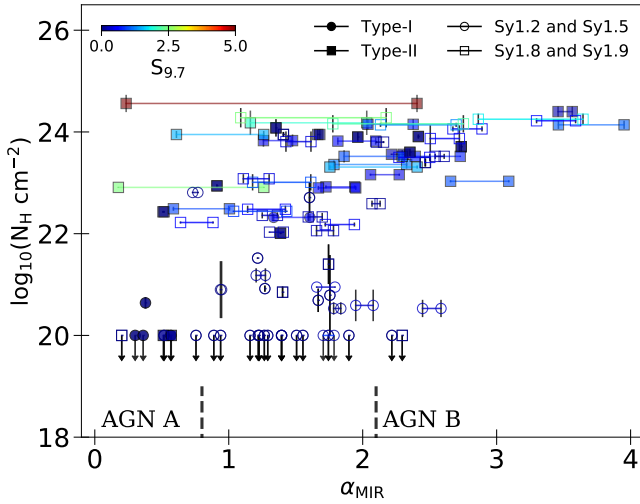


Figure 15. Plot showing the relationship between the column density of gas N_H and the average MIR slope α_{MIR} (i.e. average between α_1 and α_2 ; see § 3.2.1) found in our sample of AGNs, split in terms of AGN types (see keys), and colour coded by the strength of the observed silicate absorption at $9.7 \mu m$ (see the colour bar in the top left-hand side corner). The lines connecting two symbols show the effect of dust obscuration on the slopes α_{MIR} , where the connected right-hand symbol and left-hand symbol correspond to the absorbed and the de-absorbed values, respectively. The arrows on the symbols indicate upper limits for N_H . The dashed line and dot-dashed line show the average MIR slope of our “AGN A” and “AGN B” templates.

shape of the intrinsic, and/or the observed IR AGN SEDs. To better understand the physical mechanisms leading to such an anisotropy in the average IR emission of AGNs, we combined together several observations tracing different emission/absorption mechanisms for our sample of AGNs fit with *IRAGNSEP*. First, we considered the column densities of N_H (taken from Ricci et al. 2017a), mainly responsible for the absorption of X-rays. Then, we looked at the optical type of each of our AGNs (using the classifications reported in Oh et al. 2018), providing information on the optical “visibility” of the central engine. We further traced the amount of obscuring material present along the line of sight by using the measured total absorption at $9.7 \mu m$, $\Theta(\tau_{9.7})$, converted to $S_{9.7}$, using,

$$S_{9.7} \equiv - \ln \left(\frac{F_{9.7\mu m}^{Obs}}{F_{9.7\mu m}^{Int}} \right), \quad (7)$$

where $F_{9.7\mu m}^{Obs}$ and $F_{9.7\mu m}^{Int}$ are the observed and the intrinsic (i.e. de-absorbed) fluxes at $9.7 \mu m$, respectively. Finally, we have the MIR slopes, α_{MIR} , used to separate our two AGN templates (see § 3.2.3) to probe the “temperature” of the AGN continuum, where flatter slopes correspond to hotter SEDs, and steeper slopes to cooler SEDs. For α_{MIR} , we also compared the intrinsic slopes, as corrected by our prescription for dust obscuration, to the observed ones.

In Fig 15 we show all these parameters combined, where the abscissa is the slope α_{MIR} , and the ordinate is the column density of gas N_H . The symbols show the optical types, where circles and squares are for Type-I and Type-II AGNs, respectively (intermediate types are shown with open symbols), and the colour code indicates the strength of the silicate absorption at $9.7 \mu m$. In Fig 15, each of the AGNs has two α_{MIR} slopes connected with a line and indicating

the absorbed (right-hand point) and de-absorbed (left-hand point) α_{MIR} slope. The larger $S_{9.7}$, the larger the distance between the two.

Within the context of the simplest version of the AGN unification scheme, a single universal intrinsic AGN IR SED should be valid for all of our sources, and the differences observed should be attributed to dust obscuration along the line of sight. However, we note from Fig. 15 that this is not the case, and our sources show a wide range of α_{MIR} , even after correcting for dust obscuration based on the strength of the silicate absorption at $9.7 \mu m$. This justifies the need for our “AGN B” template which represents sources with somewhat steeper “intrinsic” α_{MIR} .

Although obscuration does not appear to be the obvious reason behind the differences between our two AGN templates, we still find a mild trend for more dust-obscured sources (lighter blue in Fig. 15) to have larger column densities of gas (i.e. $N_H > 10^{22} \text{ cm}^{-2}$), and to be classified as optical Type-II AGNs (square symbols in Fig. 15). In fact, it is believed that dust in the host galaxy is responsible for the silicate absorption trough at $9.7 \mu m$ (e.g. Deo et al. 2009; Goulding et al. 2012). By using this feature to correct for absorption, it is likely that we are not sensitive to the level of nuclear absorption.

Furthermore, it is now clear that dusty structures in AGNs (i.e. those responsible for the nuclear obscuration) are more complex than the classical equatorial dusty torus. In fact, IR interferometry has recently shown that the parsec-scale MIR emission of some AGNs has a stronger polar-extended component, when compared to the classical equatorial dust (e.g. Hönig et al. 2013; Leftley et al. 2018). In addition, it was shown that this component can extend up to scales of tens-to-hundreds of parsecs, which is similar to scales observed for the narrow-line-emitting region of the AGN (e.g. Radomski et al. 2003; Asmus et al. 2016). Therefore, the unified AGN orientation scenario has been re-visited to account for the discovery of the extended polar dust (see Ogawa et al. 2021, and references therein). It was further proposed that extended AGN polar dust creates a cooler component in the IR SEDs of AGNs, peaking at $\lambda \sim 30 \mu m$ (e.g. Hönig et al. 2011; Lyu & Rieke 2018). In light of these, we suggest that our “AGN A” template represents the typical unobscured Type-I sources, for which both, the AGN and the galaxy are face-on. In addition, our “AGN A” template also represents the absorption-corrected Type-II sources for which the main dust obscuring material is located in the host galaxy (i.e. face-on AGN at the centre of an edge-on galaxy disk, or with coincident galactic dust lanes).

By contrast, we suggest that our “AGN B” template represents sources that, in addition to galactic intervening dust material, are suffering from significant nuclear obscuration. In such cases, the hotter dust contribution is fully or partly absorbed (i.e. depending on the amount of intervening dust in the line of sight), and only the extended AGN-heated dust components, such as the extended polar dust, are recovered. The source UGC3601 in Fig. 11 is a good example as it shows no evidence for silicate absorption, has a low column density of gas (i.e. $N_H = 2.5 \times 10^{21} \text{ cm}^{-2}$) with significant silicate emission, though shows a rising α_{MIR} , and is classified as a Seyfert 1.9 galaxy, meaning that only broad $H\alpha$ lines are detected.

Perhaps more interestingly, we find that intermediate Seyfert-type galaxies follow a better relationship between the column density of gas, N_H , and α_{MIR} slope, yet show minimum silicate absorption (see Fig. 15). In fact, by inspecting their IR SEDs, we found that Seyfert 1.2 and Seyfert 1.5 AGNs mostly show a rising MIR continuum and mild silicate emission with the absence of strong silicate absorption, and Seyfert 1.8 and Seyfert 1.9 AGNs also show a rising MIR continuum, yet no silicate emission or absorption (see also Deo et al. 2009). It is possible that intermediate Seyfert galaxies

are free of galactic dust extinction, and that only nuclear obscuration (i.e. via the torus and/or the extended polar dust) affects the light. We reserve further analysis regarding the connection between the shape of the IR SED of AGNs to the unified scheme to future study, and assume for the rest of this discussion that nuclear obscuration is responsible for the differences between our “AGN A” and “AGN B” templates, and that the latter is dominated by AGN-heated dust at larger scales.

We note that some studies included an extra parameter representing obscuration in their fits to account for the full diversity of MIR slopes (e.g. [Del Moro et al. 2013, 2016](#)). In fact, we find that both our AGN templates are necessary to fit the photometric SEDs of our sample of AGNs, where the “AGN A” and “AGN B” templates are best fitting 43 per cent and 57 per cent of the SEDs, respectively, when sufficient photometry measurements are available to constrain the MIR slope. It is useful to bear in mind that using templates is less demanding, and less susceptible to degeneracies than adding a free obscuration parameter in the fit, as in [Del Moro et al. \(2016\)](#).

4.3 The relationship between AGN luminosity and the AGN far-IR emission

It was suggested in [Mullaney et al. \(2011\)](#) that less powerful AGNs (i.e. where less powerful means $L_X^{2-10} < 10^{42.9} \text{ erg s}^{-1}$, i.e., below the median L_X^{2-10} of their sample) tend to show cooler emission (i.e. contribute more to the FIR) than their higher X-ray luminosity counterparts. To assess whether our templates also show this trend, we split our sample into two sub-samples according to bolometric luminosity (L_{bol}). We calculated L_{bol} by first converting the 14–195 keV to 2–10 keV luminosities, using the photon indices found in [Oh et al. \(2018\)](#), then convert these 2–10 keV luminosities to L_{bol} , using the average bolometric correction of 22.4 reported in [Vasudevan & Fabian \(2007\)](#). We split our sample at $L_{\text{bol}} = 10^{44.2} \text{ erg s}^{-1}$, which is equivalent to the value used in [Mullaney et al. \(2011\)](#), after we converted their 2–10 keV luminosities to L_{bol} .

We show in Fig. 16 the average AGN continuum SEDs split into bins of L_{bol} . Although we find that lower luminosity AGNs have a higher FIR-to-MIR relative emission when compared to their higher luminosity counterparts, we do not find any strong differences between the positions of the break, as suggested in [Mullaney et al. \(2011\)](#).

The lack of a relationship between L_{bol} and the contribution to the FIR, when considering our whole sample, is also in apparent contradiction with [Xu et al. \(2020\)](#), which reported that more optically luminous quasars (i.e. using the 5100Å luminosity; L_{5100}) show cooler SEDs than their optically less luminous counterparts. To test this in our AGN sample, we derived average SEDs for our Type-I AGNs alone, which are similar sources to those in [Xu et al. \(2020\)](#), after splitting the sample at $L_{\text{bol}} = 10^{45.5} \text{ erg s}^{-1}$. The latter corresponds to the divide adopted in [Xu et al. \(2020\)](#), after converting their L_{5100} to L_{bol} using a factor of ten ([Richards et al. 2006](#)). In doing this, we find that more powerful Type-I AGNs show, on average, a cooler SED when compared to their less powerful counterparts, in agreement with [Xu et al. \(2020\)](#); see Fig. 16). In fact, on average, the position of the break shifts from $\lambda_{\text{break}} \sim 35 \mu\text{m}$ to $\lambda_{\text{break}} \sim 50 \mu\text{m}$, from lower-to-higher luminosity Type-I AGNs, while the MIR-to-FIR relative emission remains similar. We stress, however, that our sub-sample of Type-I AGNs is small, containing only four and three sources at higher and lower bolometric luminosities, respectively.

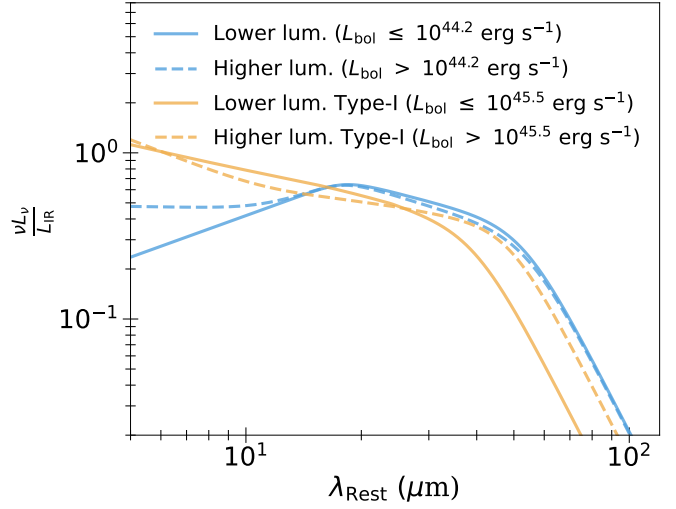


Figure 16. Plot showing the average AGN SEDs in bins of bolometric luminosities. The continuous and the dashed blue lines show the average SEDs of the full sample split at $L_{\text{bol}} = 10^{44.2} \text{ erg s}^{-1}$, which corresponds to the same split as in [Mullaney et al. \(2011\)](#), while the continuous and the dashed orange lines show the average SEDs for Type-I AGNs in our sample, split at $L_{\text{bol}} = 10^{45.5} \text{ erg s}^{-1}$, which corresponds to the same split as in [Xu et al. \(2020\)](#).

The differences in the relationship between L_{bol} and the FIR AGN contribution observed for our full sample and the Type-I sources could potentially be related to the Eddington ratio. In fact, [Ricci et al. \(2017b\)](#) found that only higher Eddington ratio AGNs have the ability to clear-out the obscuring material, and, for those, a relationship is expected between AGN power and the FIR luminosity of the AGN (see also [Ogawa et al. 2021](#)). A full analysis of the shapes of IR AGN SEDs and how it changes with λ_{Edd} is beyond the scope of this paper, and left for future work.

5 CONCLUSION

In this work we have investigated the intrinsic AGN IR emission of AGNs selected from the 105-month *Swift*–BAT all-sky hard X-ray survey. Our sample is typical of local ($z < 0.3$) low-to-high X-ray luminosity AGNs (i.e. $L_{\text{bol}} \sim \times 10^{42-46} \text{ erg s}^{-1}$; see Fig. 1). For the IR counterparts, we used archival *Spitzer*–IRS spectra ($5 \mu\text{m} < \lambda < 40 \mu\text{m}$), as well as *Herschel*–PACS and *Herschel*–SPIRE photometry ($70 \mu\text{m}$ – $500 \mu\text{m}$) for which we have corrected the flux for spatially extended emission (see § 2.2.1). Our final sample consists of 100 AGN SEDs covering most of the IR portion of the electromagnetic spectrum (see Fig. 2).

Prior to extracting the intrinsic AGN IR emission we defined a set of templates for galaxy emission using a sample of 110 star-forming galaxies pre-selected based on the $\text{EW}_{6.2\mu\text{m}}^{\text{PAH}}$ and the WISE colours W1 and W2 (see § 3.1). After fitting their SEDs, we discarded an extra 50 per cent of this sample as they show potential mild AGN contamination (see § 3.1.3), and kept 55 galaxies that we used to build eight templates for star-forming galaxies (see § 3.1.4). Specifically, we have one template that represents the PAH emission, and six templates that represent the dust continuum emission. Using the best fits, we defined Eq. 4 to evaluate the normalisation of the dust continuum using the PAH features observed in the MIR to within a scatter of 0.3 dex (see § 3.1.4).

To account for the AGN emission we defined a flexible model that represented continuum emission and silicate features (see § 3.2.1). By fitting our AGN SEDs with a combination of each of our galaxy templates plus our full AGN model (see § 3.2.2), we extracted a new set of three IR templates for AGN (see § 3.2.3). Two of the templates correspond to continuum emission (“AGN A” and “AGN B”), and one corresponds to silicate emission (see Fig. 12). The most important features of our two AGN continuum templates is the MIR slope, with “AGN B” showing a rising MIR emission compared to “AGN A”.

We compared our two AGN continuum templates to previous work and found that our “AGN A” template was consistent with some of the most recent AGN templates derived for (local) Type-I AGNs and QSOs, for which the host contributions have been correctly accounted-for. By contrast, our “AGN B” template was in better agreement with AGN SEDs measured in low-to-moderate X-ray luminosity AGNs (see § 4.1 and Fig. 14). We further found that, overall, our AGN templates show a hotter SED when compared to previous work, yet the differences in the FIR are minimal, and can be explained by the use of different libraries of galaxy templates.

We also found that, in general, the differences between our “AGN A” and “AGN B” templates can be explained by nuclear obscuration, and the presence of extended AGN polar dust. We suggested that, while our “AGN A” template is typical of sources for which there is no, or minimal, amount of nuclear obscuration, our “AGN B” template represents sources which suffer from nuclear obscuration which cannot be easily removed. For the latter, the SED is dominated by the emission of the extended AGN-heated polar dust, and the hotter dust contributions are, to some extent, suppressed.

After splitting our AGN sample into two bins of X-ray luminosity, we found that less powerful AGNs have a stronger relative FIR-to-MIR energy balance, when compared to more powerful AGNs, but the former do not show any evidence for an excess of FIR emission, in contrast with results reported in Mullaney et al. (2011). However, we found that the average SED for more powerful Type-I sources is cooler (i.e. contributes more to the FIR), when compared to their less powerful counterparts. This is in agreement with the findings reported in Xu et al. (2020), where more optically luminous AGNs show cooler SEDs (i.e. contribute more to the FIR) when compared to less optically luminous AGNs (see § 4.3).

Lastly, we have developed IRAGNSEP – a python-based package that can be used to decompose the IR SEDs of AGNs (see § 3.3). The default templates included in IRAGNSEP are those that we have presented in this work, and can be downloaded via <https://tinyurl.com/yawp96qc>. IRAGNSEP is freely available at <https://pypi.org/project/iragnsep/>.

ACKNOWLEDGEMENTS

We thank the anonymous referee for the useful comments that help to significantly improve the quality of the paper. EB, JRM, CT acknowledge STFC grant R/151397. DJR and DMA acknowledge the Science and Technology Facilities Council (grant codes ST/P000541/1 and ST/T000244/1). EB thanks Mouyuan Sun for the valuable discussion on the relationship between AGN luminosity and AGN contribution to the FIR. This research has made use of the NASA/IPAC Infrared Science Archive which is operated by the Jet Propulsion Laboratory, California Institute of Technology, under contract with the National Aeronautics and Space Administration. This research has made use of the SIMBAD database,

operated at CDS, Strasbourg, France. The following packages were used for the data reduction and analysis: MATPLOTLIB (Hunter 2007), ASTROPY (Astropy Collaboration et al. 2018), NUMPY, SCIPY (Virtanen et al. 2020), PANDAS (McKinney 2010), and NUMBA (Lam et al. 2015). This research made use of Photutils, an Astropy package for detection and photometry of astronomical sources (Bradley et al. 2020).

DATA AVAILABILITY STATEMENT

The data underlying this article were accessed from the IRSA database (<https://irsa.ipac.caltech.edu/frontpage/>), the *Swift* observatory archive (<https://swift.gsfc.nasa.gov/results/bs105mon/>), and the CASSIS database (<https://cassis.sirtf.com>). Our analysis led to new data that are shared in the supplementary material, or directly available at https://github.com/epbernhard/iragnsep_paper.

REFERENCES

- Aird J., Coil A. L., Georgakakis A., Nandra K., Barro G., Pérez-González P. G., 2015, *MNRAS*, **451**, 1892
- Akaike H., 1973, *Biometrika*, **60**, 255
- Akaike H., 1994, in Bozdogan H., Sclove S. L., Gupta A. K., Haughton D., Kitagawa G., Ozaki T., Tanabe K., eds., , *Proceedings of the First US/Japan Conference on the Frontiers of Statistical Modeling: An Informational Approach: Volume 3 Engineering and Scientific Applications*. Springer Netherlands, Dordrecht, pp 27–38, doi:10.1007/978-94-011-0854-6_2, http://dx.doi.org/10.1007/978-94-011-0854-6_2
- Antonucci R., 1993, *ARA&A*, **31**, 473
- Armus L., et al., 2007, *ApJ*, **656**, 148
- Asmus D., Hönig S. F., Gandhi P., 2016, *ApJ*, **822**, 109
- Assef R. J., et al., 2013, *ApJ*, **772**, 26
- Astropy Collaboration et al., 2018, *AJ*, **156**, 123
- Barthelmy S. D., et al., 2005, *Space Sci. Rev.*, **120**, 143
- Bradley L., et al., 2020, *Zenodo*
- Brandl B. R., et al., 2006, *ApJ*, **653**, 1129
- Burgarella D., Buat V., Iglesias-Páramo J., 2005, *MNRAS*, **360**, 1413
- Calistro Rivera G., Lusso E., Hennawi J. F., Hogg D. W., 2016, *ApJ*, **833**, 98
- Calzetti D., 2001, *PASP*, **113**, 1449
- Chabrier G., 2003, *PASP*, **115**, 763
- Chary R., Elbaz D., 2001, *ApJ*, **556**, 562
- Chen P. S., Yang X. H., Liu J. Y., Shan H. G., 2018, *AJ*, **155**, 17
- Chiar J. E., Tielens A. G. G. M., 2006, *ApJ*, **637**, 774
- Ciesla L., et al., 2015, *A&A*, **576**, A10
- Cresci G., Vanzì L., Telles E., Lanzuisi G., Brusa M., Mingozzi M., Sauvage M., Johnson K., 2017, *A&A*, **604**, A101
- Dale D. A., Helou G., 2002, *ApJ*, **576**, 159
- Dale D. A., Helou G., Contursi A., Silberman N. A., Kolhatkar S., 2001, *ApJ*, **549**, 215
- Dale D. A., Helou G., Magdis G. E., Armus L., Díaz-Santos T., Shi Y., 2014, *The Astrophysical Journal*, **784**, 83
- Del Moro A., et al., 2013, *A&A*, **549**, A59
- Del Moro A., et al., 2016, *MNRAS*, **456**, 2105
- Deo R. P., Richards G. T., Crenshaw D. M., Kraemer S. B., 2009, *ApJ*, **705**, 14
- Díaz-Santos T., et al., 2017, *ApJ*, **846**, 32
- Dicken D., Tadhunter C., Axon D., Morganti R., Inskip K. J., Holt J., González Delgado R., Groves B., 2009, *ApJ*, **694**, 268
- Dudik R. P., Satyapal S., Marcu D., 2009, *ApJ*, **691**, 1501
- Elvis M., et al., 1994, *ApJS*, **95**, 1

- Foreman-Mackey D., Hogg D. W., Lang D., Goodman J., 2013, *PASP*, **125**, 306
- Galliano F., et al., 2011, *A&A*, **536**, A88
- Gehrels N., et al., 2004, *ApJ*, **611**, 1005
- Goodman J., Weare J., 2010, *Communications in applied mathematics and computational science*, **5**, 65
- Goulding A. D., Alexander D. M., 2009, *MNRAS*, **398**, 1165
- Goulding A. D., Alexander D. M., Bauer F. E., Forman W. R., Hickox R. C., Jones C., Mullaney J. R., Trichas M., 2012, *ApJ*, **755**, 5
- Griffin M. J., et al., 2010, *A&A*, **518**, L3+
- Hao L., et al., 2005, *ApJ*, **625**, L75
- Hao L., Weedman D. W., Spoon H. W. W., Marshall J. A., Levenson N. A., Elitzur M., Houck J. R., 2007, *ApJ*, **655**, L77
- Harrison C. M., 2017, *Nature Astronomy*, **1**, 0165
- Hatziminaoglou E., Hernán-Caballero A., Feltre A., Piñol Ferrer N., 2015, *ApJ*, **803**, 110
- Hebbar P. R., Heinke C. O., Sivakoff G. R., Shaw A. W., 2019, *MNRAS*, **488**, 19
- Hirashita H., Deng W., Murga M. S., 2020, *MNRAS*, **491**, 171
- Hönig S. F., 2019, *ApJ*, **884**, 171
- Hönig S. F., Kishimoto M., 2010, *A&A*, **523**, A27
- Hönig S. F., Leipski C., Antonucci R., Haas M., 2011, *ApJ*, **736**, 26
- Hönig S. F., et al., 2013, *ApJ*, **771**, 87
- Houck J. R., et al., 2004, *ApJS*, **154**, 18
- Hunter J. D., 2007, *Computing in Science and Engineering*, **9**, 90
- Johnson K. E., Leitherer C., Vacca W. D., Conti P. S., 2000, *AJ*, **120**, 1273
- Kemper F., de Koter A., Waters L. B. F. M., Bouwman J., Tielens A. G. G. M., 2002, *A&A*, **384**, 585
- Kennicutt Jr. R. C., 1998, *ApJ*, **498**, 541
- Krügel E., 2009, *A&A*, **493**, 385
- Lam S. K., Pitrou A., Seibert S., 2015, in *Proceedings of the Second Workshop on the LLVM Compiler Infrastructure in HPC. LLVM '15*. Association for Computing Machinery, New York, NY, USA, doi:10.1145/2833157.2833162, <https://doi.org/10.1145/2833157.2833162>
- Lambrides E. L., Petric A. O., Tchernyshyov K., Zakamska N. L., Watts D. J., 2019, *MNRAS*, **487**, 1823
- Lani C., Netzer H., Lutz D., 2017, *MNRAS*, **471**, 59
- Laurent O., Mirabel I. F., Charmandaris V., Gallais P., Madden S. C., Sauvage M., Vigroux L., Cesarsky C., 2000, *A&A*, **359**, 887
- Lebouteiller V., Bernard-Salas J., Sloan G. C., Barry D. J., 2010, *PASP*, **122**, 231
- Lebouteiller V., Barry D. J., Spoon H. W. W., Bernard-Salas J., Sloan G. C., Houck J. R., Weedman D. W., 2011, *ApJS*, **196**, 8
- Leftley J. H., Tristram K. R. W., Hönig S. F., Kishimoto M., Asmus D., Gandhi P., 2018, *ApJ*, **862**, 17
- Li A., Draine B. T., 2001, *ApJ*, **554**, 778
- Lyu J., Rieke G. H., 2017, *ApJ*, **841**, 76
- Lyu J., Rieke G. H., 2018, *ApJ*, **866**, 92
- Lyu J., Rieke G. H., Shi Y., 2017, *ApJ*, **835**, 257
- Magdis G. E., et al., 2013, *A&A*, **558**, A136
- Martínez-Paredes M., et al., 2020, *ApJ*, **890**, 152
- Marton G., et al., 2017, arXiv e-prints,
- McKinney W., 2010, in van der Walt S., Millman J., eds, *Proceedings of the 9th Python in Science Conference*. pp 51 – 56
- Meléndez M., Mushotzky R. F., Shimizu T. T., Barger A. J., Cowie L. L., 2014, *ApJ*, **794**, 152
- Messias H., Afonso J., Salvato M., Mobasher B., Hopkins A. M., 2012, *ApJ*, **754**, 120
- Min M., Waters L. B. F. M., de Koter A., Hovenier J. W., Keller L. P., Markwick-Kemper F., 2007, *A&A*, **462**, 667
- Mor R., Netzer H., 2012, *MNRAS*, **420**, 526
- Mor R., Netzer H., Elitzur M., 2009, *ApJ*, **705**, 298
- Mullaney J. R., Alexander D. M., Goulding A. D., Hickox R. C., 2011, *MNRAS*, **414**, 1082
- Nenkova M., Sirocky M. M., Nikutta R., Ivezić Ž., Elitzur M., 2008, *ApJ*, **685**, 160
- Netzer H., et al., 2007, *ApJ*, **666**, 806
- Netzer H., Lani C., Nordon R., Trakhtenbrot B., Lira P., Shemmer O., 2016, *ApJ*, **819**, 123
- Noll S., Burgarella D., Giovannoli E., Buat V., Marcillac D., Muñoz-Mateos J. C., 2009, *A&A*, **507**, 1793
- Ogawa S., Ueda Y., Tanimoto A., Yamada S., 2021, *ApJ*, **906**, 84
- Oh K., et al., 2018, *ApJS*, **235**, 4
- Orellana G., et al., 2017, *A&A*, **602**, A68
- Peeters E., Mattioli A. L., Hudgins D. M., Allamandola L. J., 2004, *ApJ*, **617**, L65
- Pilbratt G. L., et al., 2010, *A&A*, **518**, L1+
- Poglitsch A., et al., 2010, *A&A*, **518**, L2
- Prieto M. A., Reunanen J., Tristram K. R. W., Neumayer N., Fernandez-Ontiveros J. A., Orienti M., Meisenheimer K., 2010, *MNRAS*, **402**, 724
- Radomski J. T., Piña R. K., Packham C., Telesco C. M., De Buizer J. M., Fisher R. S., Robinson A., 2003, *ApJ*, **587**, 117
- Reines A. E., Sivakoff G. R., Johnson K. E., Brogan C. L., 2011, *Nature*, **470**, 66
- Reines A. E., Reynolds M. T., Miller J. M., Sivakoff G. R., Greene J. E., Hickox R. C., Johnson K. E., 2016, *ApJ*, **830**, L35
- Ricci C., et al., 2017a, *The Astrophysical Journal Supplement Series*, **233**, 17
- Ricci C., et al., 2017b, *Nature*, **549**, 488
- Richards G. T., et al., 2006, *ApJS*, **166**, 470
- Rieke G. H., Alonso-Herrero A., Weiner B. J., Pérez-González P. G., Blaylock M., Donley J. L., Marcillac D., 2009, *ApJ*, **692**, 556
- Riffel R., et al., 2019, *MNRAS*, **486**, 3228
- Robotham A. S. G., Bellstedt S., Lagos C. d. P., Thorne J. E., Davies L. J., Driver S. P., Bravo M., 2020, *MNRAS*, **495**, 905
- Rosario D. J., et al., 2012, *A&A*, **545**, A45
- Sales D. A., Pastoriza M. G., Riffel R., 2010, *ApJ*, **725**, 605
- Samsyan A., Weedman D., Lebouteiller V., Barry D., Sargsyan L., 2016, *ApJS*, **226**, 11
- Sanders D. B., Mazzarella J. M., Kim D.-C., Surace J. A., Soifer B. T., 2003, *AJ*, **126**, 1607
- Sargsyan L., Weedman D., Lebouteiller V., Houck J., Barry D., Hovhannisyan A., Mickaelian A., 2011, *ApJ*, **730**, 19
- Schreiber C., et al., 2015, *A&A*, **575**, A74
- Schreiber C., Elbaz D., Pannella M., Ciesla L., Wang T., Franco M., 2018, *A&A*, **609**, A30
- Schulz B., et al., 2017, arXiv e-prints,
- Schulze A., et al., 2019, *MNRAS*, **488**, 1180
- Schweitzer M., et al., 2008, *ApJ*, **679**, 101
- Shimizu T. T., Meléndez M., Mushotzky R. F., Koss M. J., Barger A. J., Cowie L. L., 2016, *MNRAS*, **456**, 3335
- Siebenmorgen R., Haas M., Kruegel E., Schulz B., 2005, *Astronomische Nachrichten*, **326**, 556
- Siebenmorgen R., Heymann F., Efstathiou A., 2015, *A&A*, **583**, A120
- Smail I., Swinbank A. M., Ivison R. J., Ibar E., 2011, *MNRAS*, **414**, L95
- Smith J. D. T., et al., 2007, *ApJ*, **656**, 770
- Spoon H. W. W., Marshall J. A., Houck J. R., Elitzur M., Hao L., Armus L., Brandl B. R., Charmandaris V., 2007, *ApJ*, **654**, L49
- Stanley F., Harrison C. M., Alexander D. M., Simpson J., Knudsen K. K., Mullaney J. R., Rosario D. J., Scholtz J., 2018, *MNRAS*, **478**, 3721
- Stierwalt S., et al., 2014, *ApJ*, **790**, 124
- Sturm E., et al., 2005, *ApJ*, **629**, L21
- Su Y., Irwin J. A., White Raymond E. I., Cooper M. C., 2015, *ApJ*, **806**, 156
- Symeonidis M., Giblin B. M., Page M. J., Pearson C., Bendo G., Seymour N., Oliver S. J., 2016, *MNRAS*, **459**, 257
- Tadhunter C., et al., 2007, *ApJ*, **661**, L13
- Urry C. M., Padovani P., 1995, *PASP*, **107**, 803
- Vasudevan R. V., Fabian A. C., 2007, *MNRAS*, **381**, 1235
- Vika M., Ciesla L., Charmandaris V., Xilouris E. M., Lebouteiller V., 2017, *A&A*, **597**, A51
- Virtanen P., et al., 2020, *Nature Methods*,
- Wenger M., et al., 2000, *A&AS*, **143**, 9
- Xie Y., Ho L. C., Li A., Shangguang J., 2018, *The Astrophysical Journal*, **860**, 154

Xu L., Rieke G. H., Egami E., Pereira M. J., Haines C. P., Smith G. P., 2015, *ApJS*, **219**, 18

Xu J., Sun M., Xue Y., 2020, arXiv e-prints, p. [arXiv:2003.10078](https://arxiv.org/abs/2003.10078)

Yang G., et al., 2020, *MNRAS*, **491**, 740

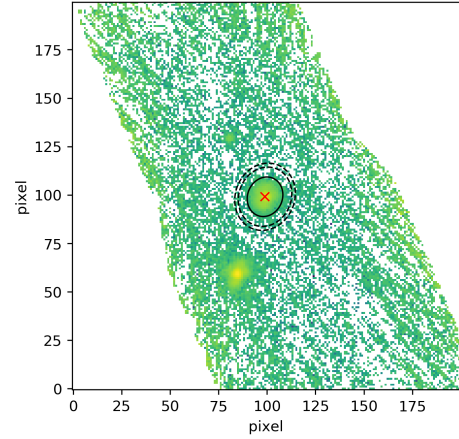
APPENDIX A: CALCULATING IR FLUXES FOR SPATIALLY EXTENDED SOURCES, AND COMPARISON WITH LITERATURE

To calculate IR fluxes we downloaded observation plates from the “*Herschel* High Level Images” products found in the IRSA database which contain a large collection of *Herschel* observations. We only used the data product levels 2.0 or above (maximum of 3.0) which correspond to levels on which scientific analysis can be performed. We used pointed observations when available, and survey data otherwise. While the maps for PACS (i.e. 70 μm , 100 μm , and 160 μm) are provided in Janskys (Jy) per pixel, those for SPIRE (i.e. 250 μm , 350 μm , and 500 μm) are given in Jy per beam. Therefore, we first converted the SPIRE maps from Jy per beam to Jy per pixel, using the size of the beams (469.35 arcsec^2 , 831.27 arcsec^2 , and 1804.31 arcsec^2), and the size of the pixels (6'' \times 6'', 10'' \times 10'', and 14'' \times 14'') at each of the SPIRE wavelengths (250 μm , 350 μm , and 500 μm), as reported in the *Herschel* observer manual.

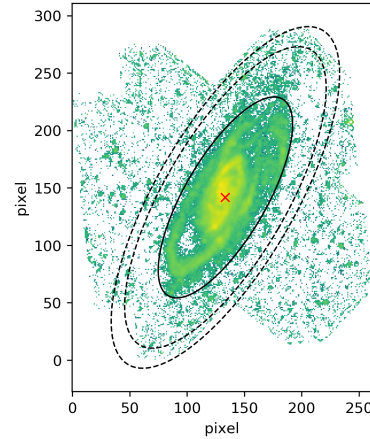
Once the images were converted to Jy per pixel, we used the Python package Photutils (Bradley et al. 2020) to analyse the images and to extract fluxes and their uncertainties. First, a median background map was created using sigma-clip statistics, after degrading the image with a five-by-five Gaussian kernel. Using this background map, we calculated the detection threshold of the image, using a one sigma limit. We then created a segmentation map (i.e. map flagging pixels above a certain value), using the detection threshold, and after degrading the image using a three-by-three Gaussian kernel. To identify the detections in survey images, we used the known position of the source. The extent of the source was calculated on the segmentation map by Photutils, and characterised by a semi-major and a semi-minor axis (1σ).

To extract the fluxes, we used an elliptical aperture on each cut-out, the size of which corresponded to three times the size of the corresponding semi-axes. We then summed the pixels within the elliptical aperture, and removed the median background to obtain the flux of the source in Jy. The uncertainties were estimated in an elliptical annulus where the inner and the outer edges were 1.5 and 1.7 times the elliptical aperture used to extract the flux, respectively. We added in quadrature an extra 3 per cent of the flux to the uncertainties, as we found that the true edges of extended sources were challenging to define, and a change of aperture to include more extended flux corresponded to a change in flux of roughly 3 per cent.

We show in Fig. A1 two examples of extended sources found in our AGN sample which were classified as point sources in the HPDPs. We also show the apertures used to extract the fluxes and their uncertainties. The top panel in Fig. A1 shows an example of a source that is barely extended, and for which our automated aperture flux extraction seemed to capture the full extent of the source. Instead, the bottom panel in Fig. A1 shows a source that is fully extended and for which we had to increase the size of the apertures to match the physical extent of the source. The fraction of the elliptical annulus that fell outside of the frame was ignored in the calculation of the uncertainties. In total, we had to modify the size of the aperture for roughly 30 per cent of our sources to ensure that all our apertures encompassed the totality of the source,



(a) UGC 7064 at 70 μm .



(b) NGC 4258 at 250 μm .

Figure A1. Two examples of extended sources found in our AGN sample. The panel (a) shows an example of a barely extended source, and the panel (b) shows a fully extended source where features like spiral arms are visible. Both these sources were classified as point sources in the HPDPs. The inner solid ellipse represents the aperture that were used to extract the flux, and the dashed elliptical annulus shows that of the uncertainties. The red cross corresponds to the centre of the ellipses.

and that no extended flux was missed. The full sets of images for our extended sources are available in the supplementary material, or directly at <https://tinyurl.com/yazhbx7p> and <https://tinyurl.com/yde5eptk> for the AGN and the star-forming galaxy samples, respectively.

Overall, we find that 30 per cent, 20 per cent, 55 per cent, 62 per cent, 58 per cent, and 45 per cent of our sources have been misclassified as point sources in the HPDPs at 70 μm , 100 μm , 160 μm , 250 μm , 350 μm , and 500 μm , respectively, as shown in Fig. A2 with open grey squares. We note that this mostly affects bright sources (likely to be at lower redshifts) at SPIRE wavelengths. In addition, a vast majority of sources that were undetected at 500 μm in the HPDP are now detected due to the larger aperture used to calculate the fluxes. In addition, we find that all of our *Herschel* fluxes are fully consistent with those overlapping with Meléndez et al. (2014) for PACS at 70 μm and 160 μm , and from

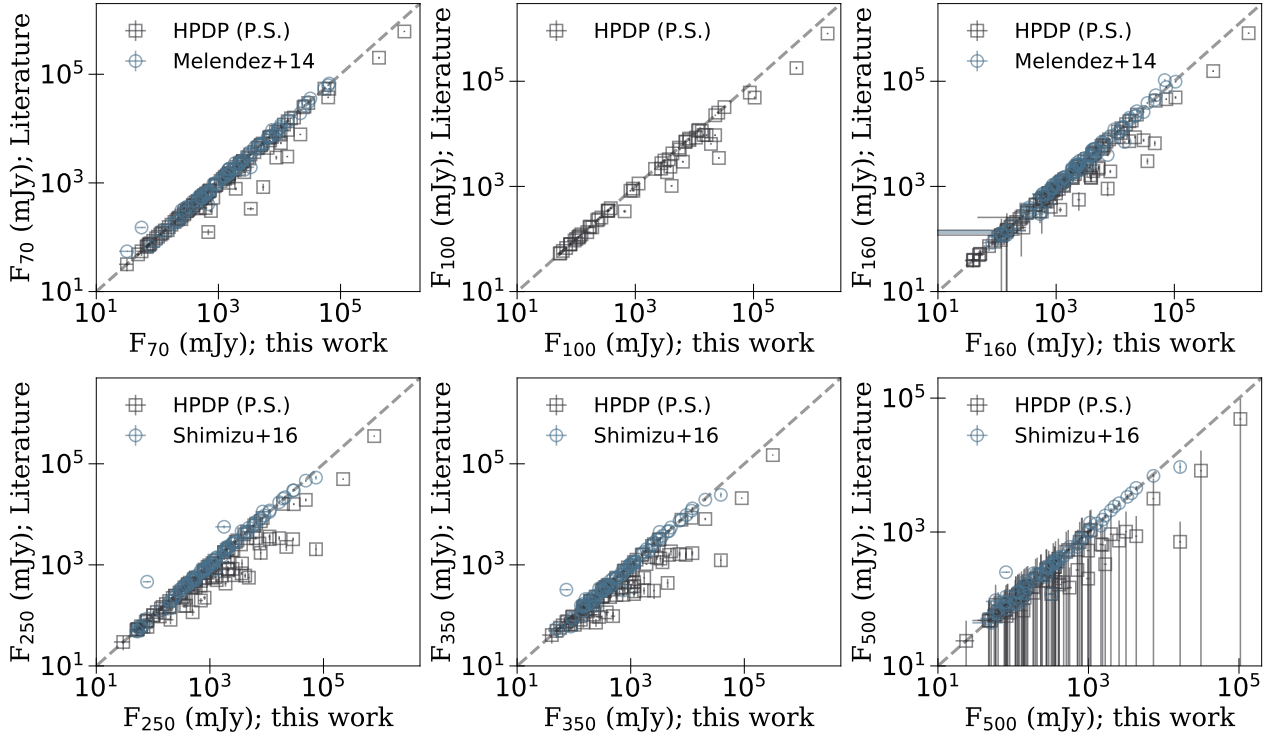


Figure A2. The fluxes used in this work, corresponding to the HPDP fluxes for point sources and to our own fluxes for spatially extended sources, against the HPDP fluxes (open grey squares), and the fluxes from Meléndez et al. (2014) for PACS at 70 μm and 160 μm , and from Shimizu et al. (2016) for SPIRE (open blue circles). Each panel corresponds to an *Herschel* wavelength, from 70 μm to 500 μm , and increases in reading order. The dashed grey line in each of the panels shows the 1:1 relationship.

Shimizu et al. (2016) for SPIRE, where extended sources were correctly accounted for (see Fig. A2).

APPENDIX B: DETAILED ANALYSIS OF THE FAILED FITS

While attempting to fit the IR SEDs of our pre-selected star-forming galaxies (based on $\text{EW}_{6.2\mu\text{m}}^{\text{PAH}}$ and WISE colours), we found a large fraction (i.e. 50 per cent) for which the galaxy model of S18, split in terms of PAHs and dust continuum, failed. For each of these sources, we carefully inspected their SEDs and searched the NED database to find evidence of misclassification.

First, we directly discarded IC 342 (aorkey = 9072128) which is a well known star-forming galaxy, yet its redshift of $z = 0.0001$ and spatial extent are such that, at the resolution of the *Spitzer*-IRS spectra, only the central starburst was observed, and a simple re-scaling was not sufficient. We then also directly discarded NGC4676 (aorkey = 9073152), NGC1141 (aorkey = 4830976), and MCG+06-32-058 (aorkey = 14081536) as their *Herschel* fluxes were enhanced by blended companions which could not be easily deblended (the images can be found in the supplementary material and at <https://tinyurl.com/yde5eptk>). Finally, we directly discarded WISEAJ000024.24-525031.0 (aorkey = 17863936) as its large attenuation is such that our prescriptions were not able to recover the observed fluxes. These five SEDs and their fits are shown in the leftmost panel of Fig. B1.

Second, we found 34 galaxies with potential AGN contamination in the IR. In particular, we considered the work of Vika et al. (2017), where the SED fitting code CIGALE (Burgarella et al. 2005;

Noll et al. 2009) was used on photometry spanning the UV to IR (up to 22 μm), including an AGN contribution. In addition, we used the work from Díaz-Santos et al. (2017) who combined up to five IR diagnostics, including emission line diagnostics, $\text{EW}_{6.2\mu\text{m}}^{\text{PAH}}$, MIR flux ratios, and the diagram from Laurent et al. (2000), to calculate an average IR AGN contamination. Finally, we also used AGN fractions reported in Magdis et al. (2013) where DECOMPIR (Mullaney et al. 2011) was used to decompose the IR SEDs of galaxies, including an AGN contribution. Although we found a large number of galaxies that could not be fit with S18 to have AGN IR contribution in the aforementioned studies, the fractions were generally low (i.e. typically less than 10–20 per cent) and ambiguous. For instance, WISEAJ103450.50+584418.2 (aorkey = 24153088) was found to have 2.1 ± 3.5 per cent or 64 ± 10 per cent AGN IR contributions in Vika et al. (2017) or Magdis et al. (2013), respectively. This shows the difficulties of accurately measuring the AGN fraction at IR wavelengths, as well as the importance of distinguishing the AGN component from that of the galaxy, even when the AGN contributes at less than ~ 10 per cent of the IR.

We note that these are mainly unveiled via SED fits which, in turn, depend upon the accuracy of the star-forming galaxy templates used. However, by inspecting the SEDs, we noted the presence of multiple faint high-ionisation emission lines, such as [NeV] at 24 μm and [OIV] at 26 μm , in half of these galaxies, with a confirmed [NeV]-detected galaxy (i.e. ESO593-IG008 or aorkey = 20311296) in Dudik et al. (2009). Although this strongly suggests that these are genuine IR AGNs, we cannot exclude the possibility that some SEDs are less well fit due the spatial extent of the source and the resolution of the *Spitzer*-IRS instrument. The second leftmost panel of Fig. B1 shows five random examples amongst our 34 galaxies

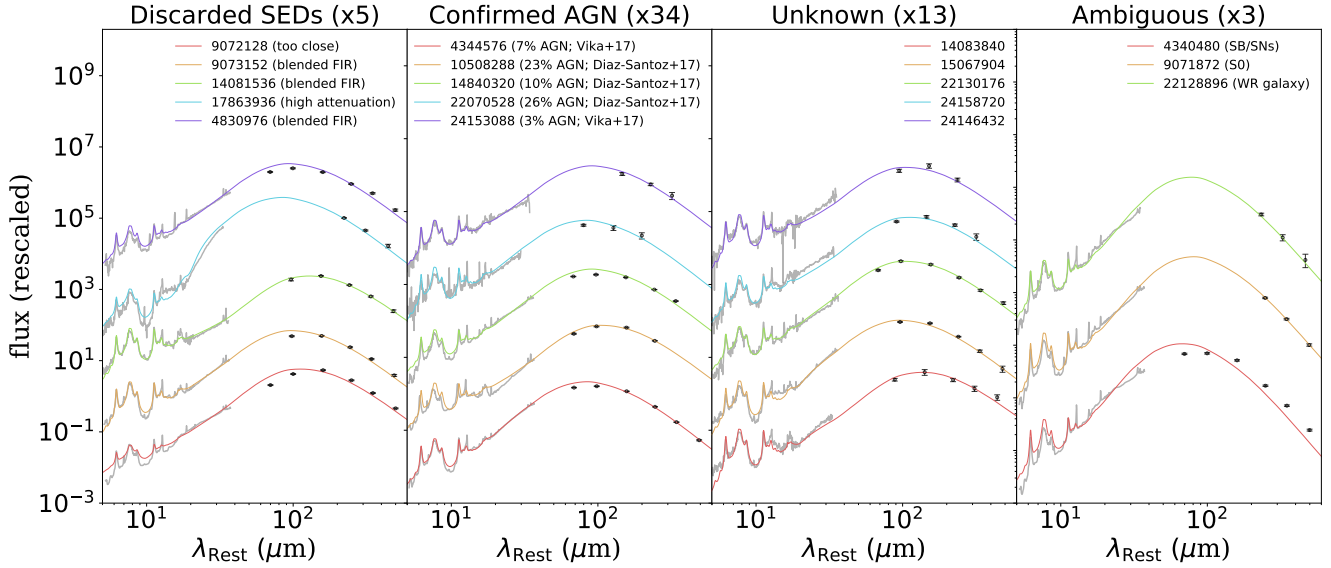


Figure B1. The SEDs that could not be fit by using the galaxy model of S18. We separated the full set of failed SEDs into four bins (see panels), as indicated at the top of each panel. The “discarded SEDs” were SEDs for which we found intrinsic issues (i.e. blended photometry). The “confirmed AGNs” were found to have IR contamination in some previous studies. The “unknown” are SEDs for which we did not find any information regarding the AGN/galaxy contribution. Finally, the “ambiguous” are SEDs for which we found no evidence for AGN contribution in the IR based on previous work. The number next to the name of the bin indicates the total number of sources in the bin.

with potential IR AGN contribution. The full set of 34 individual SEDs can be found in the supplementary material, or directly at <https://tinyurl.com/ybu9jeg1>.

Third, we found 13 SEDs for which we could not find any references regarding an AGN (or lack of) at MIR wavelengths. For these we matched the SEDs with those from our confirmed AGNs, after normalising both at $15\ \mu\text{m}$. We found that, for each of these SEDs, we could find an identical matching MIR SED with confirmed AGN contamination, and which was differing in the FIR. Therefore, these are likely to also be contaminated by AGNs, and were discarded. The second to last panel of Fig. B1 show an example of five of these sources. The entire set of 13 SEDs can be found in the supplementary material, or directly at <https://tinyurl.com/ybu9jeg1>.

Finally, we were left with three sources for which we did not find any evidence of any AGN contribution, yet the model of S18 could not fit their SEDs. Firstly, Henize 2-10 (aorkey = 4340480; He2-10) is a remarkably compact starburst galaxy containing an abundant number of young super star clusters (e.g. Johnson et al. 2000). While Reines et al. (2011) speculated the presence of an AGN at the centre of He2-10 by finding an X-ray point source that coincides with a steep-spectrum radio source, further X-ray observations by Reines et al. (2016) revealed the presence of two sources, one coincident with the radio emission (with an X-ray luminosity of $L_X \sim 10^{38}\ \text{erg s}^{-1}$), and believed to be an AGN, and the other one showing no radio emission, and believed to be an X-ray binary. However, Cresci et al. (2017) found that the optical emission line diagnostics at the centre of He2-10 was fully consistent with star formation, and showed that the X-ray luminosity found previously was consistent with emission from supernovae. Finally, Hebbar et al. (2019) have recently found that SN models of X-ray emission explain much better the observed X-ray spectrum of He2-10 than an AGN power-law.

We then found that NGC1222 (aorkey = 9071872) has a matching SED to He2-10, suggesting the presence of a starburst. In fact,

NGC1222 is reported to be a lenticular S0 galaxy (Riffel et al. 2019), and was undetected in X-rays (Su et al. 2015). In addition, we found that WISEAJ155616.05+395137.8 (aorkey = 22128896) also has an SED which is identical to He2-10 and NGC1222, yet is reported as a Wolf-Rayet galaxy (Chen et al. 2018), and is therefore consistent with IR powered by star formation. Although these three galaxies were found to be consistent with starburst galaxies, we discarded them from our star-forming galaxy sample as (1) their SEDs were very similar to that of galaxies for which the MIR is contaminated by AGNs, and (2) because of their peculiar nature. The rightmost panel of Fig. B1 show the SEDs of these three galaxies.

APPENDIX C: TABLES

Table C1: The properties of our sample of 112 AGNs selected from the 105-month *Swift*–BAT all-sky hard X-ray survey of Oh et al. (2018) (see § 2). All of the columns are from Oh et al. (2018), aside for the column densities of N_{H} , which are from Ricci et al. (2017a). The positions are those of the counterparts. A machine-readable version of this table is available in the supplementary material, or directly at <https://tinyurl.com/yah2os8v>.

ID	<i>Swift</i> -BAT Name	Counterpart Name	R.A. (h:m:s)	Dec. (d:m:s)	z	$\log(L_X \text{ erg s}^{-1})$	Type	$\log(N_{\text{H}} \text{ cm}^{-2})$
1	J0900.9+2095	2MASXJ09003684+2053402	09:00:36.864	+20:53:40.560	0.235	45.1	Sy2	–
2	J0508.1+1727	2MASXJ05081967+1721483	05:08:19.680	+17:21:46.800	0.017	43.2	Sy1.9	22.33
3	J0516.2-0009	Ark120	05:16:11.424	-00:08:59.280	0.032	44.2	Sy1	20.0
4	J0138.6-4001	ESO297-18	01:38:37.152	-40:00:41.040	0.025	43.9	Sy2	23.83
5	J1306.4-4025A	ESO323-77	13:06:26.136	-40:24:52.560	0.015	43.1	Sy1.5	22.81
6	J0623.8-3215	ESO426-2	06:23:46.416	-32:12:59.760	0.022	43.4	Sy2	23.95
7	J0601.9-8636	ESO5-4	06:05:41.640	-86:37:54.840	0.006	42.4	Sy2	24.18
8	J1238.9-2720	ESO506-27	12:38:54.600	-27:18:28.080	0.025	44.1	Sy2	23.95
9	J1419.0-2639	ESO511-30	14:19:22.416	-26:38:40.920	0.022	43.6	Sy1	20.0
10	J0342.0-2115	ESO548-81	03:42:03.720	-21:14:39.840	0.014	43.2	Sy1.9	20.0
11	J0402.4-1807	ESO549-49	04:02:25.680	-18:02:52.800	0.026	43.5	Sy1.9	22.48
12	J1013.5-3601	Fairall1149	10:13:19.920	-35:58:57.720	0.028	43.6	Sy2	23.71
13	J1836.9-5924	Fairall49	18:36:58.296	-59:24:08.640	0.02	43.1	Sy1.9	22.03
14	J1844.5-6221	Fairall51	18:44:53.976	-62:21:53.280	0.014	43.2	Sy1.5	20.0
15	J0123.9-5846	Fairall9	01:23:45.792	-58:48:20.520	0.047	44.4	Sy1.2	20.0
16	J1419.0-1323	HB89_1416-129	14:19:03.816	-13:10:44.760	0.128	44.7	Sy1.2	–
17	J1614.1+2606	HB89_1612+261	16:14:13.200	+26:04:16.320	0.131	44.6	Sy1.5	–
18	J1145.6-1819	HE1143-1810	11:45:40.464	-18:27:15.480	0.032	44.0	Sy1.2	20.0
19	J1313.1-1108	HE1310-1051	13:13:05.784	-11:07:42.240	0.034	43.5	Sy1.5	20.0
20	J0231.6-3645	IC1816	02:31:51.000	-36:40:19.560	0.017	43.1	Sy1.8	23.87
21	J1349.3-3018	IC4329A	13:49:19.272	-30:18:33.840	0.016	44.1	Sy1.5	21.52
22	J1457.8-4308	IC4518A	14:57:41.184	-43:07:55.560	0.016	43.1	Sy2	23.36
23	J0800.1+2638	IC486	08:00:20.976	+26:36:48.600	0.026	43.7	Sy1.9	22.06
24	J2052.0-5704	IC5063	20:52:02.352	-57:04:07.680	0.011	43.2	Sy2	23.56
25	J0521.0-2522	IRAS05189-2524	05:21:01.464	-25:21:45.360	0.042	43.6	Sy2	22.92
26	J2325.5-3827	IRAS23226-3843	23:25:24.192	-38:26:49.200	0.035	43.6	Sy2	20.0
27	J0524.1-1210	LEDA17233	05:24:06.936	-12:10:08.760	0.049	44.0	Sy1.5	20.0
28	J0911.2+4533	LEDA2265450	09:11:29.976	+45:28:05.880	0.026	43.4	Sy2	23.52
29	J2123.6+2506	LEDA66688	21:23:44.592	+25:04:27.120	0.101	44.6	Sy1.9	23.01
30	J2028.5+2543	MCG+04-48-002	20:28:35.064	+25:43:59.880	0.013	43.5	Sy2	–
31	J1303.8+5345	MCG+09-21-96	13:03:59.472	+53:47:30.120	0.029	43.8	Sy1.5	20.0
32	J0920.8-0805	MCG-1-24-12	09:20:46.248	-08:03:21.960	0.019	43.6	Sy2	22.81
33	J0438.2-1048	MCG-2-12-50	04:38:14.184	-10:47:45.240	0.036	43.7	Sy1.2	20.9
34	J1322.2-1641	MCG-3-34-64	13:22:24.456	-16:43:42.960	0.016	43.2	Sy1.9	23.8
35	J0947.6-3057	MCG-5-23-16	09:47:40.152	-30:56:56.040	0.008	43.5	Sy1.9	22.18
36	J1335.8-3416	MCG-6-30-15	13:35:53.784	-34:17:44.160	0.007	42.8	Sy1.9	20.85
37	J0300.1+3674	Mrk1066	02:59:58.584	+36:49:14.160	0.012	42.5	Sy2	–
38	J1344.7+5588	Mrk273	13:44:42.120	+55:53:12.480	0.037	43.2	Sy2	–
39	J0747.5+6057	Mrk10	07:47:29.136	+60:56:00.600	0.029	43.4	Sy1.5	20.53
40	J0206.2-0019	Mrk1018	02:06:15.984	-00:17:29.040	0.042	44.0	Sy1.2	20.0
41	J0925.0+5218	Mrk110	09:25:12.864	+52:17:10.680	0.035	44.2	Sy1.5	20.0
42	J0804.2+0507	Mrk1210	08:04:05.856	+05:06:49.680	0.013	43.3	Sy1.9	23.4
43	J1506.7+0353A	Mrk1392	15:05:56.640	+03:42:25.200	0.036	43.7	Sy1.5	20.0
44	J0902.0+6007	Mrk18	09:01:58.320	+60:09:07.200	0.011	42.6	Sy1.9	23.08
45	J1535.9+5751	Mrk290	15:35:52.368	+57:54:09.360	0.029	43.6	Sy1.5	20.0
46	J0615.8+7101	Mrk3	06:15:36.360	+71:02:15.000	0.013	43.7	Sy1.9	24.06
47	J1049.4+2258	Mrk417	10:49:30.936	+22:57:51.840	0.032	43.9	Sy2	23.9
48	J1355.9+1822	Mrk463	13:56:02.880	+18:22:19.560	0.05	43.7	Sy1.9	23.81
49	J1441.4+5341	Mrk477	14:40:38.088	+53:30:15.840	0.037	43.6	Sy1.9	23.52
50	J1223.7+0238	Mrk50	12:23:24.144	+02:40:44.760	0.023	43.4	Sy1	20.0
51	J2044.2-1045	Mrk509	20:44:09.744	-10:43:24.600	0.034	44.4	Sy1.2	20.0
52	J2200.9+1032	Mrk520	22:00:41.376	+10:33:07.920	0.026	43.7	Sy1	22.32
53	J0214.6-0049	Mrk590	02:14:33.600	-00:46:01.200	0.026	43.2	Sy1.5	20.0
54	J0926.2+1244	Mrk705	09:26:03.288	+12:44:03.480	0.029	43.5	Sy1.2	20.0
55	J1504.2+1025	Mrk841	15:04:01.200	+10:26:16.080	0.036	44.0	Sy1.2	20.0

Table C1: *continued.*

56	J2236.7-1233	Mrk915	22:36:46.512	-12:32:42.720	0.024	43.6	Sy1.9	20.0
57	J2304.8-0843	Mrk926	23:04:43.464	-08:41:08.520	0.046	44.7	Sy1.5	20.0
58	J0650.0+6085	NGC2273	06:50:08.664	+60:50:44.880	0.006	41.9	Sy2	–
59	J1017.8+7340	NGC3147	10:16:53.640	+73:24:02.520	0.009	42.2	Sy2	–
60	J0552.2-0727	NGC2110	05:52:11.376	-07:27:22.320	0.007	43.6	Sy2	22.94
61	J0042.9-2332	NGC235A	00:42:52.800	-23:32:27.600	0.022	43.7	Sy1.9	23.5
62	J0856.0+7812	NGC2655	08:55:37.728	+78:13:23.160	0.004	41.8	Sy2	23.56
63	J0945.6-1420	NGC2992	09:45:42.048	-14:19:35.040	0.007	42.6	Sy1.9	21.72
64	J1001.7+5543	NGC3079	10:01:57.792	+55:40:47.280	0.003	42.0	Sy2	24.56
65	J0959.5-2248	NGC3081	09:59:29.544	-22:49:34.680	0.008	43.0	Sy2	23.91
66	J1023.5+1952	NGC3227	10:23:30.576	+19:51:54.360	0.003	42.5	Sy1.5	20.95
67	J1048.4-2511	NGC3393	10:48:23.448	-25:09:43.560	0.012	42.9	Sy2	24.4
68	J1139.8+3157	NGC3786	11:39:42.480	+31:54:32.400	0.008	42.4	Sy1.9	22.36
69	J1206.2+5243	NGC4102	12:06:23.112	+52:42:39.240	0.002	41.7	Sy2	24.14
70	J1210.5+3924	NGC4151	12:10:32.568	+39:24:20.520	0.003	43.1	Sy1.5	22.71
71	J1219.4+4720	NGC4258	12:18:57.504	+47:18:14.400	0.001	41.1	Sy1.9	23.0
72	J1225.8+1240	NGC4388	12:25:46.752	+12:39:43.560	0.008	43.6	Sy2	23.52
73	J1235.6-3954	NGC4507	12:35:36.624	-39:54:33.480	0.011	43.7	Sy1.9	23.95
74	J1304.3-1022	NGC4939	13:04:14.400	-10:20:22.560	0.01	42.8	Sy2	23.29
75	J1304.3-0532	NGC4941	13:04:13.128	-05:33:05.760	0.004	41.8	Sy2	23.91
76	J1338.2+0433	NGC5252	13:38:15.960	+04:32:33.360	0.023	44.0	Sy2	22.43
77	J0123.8-3504	NGC526A	01:23:54.384	-35:03:55.440	0.019	43.7	Sy2	22.01
78	J1341.9+3537	NGC5273	13:42:08.328	+35:39:15.120	0.003	41.6	Sy1.5	20.59
79	J1413.2-0312	NGC5506	14:13:14.856	-03:12:27.000	0.006	43.3	Sy1.9	22.44
80	J1417.9+2507	NGC5548	14:17:59.544	+25:08:12.480	0.017	43.7	Sy1.5	20.69
81	J1442.5-1715	NGC5728	14:42:23.928	-17:15:11.520	0.009	43.2	Sy1.9	24.14
82	J1515.0+4205	NGC5899	15:15:03.240	+42:02:59.640	0.008	42.5	Sy2	23.03
83	J1652.9+0223	NGC6240	16:52:58.896	+02:24:03.240	0.024	43.9	Sy1.9	24.25
84	J1717.1-6249	NGC6300	17:16:59.472	-62:49:14.160	0.003	42.4	Sy2	23.31
85	J2148.3-3454	NGC7130	21:48:19.512	-34:57:04.320	0.016	43.0	Sy1.9	24.22
86	J2201.9-3152	NGC7172	22:02:01.920	-31:52:11.280	0.008	43.4	Sy2	22.91
87	J2303.3+0852	NGC7469	23:03:15.624	+08:52:26.400	0.016	43.6	Sy1.5	20.53
88	J2304.9+1220	NGC7479	23:04:56.664	+12:19:22.440	0.007	42.3	Sy1.9	24.16
89	J2318.4-4223	NGC7582	23:18:23.496	-42:22:14.160	0.005	42.6	Sy2	24.15
90	J2318.9+0013	NGC7603	23:18:56.616	+00:14:38.400	0.029	44.0	Sy1	20.0
91	J2328.9+0328	NGC7682	23:29:03.888	+03:31:59.880	0.017	43.0	Sy2	24.27
92	J0201.0-0648	NGC788	02:01:06.456	-06:48:55.800	0.013	43.5	Sy2	23.82
93	J0234.1+3233	NGC973	02:34:20.112	+32:30:20.160	0.016	43.4	Sy2	22.49
94	J0234.6-0848	NGC985	02:34:37.776	-08:47:15.360	0.043	44.1	Sy1.5	20.92
95	J1104.8+7689	PG1100+772	11:04:13.680	+76:58:58.080	0.311	45.2	Sy1	–
96	J1119.6+2136	PG1116+215	11:19:08.688	+21:19:18.120	0.176	44.9	Sy1	–
97	J0054.9+2524	PG0052+251	00:54:52.104	+25:25:37.920	0.155	44.9	Sy1.2	20.0
98	J0810.9+7602	PG0804+761	08:10:58.560	+76:02:42.000	0.1	44.6	Sy1	20.64
99	J1152.1-1122	PG1149-110	11:52:03.552	-11:22:24.240	0.049	43.9	Sy1.2	20.79
100	J1204.8+2758	PG1202+282	12:04:42.096	+27:54:11.880	0.165	44.8	Sy1.5	20.0
101	J2359.3-6058	PKS2356-61	23:59:04.368	-60:54:59.400	0.096	44.6	Sy2	23.16
102	J1238.6+0928	SDSSJ123843.43+092736.6	12:38:43.440	+09:27:36.720	0.082	44.3	Sy2	23.6
103	J2240.2+0801	UGC12138	22:40:17.040	+08:03:14.040	0.025	43.4	Sy1.5	20.0
104	J2341.8+3033	UGC12741	23:41:55.464	+30:34:54.480	0.017	43.1	Sy2	23.82
105	J0630.7+6342	UGC3478	06:32:47.160	+63:40:25.320	0.012	42.4	Sy1.2	21.18
106	J0655.8+3957	UGC3601	06:55:49.536	+40:00:00.720	0.017	43.0	Sy1.9	21.4
107	J0935.9+6120	UGC5101	09:35:51.648	+61:21:11.160	0.039	43.4	Sy1.9	24.28
108	J1204.9+3105	UGC7064	12:04:43.344	+31:10:38.280	0.025	43.2	Sy1.9	22.59
109	J0800.5+2327	Z118-36	07:59:53.472	+23:23:24.360	0.029	43.7	Sy1.9	22.22
110	J0923.7+2255	Z121-75	09:23:43.008	+22:54:32.400	0.032	43.9	Sy1.2	20.0
111	J1200.8+0650	Z41-20	12:00:57.912	+06:48:23.040	0.036	43.8	Sy2	22.9
112	J0453.4+0404	Z420-15	04:53:25.752	+04:03:41.760	0.029	43.7	Sy2	24.08

Table C2: The *Herschel* fluxes of our sample of 112 AGNs. A star is used to flag the fluxes of the two sources with potential IR blending. The symbol † is used to flag sources with potential issues in the FIR fluxes, as found to give inconsistent SEDs. A machine-readable version of this table is available in the supplementary material, or directly at <https://tinyurl.com/yah2os8v>.

ID ^a	F70 (mJy)	Flag70 ^b	F100 (mJy)	Flag100	F160 (mJy)	Flag160	F250 (mJy)	Flag250	F350 (mJy)	Flag350	F500 (mJy)	Flag500
1	71.62 ±3.79	P.S.	53.98 ±4.19	P.S.	39.61 ±10.07	P.S.	0.0	N/A	0.0	N/A	0.0	N/A
2	2265.97 ±157.88	P.S.	3105.46 ±221.24	P.S.	3313.94 ±127.05	P.S.	0.0	N/A	0.0	N/A	0.0	N/A
3	627.83 ±16.89	P.S.	0.0	N/A	1012.0 ±194.93	P.S.	565.99 ±28.3	Ext.	315.76 ±30.98	Ext.	108.7 ±13.9	P.S.
4	668.01 ±37.27	Ext.	0.0	N/A	1939.47 ±79.6	Ext.	1280.13 ±45.99	Ext.	680.99 ±37.55	Ext.	232.99 ±20.87	Ext.
5	6814.31 ±127.0	P.S.	0.0	N/A	7087.19 ±244.47	P.S.	2857.6 ±45.0	P.S.	1135.6 ±42.94	Ext.	398.1 ±25.5	P.S.
6	333.64 ±84.13	Ext.	0.0	N/A	0.0	N/A	496.83 ±43.64	Ext.	277.59 ±34.67	Ext.	0.0	N/A
7	8882.76 ±277.08	Ext.	0.0	N/A	22291.49 ±694.52	Ext.	11297.73 ±341.64	Ext.	5104.31 ±159.47	Ext.	1986.71 ±68.13	Ext.
8	657.55 ±104.09	Ext.	0.0	N/A	1781.32 ±168.65	Ext.	1117.38 ±44.04	Ext.	493.27 ±28.76	Ext.	183.68 ±19.49	Ext.
9	682.82 ±136.33	Ext.	0.0	N/A	2420.86 ±139.17	Ext.	1883.65 ±74.6	Ext.	1141.32 ±51.43	Ext.	408.69 ±39.05	Ext.
10	823.61 ±41.3	Ext.	0.0	N/A	1837.96 ±97.67	Ext.	790.15 ±31.8	Ext.	307.1 ±22.2	P.S.	115.4 ±24.5	P.S.
11	3182.12 ±104.56	Ext.	0.0	N/A	4263.46 ±233.01	P.S.	1784.0 ±24.3	P.S.	753.4 ±23.5	P.S.	275.2 ±18.3	P.S.
12	277.26 ±11.08	P.S.	0.0	N/A	571.31 ±85.98	Ext.	381.41 ±38.07	Ext.	225.8 ±26.85	Ext.	79.78 ±18.2	Ext.
13	3342.46 ±57.86	P.S.	0.0	N/A	2416.31 ±200.47	P.S.	911.4 ±16.8	P.S.	362.8 ±16.7	P.S.	115.7 ±12.5	P.S.
14	1978.48 ±37.49	P.S.	0.0	N/A	1850.87 ±275.21	Ext.	1095.25 ±48.77	Ext.	560.72 ±41.35	Ext.	188.38 ±26.96	Ext.
15	537.0 ±13.43	P.S.	0.0	N/A	602.51 ±76.62	Ext.	222.0 ±13.8	P.S.	134.91 ±19.84	Ext.	0.0	N/A
16	48.4 ±3.63	P.S.	52.6 ±4.83	P.S.	39.04 ±10.55	P.S.	0.0	N/A	0.0	N/A	0.0	N/A
17	217.36 ±5.77	P.S.	226.9 ±6.85	P.S.	193.42 ±13.73	P.S.	99.6 ±14.5	P.S.	0.0	N/A	0.0	N/A
18	247.09 ±23.45	Ext.	0.0	N/A	323.0 ±40.2	Ext.	196.82 ±34.72	Ext.	88.8 ±24.06	Ext.	0.0	N/A
19	95.44 ±4.74	P.S.	115.19 ±5.92	P.S.	115.86 ±11.25	P.S.	60.81 ±13.6	Ext.	0.0	N/A	0.0	N/A
20	1473.32 ±53.34	Ext.	0.0	N/A	2234.25 ±90.97	Ext.	1025.57 ±37.35	Ext.	408.32 ±20.63	Ext.	155.7 ±15.9	P.S.
21	1757.69 ±29.94	P.S.	0.0	N/A	1111.43 ±86.03	Ext.	466.46 ±32.8	Ext.	148.0 ±19.8	P.S.	76.02 ±14.48	Ext.
22	5018.5 ±99.12	P.S.	5459.2 ±172.0	P.S.	4524.83 ±329.64	P.S.	1778.1 ±534.4	P.S.	0.0	N/A	0.0	N/A
23	873.45 ±18.01	P.S.	0.0	N/A	1322.29 ±78.88	Ext.	699.88 ±32.56	Ext.	316.02 ±24.43	Ext.	141.82 ±19.92	Ext.
24	4350.88 ±98.47	P.S.	3675.55 ±117.41	Ext.	3630.35 ±127.94	Ext.	2082.23 ±72.82	Ext.	1013.02 ±41.93	Ext.	365.3 ±36.01	Ext.
25	13631.51 ±199.1	P.S.	11462.73 ±200.76	P.S.	6163.15 ±80.09	P.S.	2132.5 ±24.0	P.S.	775.8 ±21.3	P.S.	234.2 ±16.3	P.S.
26	594.61 ±18.09	P.S.	0.0	N/A	1209.42 ±217.01	P.S.	566.8 ±27.56	Ext.	242.63 ±20.17	Ext.	84.7 ±15.2	P.S.
27	346.95 ±9.28	P.S.	0.0	N/A	257.33 ±210.89	P.S.	101.2 ±21.3	P.S.	0.0	N/A	0.0	N/A
28	391.6 ±9.14	P.S.	0.0	N/A	453.2 ±179.41	P.S.	192.0 ±13.2	P.S.	63.5 ±10.8	P.S.	0.0	N/A
29	0.0	N/A	342.02 ±8.18	P.S.	239.11 ±9.81	P.S.	116.4 ±11.0	P.S.	0.0	N/A	0.0	N/A
30	9487.38 ±285.88	Ext.	13327.03 ±402.08	Ext.	11081.33 ±235.38	P.S.	4021.8 ±51.9	P.S.	1566.1 ±49.6	P.S.	537.9 ±35.2	P.S.
31	55.07 ±9.92	P.S.	0.0	N/A	82.79 ±25.63	Ext.	79.2 ±13.9	P.S.	49.4 ±14.0	P.S.	0.0	N/A
32	583.45 ±15.59	P.S.	0.0	N/A	993.48 ±88.24	Ext.	687.73 ±51.2	Ext.	433.11 ±26.51*	Ext.	135.67 ±17.34*	Ext.
33	617.45 ±39.98	Ext.	0.0	N/A	1542.92 ±94.47	Ext.	817.48 ±39.88	Ext.	351.21 ±26.31	Ext.	150.5 ±17.3	P.S.
34	4907.67 ±81.65	P.S.	4238.88 ±108.02	P.S.	2981.59 ±60.92	P.S.	1109.34 ±41.59	Ext.	445.14 ±39.85	Ext.	138.7 ±13.5	P.S.
35	1463.42 ±24.43	P.S.	0.0	N/A	444.96 ±207.36	P.S.	136.9 ±14.1	P.S.	57.1 ±11.6	P.S.	0.0	N/A
36	1177.27 ±20.6	P.S.	0.0	N/A	734.22 ±198.38	P.S.	244.2 ±11.7	P.S.	95.6 ±14.8	P.S.	0.0	N/A
37	11861.34 ±214.01	P.S.	11891.23 ±215.86	P.S.	7848.65 ±150.21	P.S.	3047.5 ±38.6	P.S.	1265.5 ±29.1	P.S.	326.12 ±25.49	Ext.
38	24697.31 ±412.91	P.S.	22529.92 ±436.89	P.S.	12759.0 ±188.18	P.S.	4509.0 ±52.4	P.S.	1616.7 ±30.8	P.S.	507.2 ±22.0	P.S.
39	752.54 ±52.65	Ext.	0.0	N/A	1997.79 ±110.46	Ext.	1318.46 ±49.91	Ext.	702.1 ±33.68	Ext.	279.25 ±29.83	Ext.

Table C2: continued.

40	77.32 ±8.3	P.S.	0.0	N/A	108.42 ±40.62†	Ext.	202.71 ±26.61†	Ext.	146.67 ±21.59†	Ext.	0.0	N/A
41	102.41 ±4.94	P.S.	110.03 ±23.36	Ext.	104.98 ±10.3	P.S.	0.0	N/A	0.0	N/A	0.0	N/A
42	1487.92 ±26.3	P.S.	1135.12 ±33.5	P.S.	833.92 ±40.27	Ext.	337.42 ±23.78	Ext.	142.59 ±16.4	Ext.	0.0	N/A
43	305.6 ±14.14	P.S.	0.0	N/A	816.88 ±85.99	Ext.	561.92 ±26.9	Ext.	222.6 ±22.88	Ext.	108.3 ±16.6	P.S.
44	2397.64 ±52.47	P.S.	0.0	N/A	2200.01 ±209.44	P.S.	809.0 ±16.5	P.S.	336.9 ±15.0	P.S.	128.8 ±16.7	P.S.
45	170.38 ±4.82	P.S.	167.96 ±4.86	P.S.	127.2 ±23.19	Ext.	50.8 ±11.2	P.S.	0.0	N/A	0.0	N/A
46	2966.8 ±76.61	P.S.	2733.42 ±89.14	Ext.	2076.72 ±71.36	Ext.	1254.61 ±56.79	Ext.	747.55 ±48.34	Ext.	320.61 ±32.9	Ext.
47	117.42 ±9.52	P.S.	0.0	N/A	144.04 ±34.93	Ext.	52.9 ±12.3	P.S.	0.0	N/A	0.0	N/A
48	0.0	N/A	0.0	N/A	0.0	N/A	475.49 ±45.99	Ext.	259.1 ±28.11	Ext.	89.77 ±21.24	Ext.
49	1310.46 ±24.42	P.S.	0.0	N/A	750.47 ±249.16	P.S.	245.2 ±39.2	P.S.	92.3 ±21.8	P.S.	0.0	N/A
50	31.77 ±8.21	P.S.	0.0	N/A	146.62 ±163.19	P.S.	67.85 ±14.73	Ext.	0.0	N/A	0.0	N/A
51	1515.77 ±26.68	P.S.	0.0	N/A	1166.65 ±202.57	P.S.	407.0 ±12.4	P.S.	154.7 ±13.5	P.S.	50.91 ±22.24	Ext.
52	5305.51 ±94.29	P.S.	7008.37 ±159.28	P.S.	5836.3 ±102.8	P.S.	0.0	N/A	0.0	N/A	0.0	N/A
53	761.12 ±70.23	Ext.	0.0	N/A	2059.7 ±94.79	Ext.	1629.05 ±62.33	Ext.	690.74 ±38.98	Ext.	243.39 ±20.44	Ext.
54	691.82 ±18.92	P.S.	926.81 ±41.59	Ext.	997.4 ±46.62	Ext.	412.4 ±13.9	P.S.	216.69 ±18.26	Ext.	83.0 ±13.0	P.S.
55	452.04 ±6.81	P.S.	342.8 ±7.12	P.S.	175.11 ±7.71	P.S.	62.54 ±18.37	Ext.	0.0	N/A	0.0	N/A
56	427.3 ±12.25	P.S.	0.0	N/A	530.01 ±35.84	Ext.	319.55 ±23.16	Ext.	162.21 ±15.65	Ext.	56.0 ±11.4	P.S.
57	510.17 ±15.73	P.S.	0.0	N/A	581.33 ±182.44	P.S.	292.58 ±19.68	Ext.	0.0	N/A	0.0	N/A
58	6822.39 ±135.54	P.S.	8233.25 ±249.86	Ext.	6557.12 ±202.31	Ext.	3526.01 ±114.76	Ext.	1893.03 ±73.23	Ext.	790.46 ±46.93	Ext.
59	0.0	N/A	27067.38 ±832.57	Ext.	36216.72 ±1094.43	Ext.	22197.97 ±669.01	Ext.	9318.01 ±282.82	Ext.	3153.38 ±97.4	Ext.
60	4524.0 ±108.87	P.S.	5653.83 ±172.44	Ext.	4466.71 ±141.21	Ext.	1783.26 ±63.09	Ext.	803.14 ±39.46	Ext.	275.35 ±28.4	Ext.
61	2221.3 ±46.46	P.S.	2760.78 ±74.32	P.S.	2411.91 ±46.74	P.S.	978.1 ±17.6	P.S.	359.4 ±22.3	P.S.	120.7 ±16.5	P.S.
62	1485.19 ±55.13†	Ext.	0.0	N/A	3780.54 ±165.74†	Ext.	3620.56 ±130.55†	Ext.	1895.2 ±89.37†	Ext.	718.39 ±51.81†	Ext.
63	7584.4 ±228.99	Ext.	10582.98 ±319.49	Ext.	9634.67 ±291.7	Ext.	4607.98 ±145.56*	Ext.	2074.97 ±73.57*	Ext.	722.68 ±37.74*	Ext.
64	62787.22 ±1892.78	Ext.	104497.33 ±3137.39	Ext.	104713.92 ±148.61	Ext.	48766.07 ±146.82	Ext.	20556.37 ±620.9	Ext.	7304.8 ±225.69	Ext.
65	2657.71 ±96.28	Ext.	3926.73 ±132.9	Ext.	4253.1 ±154.34	Ext.	2060.92 ±71.64	Ext.	1154.4 ±55.33	Ext.	468.16 ±37.22	Ext.
66	10408.74 ±360.41	Ext.	16031.66 ±517.7	Ext.	21636.26 ±657.78	Ext.	11198.84 ±340.06	Ext.	4744.5 ±152.88	Ext.	1541.02 ±59.88	Ext.
67	2648.4 ±148.85	Ext.	0.0	N/A	3912.02 ±194.72	Ext.	2631.75 ±94.94	Ext.	1167.9 ±52.67	Ext.	415.31 ±33.51	Ext.
68	2176.33 ±75.38	Ext.	0.0	N/A	3263.88 ±123.76	Ext.	1819.63 ±136.25	Ext.	845.57 ±104.59	Ext.	296.5 ±42.85	Ext.
69	54423.17 ±990.29	P.S.	0.0	N/A	48356.71 ±1452.97	Ext.	19407.24 ±583.57	Ext.	7815.3 ±186.2	P.S.	2218.63 ±70.65	Ext.
70	6372.21 ±214.02	Ext.	6386.47 ±255.3	Ext.	8258.02 ±267.44	Ext.	4183.73 ±147.02	Ext.	1717.09 ±73.39	Ext.	561.39 ±40.73	Ext.
71	32032.0 ±1003.22†	Ext.	36930.02 ±1158.89†	Ext.	68761.55 ±2095.53†	Ext.	73721.28 ±2228.86†	Ext.	38636.37 ±1180.41†	Ext.	16519.72 ±539.66†	Ext.
72	10547.4 ±322.74	Ext.	19050.13 ±585.71	Ext.	17241.83 ±523.61	Ext.	7454.24 ±226.48	Ext.	3333.87 ±122.7	Ext.	1465.47 ±73.07	Ext.
73	3880.14 ±123.51	Ext.	0.0	N/A	5207.54 ±183.81	Ext.	2508.21 ±86.24	Ext.	1144.78 ±43.77	Ext.	403.11 ±28.3	Ext.
74	3387.58 ±446.11	Ext.	0.0	N/A	14409.16 ±522.54	Ext.	9134.39 ±283.99	Ext.	4467.41 ±146.34	Ext.	1669.03 ±75.98	Ext.
75	926.31 ±18.64†	P.S.	4113.46 ±159.82†	Ext.	7437.04 ±251.29†	Ext.	4855.01 ±158.49†	Ext.	2576.33 ±100.09†	Ext.	990.9 ±57.87†	Ext.
76	274.3 ±26.24	Ext.	0.0	N/A	533.17 ±77.0	Ext.	351.31 ±32.45	Ext.	244.34 ±52.62	Ext.	72.79 ±29.6	Ext.
77	224.1 ±14.24	P.S.	0.0	N/A	317.4 ±49.26	Ext.	195.99 ±22.73	Ext.	132.56 ±25.28	Ext.	0.0	N/A
78	730.04 ±16.39	P.S.	827.38 ±27.98	P.S.	682.52 ±44.99	Ext.	344.08 ±24.0	Ext.	173.06 ±19.62	Ext.	61.98 ±15.65	Ext.
79	8742.5 ±137.81	P.S.	8121.53 ±181.52	P.S.	6263.77 ±196.52	Ext.	2593.23 ±82.33	Ext.	1099.29 ±40.37	Ext.	359.91 ±25.39	Ext.
80	1088.84 ±24.15	P.S.	0.0	N/A	1367.32 ±81.47	Ext.	822.46 ±35.05	Ext.	330.61 ±22.57	Ext.	81.72 ±17.59	Ext.

Table C2: continued.

81	9810.3 ±304.15	Ext.	14317.62 ±434.9	Ext.	13560.22 ±411.57	Ext.	6426.08 ±198.83	Ext.	2889.97 ±97.56	Ext.	989.59 ±45.73	Ext.
82	5415.5 ±215.32	Ext.	0.0	N/A	13660.1 ±429.34	Ext.	7844.55 ±240.32	Ext.	3624.73 ±115.49	Ext.	1280.56 ±49.12	Ext.
83	25705.32 ±432.73	P.S.	25291.57 ±591.08	P.S.	17352.44 ±356.62	P.S.	6042.6 ±104.1	P.S.	2369.6 ±61.1	P.S.	823.3 ±35.4	P.S.
84	21965.1 ±717.76	Ext.	0.0	N/A	46698.04 ±1440.58	Ext.	29146.65 ±881.61	Ext.	12193.13 ±372.57	Ext.	4314.37 ±143.31	Ext.
85	17282.83 ±519.99	Ext.	0.0	N/A	18991.57 ±573.03	Ext.	7880.29 ±238.58	Ext.	3115.5 ±74.6	P.S.	1077.8 ±39.0	P.S.
86	7039.36 ±216.94	Ext.	0.0	N/A	12467.48 ±378.47	Ext.	5787.29 ±176.5	Ext.	2383.79 ±75.07	Ext.	764.9 ±34.65	Ext.
87	29631.73 ±570.24	P.S.	32226.92 ±799.23	P.S.	23237.99 ±437.32	P.S.	8488.2 ±127.5	P.S.	322.6 ±275.3	P.S.	1045.1 ±73.0	P.S.
88	13687.7 ±497.71	Ext.	22412.18 ±702.64	Ext.	30180.8 ±937.54	Ext.	16603.99 ±504.3	Ext.	7236.41 ±225.8	Ext.	2550.63 ±92.45	Ext.
89	65266.05 ±1961.67	Ext.	86531.98 ±2600.04	Ext.	73011.57 ±2195.44	Ext.	30022.6 ±904.64	Ext.	11795.95 ±359.2	Ext.	3726.09 ±126.51	Ext.
90	1260.55 ±26.02	P.S.	0.0	N/A	2346.1 ±241.63	P.S.	1205.2 ±19.5	P.S.	560.0 ±19.4	P.S.	207.8 ±9.8	P.S.
91	329.07 ±9.8†	P.S.	384.74 ±13.54†	P.S.	1177.68 ±76.78†	Ext.	693.87 ±61.45†	Ext.	489.31 ±44.28†	Ext.	266.15 ±32.57†	Ext.
92	523.51 ±13.7†	P.S.	0.0	N/A	699.01 ±76.12†	Ext.	806.18 ±43.3†	Ext.	378.57 ±37.63†	Ext.	137.09 ±18.58†	Ext.
93	0.0	N/A	3442.95 ±114.33	Ext.	5227.84 ±167.76	Ext.	3678.51 ±119.88	Ext.	1727.84 ±61.85	Ext.	712.64 ±38.44	Ext.
94	1279.18 ±47.47	Ext.	0.0	N/A	1936.74 ±89.06	Ext.	913.33 ±40.74	Ext.	437.16 ±35.68	Ext.	143.7 ±27.5	P.S.
95	73.62 ±5.99	P.S.	67.55 ±4.35	P.S.	49.38 ±9.03	P.S.	0.0	N/A	0.0	N/A	0.0	N/A
96	85.47 ±5.84	P.S.	59.3 ±6.05	P.S.	51.42 ±10.92	P.S.	0.0	N/A	0.0	N/A	0.0	N/A
97	74.43 ±4.43	P.S.	109.49 ±4.63	P.S.	145.89 ±12.41	P.S.	74.4 ±14.5	P.S.	40.8 ±13.2	P.S.	0.0	N/A
98	121.23 ±4.89	P.S.	79.58 ±4.0	P.S.	40.26 ±9.68	P.S.	0.0	N/A	0.0	N/A	0.0	N/A
99	231.45 ±5.71	P.S.	266.48 ±25.74	Ext.	271.52 ±13.28	P.S.	146.6 ±14.1	P.S.	76.5 ±12.2	P.S.	0.0	N/A
100	112.1 ±5.55	P.S.	100.08 ±5.52	P.S.	73.22 ±14.34	P.S.	0.0	N/A	0.0	N/A	0.0	N/A
101	0.0	N/A	79.93 ±3.6	P.S.	52.19 ±8.65	P.S.	29.8 ±9.4	P.S.	0.0	N/A	0.0	N/A
102	132.96 ±6.22	P.S.	122.72 ±3.96	P.S.	116.42 ±10.78	P.S.	52.8 ±13.3	P.S.	0.0	N/A	0.0	N/A
103	914.91 ±21.25	P.S.	0.0	N/A	891.72 ±83.68	Ext.	496.54 ±29.93	Ext.	195.18 ±19.33	Ext.	77.5 ±20.27	Ext.
104	384.58 ±15.52	P.S.	0.0	N/A	880.76 ±66.94	Ext.	525.83 ±27.73	Ext.	259.88 ±18.35	Ext.	106.37 ±16.59	Ext.
105	1470.84 ±55.85	Ext.	0.0	N/A	3724.4 ±162.52	Ext.	2097.58 ±71.12	Ext.	966.5 ±36.72	Ext.	354.13 ±22.15	Ext.
106	379.6 ±14.47	P.S.	0.0	N/A	599.33 ±202.84	P.S.	313.11 ±22.75	Ext.	143.02 ±20.35	Ext.	47.2 ±10.7	P.S.
107	15435.64 ±224.92	P.S.	0.0	N/A	15250.53 ±314.32	P.S.	6528.8 ±68.4	P.S.	2560.1 ±50.9	P.S.	810.4 ±28.3	P.S.
108	1459.04 ±51.33	Ext.	0.0	N/A	2517.27 ±97.75	Ext.	1185.32 ±61.66	Ext.	549.79 ±61.15	Ext.	198.6 ±42.7	P.S.
109	1857.35 ±62.87	Ext.	0.0	N/A	4062.07 ±158.47	P.S.	1989.5 ±32.0	P.S.	889.8 ±24.6	P.S.	340.9 ±23.2	P.S.
110	147.48 ±23.69	Ext.	0.0	N/A	350.79 ±75.45	Ext.	376.38 ±25.78	Ext.	159.85 ±14.11	Ext.	58.38 ±6.75	Ext.
111	540.11 ±12.44	P.S.	0.0	N/A	908.66 ±180.15	P.S.	443.6 ±13.3	P.S.	193.3 ±11.7	P.S.	63.0 ±12.5	P.S.
112	641.1 ±13.5	P.S.	0.0	N/A	614.15 ±210.49	P.S.	302.15 ±28.57	Ext.	213.13 ±20.86	Ext.	81.7 ±17.46	Ext.

^a ID of the source as in Table C1.

^b Indicates whether it is a point source (P.S.) or a spatially extended source (Ext.) at a given wavelength. The fluxes for point sources are from the HPDPs, and the fluxes for spatially extended sources have been re-calculated to include the extended flux (see Appendix A).

Table C3: The IR properties of our sample of 100 AGNs as derived using *iragnsep*. These are the sources selected to build our AGN templates (see § 3.2.3). A machine-readable version of this table is available in the supplementary material, or directly at <https://tinyurl.com/y86on7wk>.

ID ^a	S _{9.7} ^b	log ₁₀ (L _{IR} /L _⊙)	IR AGN _{frac}	SFR (M _⊙ yr ⁻¹)
1	0.385	10.801 ±0.003	0.843	6.969 ±0.043
2	0.24	10.399 ±0.002	0.28	2.733 ±0.009
3	0.0	10.443 ±0.001	0.622	3.024 ±0.01
4	0.5*	10.421 ±0.001	0.21	2.871 ±0.009
5	0.09	10.724 ±0.002	0.32	5.779 ±0.021
6	0.035	9.932 ±0.001	0.54	0.931 ±0.003
7	2.0*	10.131 ±0.001	0.13	1.474 ±0.005
8	1.5*	10.355 ±0.001	0.58	2.47 ±0.008
10	0.0	9.844 ±0.001	0.36	0.762 ±0.002
11	0.649	10.985 ±0.002	0.08	10.528 ±0.041
12	0.0	10.018 ±0.001	0.65	1.137 ±0.004
13	0.237	10.61 ±0.002	0.59	4.444 ±0.015
14	0.0	10.116 ±0.001	0.62	1.424 ±0.005
15	0.0	10.352 ±0.002	0.87	2.454 ±0.008
16	0.0	10.454 ±0.001	0.684	3.109 ±0.009
17	0.0	10.964 ±0.002	0.73	10.044 ±0.037
18	0.0	9.952 ±0.002	0.64	0.976 ±0.003
19	0.0	9.501 ±0.002	0.85	0.346 ±0.001
20	0.5*	10.222 ±0.001	0.38	1.816 ±0.005
21	0.0	10.114 ±0.002	0.84	1.416 ±0.005
22	1.249	10.636 ±0.002	0.38	4.715 ±0.016
23	0.291	10.344 ±0.001	0.47	2.406 ±0.008
24	0.2*	9.934 ±0.001	0.86	0.936 ±0.003
25	0.494	11.961 ±0.003	0.31	99.684 ±0.666
26	0.137	10.493 ±0.002	0.18	3.389 ±0.012
27	0.0	9.973 ±0.002	0.912	1.065 ±0.005
28	1.0*	9.999 ±0.002	0.29	1.088 ±0.004
29	1.0*	11.012 ±0.002	0.682	11.54 ±0.043
30	1.203	10.759 ±0.002	0.04	6.261 ±0.025
31	0.0	9.326 ±0.001	0.52	0.231 ±0.001
33	0.02	10.529 ±0.001	0.32	3.684 ±0.012
34	0.122	10.479 ±0.002	0.71	3.286 ±0.011
35	0.5*	8.727 ±0.002	0.964	0.062 ±0.0
36	0.0	9.218 ±0.001	0.7	0.185 ±0.0
37	1.0*	10.799 ±0.001	0.124	6.871 ±0.008
38	3.5*	12.168 ±0.003	0.09	160.445 ±1.108
39	0.123	10.579 ±0.001	0.19	4.133 ±0.013
41	0.0	9.659 ±0.002	0.78	0.497 ±0.002
42	0.006	9.663 ±0.002	0.88	0.502 ±0.002
43	0.0	10.34 ±0.002	0.55	2.382 ±0.008
44	0.443	10.041 ±0.002	0.11	1.197 ±0.004
45	0.0	9.6 ±0.002	0.817	0.435 ±0.002
46	0.5*	9.899 ±0.001	0.87	0.864 ±0.003
47	0.0	9.438 ±0.002	0.877	0.296 ±0.001
48	0.43	10.599 ±0.001	0.92	4.328 ±0.014
49	0.154	10.638 ±0.002	0.61	4.847 ±0.021
50	0.0	9.005 ±0.002	0.66	0.11 ±0.0
51	0.004	10.708 ±0.002	0.63	5.562 ±0.019
52	0.623	11.134 ±0.002	0.13	14.826 ±0.061
53	0.0	10.512 ±0.001	0.32	3.54 ±0.011
54	0.0	10.308 ±0.001	0.546	2.221 ±0.007
55	0.0	10.272 ±0.003	0.77	2.041 ±0.014
56	0.0	9.816 ±0.001	0.723	0.716 ±0.002
57	0.0	10.514 ±0.002	0.66	3.52 ±0.013

Table C3: *continued.*

58	0.491	9.812 ± 0.002	0.49	0.708 ± 0.002
60	0.0	9.884 ± 0.002	0.28	0.834 ± 0.003
61	0.53	10.584 ± 0.002	0.3	4.18 ± 0.016
64	5.0*	10.381 ± 0.001	0.03	2.623 ± 0.008
65	0.0	9.677 ± 0.001	0.6	0.518 ± 0.002
66	0.314	9.61 ± 0.001	0.22	0.444 ± 0.001
67	0.244	10.222 ± 0.001	0.26	1.815 ± 0.006
68	0.261	9.747 ± 0.002	0.15	0.608 ± 0.002
69	1.129	9.91 ± 0.002	0.1	0.885 ± 0.003
70	0.0	9.191 ± 0.001	0.75	0.169 ± 0.001
72	0.774	10.379 ± 0.001	0.392	2.633 ± 0.008
73	0.0	10.254 ± 0.001	0.502	1.956 ± 0.006
76	0.02	9.815 ± 0.001	0.67	0.711 ± 0.002
77	0.0	9.41 ± 0.001	0.85	0.28 ± 0.001
78	0.3*	8.275 ± 0.001	0.37	0.021 ± 0.0
79	0.914	9.882 ± 0.003	0.69	0.83 ± 0.005
80	0.0	10.015 ± 0.001	0.65	1.129 ± 0.004
81	1.3*	10.494 ± 0.002	0.12	3.399 ± 0.012
82	1.0*	10.214 ± 0.001	0.05	1.786 ± 0.006
83	1.8*	11.706 ± 0.001	0.07	55.402 ± 0.077
84	1.5*	9.893 ± 0.001	0.22	0.852 ± 0.003
85	0.671	11.2 ± 0.002	0.13	17.295 ± 0.076
86	2.5*	10.287 ± 0.001	0.13	2.109 ± 0.007
87	0.317	11.389 ± 0.001	0.286	26.676 ± 0.09
88	2.244	10.402 ± 0.001	0.44	2.749 ± 0.009
89	0.778	10.854 ± 0.001	0.05	7.779 ± 0.025
90	0.0	10.671 ± 0.001	0.48	5.112 ± 0.016
93	0.963	10.444 ± 0.001	0.15	3.033 ± 0.01
94	0.0	10.956 ± 0.001	0.533	9.9 ± 0.032
95	0.0	11.272 ± 0.002	0.801	20.688 ± 0.078
96	0.0	10.596 ± 0.002	0.939	4.303 ± 0.019
97	0.0	10.874 ± 0.002	0.74	8.146 ± 0.036
98	0.0	10.379 ± 0.002	0.93	2.645 ± 0.012
99	0.0	10.063 ± 0.002	0.79	1.26 ± 0.004
100	0.0	10.856 ± 0.002	0.818	7.822 ± 0.032
101	0.494	10.031 ± 0.002	0.858	1.197 ± 0.005
102	0.0	10.287 ± 0.001	0.85	2.112 ± 0.007
103	0.186	10.238 ± 0.001	0.55	1.885 ± 0.006
104	0.65	9.729 ± 0.001	0.23	0.584 ± 0.002
105	0.159	10.011 ± 0.001	0.25	1.118 ± 0.004
106	0.0	9.625 ± 0.002	0.39	0.459 ± 0.002
107	2.5*	11.893 ± 0.002	0.16	85.158 ± 0.333
108	0.139	10.538 ± 0.002	0.39	3.766 ± 0.013
109	0.558	10.882 ± 0.001	0.12	8.297 ± 0.027
111	0.641	10.415 ± 0.002	0.4	2.832 ± 0.01
112	0.0	9.994 ± 0.001	0.87	1.075 ± 0.003

^a ID of the source as in Table C1.^b The absorption coefficient at 9.7 μm . A star indicates that it has been fixed prior to the fit.Table C4: The properties of our sample of 110 star-forming galaxies pre-selected based on $\text{EW}_{6.2\mu\text{m}}^{\text{PAH}}$ and WISE colours (see § 3.1.1). A machine-readable version of this table is available in the supplementary material, or directly at <https://tinyurl.com/ybe3ujdu>.

ID	aorkey ^a	Counterpart Name	R.A. (h:m:s)	Dec. (d:m:s)	z	$\text{EW}_{6.2\mu\text{m}}^{\text{PAH}}$ ^b	W1 - W2 ^c	Notes ^d
1	3756800	NGC7714	23:36:14.092	+02:09:18.518	0.00933	1.024	0.38	AGN?
2	3758080	NGC1097	02:46:19.098	-30:16:27.664	0.00424	0.585	0.33	SF
3	3856128	NGC1808	05:07:42.182	-37:30:44.962	0.00332	1.015	0.404	SF

Table C4: *continued.*

4	4340480	He2-10	08:36:15.220	-26:24:33.699	0.00291	1.411	0.422	Ambiguous
5	4344576	Mkn331	23:51:26.704	+20:35:10.467	0.01848	0.965	0.467	AGN?
6	4830976	NGC1140	02:54:33.520	-10:01:40.319	0.00501	0.977	0.178	Discarded
7	4934400	NGC2993	09:45:48.311	-14:22:04.883	0.00811	1.466	0.435	SF
8	9071872	NGC1222	03:08:56.767	-02:57:18.819	0.00808	1.01	0.393	Ambiguous
9	9072128	IC342	03:46:48.359	+68:05:47.827	0.0001	1.171	0.496	Discarded
10	9073152	NGC4676	12:46:10.082	+30:43:56.211	0.02206	1.183	0.241	Discarded
11	10508288	UGC02238	02:46:17.472	+13:05:44.511	0.02188	0.937	0.49	AGN?
12	10511616	NGC6285	16:58:24.064	+58:57:21.714	0.01898	2.383	0.277	AGN?
13	10512128	Zw453.062	23:04:56.484	+19:33:07.798	0.0251	0.922	0.403	SF
14	14080768	KUG1429+334	14:31:25.400	+33:13:49.825	0.02254	1.759	0.17	SF
15	14081024	KUG1433+353	14:35:18.219	+35:07:08.508	0.02851	0.777	0.274	SF
16	14081280	2MASX J14364122+3458239	14:36:41.254	+34:58:23.966	0.03021	1.186	0.144	SF
17	14081536	MCG+06-32-058	14:31:56.217	+33:38:32.993	0.03373	0.844	0.142	Discarded
18	14081792	WISEAJ143119.77+353417.3	14:31:19.790	+35:34:17.945	0.03467	2.628	0.206	SF
19	14082048	MCG+06-32-056	14:31:21.149	+35:37:21.815	0.03484	1.909	0.334	SF
20	14083840	WISEAJ143228.32+345838.5	14:32:28.348	+34:58:39.086	0.1312	1.144	0.357	AGN?
21	14126592	WISEAJ172220.26+590949.7	17:22:20.251	+59:09:49.787	0.17862	1.152	0.504	AGN?
22	14127616	WISEA J171542.02+591657.5	17:15:41.931	+59:16:57.883	0.11578	1.024	0.47	AGN?
23	14132480	WISEAJ142819.47+335150.0	14:28:19.545	+33:51:49.996	0.48882	2.121	0.364	SF
24	14132736	WISEA J142919.74+341505.9	14:29:19.761	+34:15:06.070	0.424	1.127	0.482	AGN?
25	14835968	MCG-03-04-014	01:10:08.960	-16:51:09.154	0.03514	1.267	0.425	SF
26	14836480	NGC0695	01:51:14.247	+22:34:55.773	0.03247	0.73	0.43	SF
27	14837504	NGC2342a	07:09:18.067	+20:38:09.729	0.0176	1.157	0.287	SF
28	14838272	NGC3110	10:04:02.095	-06:28:29.088	0.01686	1.345	0.374	SF
29	14839040	IC2810	11:25:45.070	+14:40:35.590	0.03417	1.017	0.424	SF
30	14839552	Mkn1490	14:19:43.282	+49:14:11.688	0.02574	1.024	0.471	AGN?
31	14840320	NGC6090	16:11:40.789	+52:27:26.191	0.03023	1.325	0.487	AGN?
32	14840832	NGC6286b/6285	16:58:23.998	+58:57:21.852	0.01898	1.73	0.277	AGN?
33	14841088	NGC6286	16:58:31.494	+58:56:12.624	0.01835	0.796	0.479	SF
34	14843136	CGCG052-037	16:30:56.528	+04:04:58.811	0.02449	1.479	0.418	AGN?
35	15067904	WISEAJ085337.41+004409.9	08:53:37.456	+00:44:09.334	0.04092	0.911	0.412	AGN?
36	15069696	2MASXJ09194784+0231435	09:19:47.802	+02:31:43.194	0.08844	1.021	0.375	AGN?
37	16157696	WISEAJ143820.80+340234.0	14:38:20.720	+34:02:34.015	0.6736	0.956	0.164	SF
38	16158208	SDSSJ143151.84+324327.9	14:31:51.808	+32:43:27.715	0.66609	0.618	0.256	AGN?
39	16158976	WISEAJ143218.13+341259.6	14:32:18.142	+34:13:00.331	0.97777	1.074	0.246	SF
40	17470464	WISEA J161516.73+553046.6	16:15:16.758	+55:30:46.774	0.08328	2.17	0.367	SF
41	17470720	WISEAJ161645.38+550230.9	16:16:45.256	+55:02:30.760	0.08328	2.2	0.29	SF
42	17470976	WISEAJ161402.61+533036.5	16:14:02.618	+53:30:36.749	0.06343	1.311	0.22	SF
43	17538560	WISEAJ143631.97+335230.7	14:36:32.000	+33:52:30.549	0.0866	1.095	–	SF
44	17538816	WISEAJ143126.75+344517.3	14:31:26.733	+34:45:17.331	0.08275	1.611	0.265	SF
45	17863936	WISEAJ000024.24-525031.0	00:00:24.228	-52:50:30.949	0.12495	0.898	0.333	Discarded
46	18600448	WISEAJ083202.58+524714.2	08:32:02.435	+52:47:13.841	0.05865	1.098	0.12	SF
47	20310016	NGC5936	15:30:00.839	+12:59:22.011	0.01336	1.885	0.336	AGN?
48	20311296	ESO593-IG008	19:14:31.172	-21:19:06.107	0.04864	1.665	0.505	AGN?
49	20313088	MCG-02-01-051	00:18:50.855	-10:22:36.595	0.0271	1.403	0.465	AGN?
50	20316160	IRAS05442+1732	05:47:11.153	+17:33:46.792	0.01862	1.986	0.479	AGN?
51	20320768	ESO467-G027	22:14:39.880	-27:27:50.959	0.0174	0.603	0.268	SF
52	20323584	ESO286-G035	21:04:11.111	-43:35:34.685	0.01736	1.017	0.418	AGN?
53	20326656	ESO507-G070	13:02:52.390	-23:55:18.139	0.0217	1.035	0.46	AGN?
54	20327168	UGC11041	17:54:51.943	+34:46:34.208	0.01628	1.028	0.33	SF
55	20329216	IC0214	02:14:05.471	+05:10:24.592	0.03022	0.893	0.363	SF
56	20333056	IRASF03217+4022	03:25:05.379	+40:33:31.679	0.02337	1.321	0.46	AGN?
57	20334592	ESO069-IG006	16:38:11.847	-68:26:07.941	0.04697	1.309	0.503	AGN?
58	20337152	NGC0992	02:37:25.498	+21:06:04.018	0.01381	0.981	0.374	SF
59	20338176	NGC6907a	20:25:06.592	-24:48:32.833	0.01061	0.763	0.258	SF
60	20338432	UGC01845	02:24:08.015	+47:58:11.194	0.01561	2.453	0.348	AGN?
61	20339968	IRAS20351+2521	20:37:17.681	+25:31:38.595	0.0337	1.456	0.402	SF
62	20341760	NGC6701	18:43:12.495	+60:39:12.173	0.01323	0.869	0.276	SF
63	20342784	NGC0828	02:10:09.545	+39:11:24.737	0.01793	0.774	0.332	SF

Table C4: continued.

64	20347904	ESO264-G057	10:59:01.813	-43:26:25.451	0.0172	3.215	0.332	AGN?
65	20348672	NGC0023	00:09:53.415	+25:55:26.296	0.01523	0.814	0.216	SF
66	21650432	WISEAJ172611.94+592851.9	17:26:11.953	+59:28:51.830	0.07284	1.782	0.279	SF
67	21757696	WISEAJ143752.89+353251.1	14:37:52.906	+35:32:51.400	0.5628	0.905	0.401	AGN?
68	21926144	ESO540-G001	00:34:13.710	-21:26:19.861	0.02685	0.942	0.377	SF
69	22070528	WISEAJ010649.38+010323.0	01:06:49.349	+01:03:22.880	0.2535	0.761	0.397	AGN?
70	22081536	NGC3185	10:17:38.591	+21:41:17.005	0.00406	0.975	0.152	SF
71	22111744	NGC0838	02:09:38.520	-10:08:46.609	0.01284	1.472	0.389	AGN?
72	22123520	NGC4701	12:49:11.495	+03:23:16.976	0.00241	1.507	0.128	SF
73	22125056	WISEAJ132444.89+321442.5	13:24:44.901	+32:14:42.408	0.06001	0.902	0.4	AGN?
74	22128896	WISEAJ155616.05+395137.8	15:56:16.022	+39:51:37.884	0.07122	1.428	0.425	Ambiguous
75	22130176	UGC10407	16:28:28.015	+41:13:12.842	0.02833	0.809	0.318	AGN?
76	22133248	NGC4334	12:23:23.870	+07:28:24.764	0.01416	0.658	0.263	SF
77	23013120	SDSSJ032845.99+011150.8	03:28:45.985	+01:11:50.676	0.14216	2.624	0.279	SF
78	23013376	SDSSJ035733.99-053719.7	03:57:34.009	-05:37:19.827	0.20372	4.853	0.438	SF
79	23014656	SDSSJ082550.95+411710.2	08:25:50.951	+41:17:10.298	0.15615	1.333	0.449	SF
80	23016192	SDSSJ102613.97+484458.9	10:26:13.949	+48:44:58.737	0.16043	0.885	0.487	AGN?
81	23509760	WISEAJ091927.29+334727.1	09:19:27.283	+33:47:27.134	0.01927	0.975	0.26	SF
82	24142592	2MASSJ02260361-0459037	02:26:03.618	-04:59:03.983	0.055	1.312	0.222	AGN?
83	24142848	WISEAJ160408.31+545813.1	16:04:08.291	+54:58:13.048	0.06379	1.249	0.25	AGN?
84	24143616	SDSSJ105128.07+573502.4	10:51:28.059	+57:35:02.756	0.07315	1.326	0.206	AGN?
85	24146432	WISEAJ022602.92-045306.8	02:26:02.944	-04:53:06.966	0.05548	1.536	0.304	AGN?
86	24146688	2MASX J02254978-0400242	02:25:49.789	-04:00:24.930	0.04394	0.988	0.382	AGN?
87	24147200	2MASXJ02253645-0500123	02:25:36.434	-05:00:12.056	0.05397	1.773	0.309	SF
88	24148736	2MFGC13321	16:37:29.279	+40:52:48.210	0.02615	0.903	0.13	SF
89	24153088	WISEAJ103450.50+584418.2	10:34:50.508	+58:44:18.389	0.09128	1.17	0.342	AGN?
90	24154112	CGCG290-067	10:44:38.331	+56:22:10.623	0.02521	1.403	0.151	SF
91	24155136	KUG1632+414	16:34:01.798	+41:20:52.496	0.02837	1.666	0.105	AGN?
92	24155648	WISEJ163335.86+401528.9	16:33:35.870	+40:15:28.578	0.02781	1.149	0.237	AGN?
93	24158720	WISEAJ161929.54+541842.2	16:19:29.608	+54:18:41.677	0.09965	1.288	0.391	AGN?
94	24159744	WISEAJ163906.15+404003.3	16:39:06.149	+40:40:02.861	0.0347	2.09	0.139	SF
95	24160000	WISEAJ161823.10+552721.5	16:18:23.115	+55:27:21.742	0.08437	2.209	0.365	SF
96	24160512	WISEAJ161819.27+541859.3	16:18:19.336	+54:18:59.296	0.08274	1.225	0.247	SF
97	24160768	WISEAJ163705.29+413155.8	16:37:05.292	+41:31:55.535	0.12187	1.503	0.407	AGN?
98	24161792	WISEAJ163310.93+405641.1	16:33:10.906	+40:56:41.161	0.136	0.963	0.415	AGN?
99	24162048	WISEAJ162058.80+542513.2	16:20:58.821	+54:25:13.422	0.08274	1.055	0.249	SF
100	24163584	WISEAJ105005.96+561500.1	10:50:05.977	+56:15:00.000	0.11848	1.102	0.343	AGN?
101	24164864	WISEAJ022457.65-041417.8	02:24:57.641	-04:14:17.837	0.063	1.055	0.261	AGN?
102	24165376	WISEAJ021953.04-051824.0	02:19:53.030	-05:18:24.231	0.07351	1.652	0.303	SF
103	24166144	WISEAJ161301.83+552123.0	16:13:01.827	+55:21:23.121	0.012	1.19	0.024	AGN?
104	25278720	WISEAJ104901.42+592820.5	10:49:01.022	+59:28:21.521	0.0925	1.899	0.209	SF
105	25387520	WISEAJ163019.95+411132.4	16:30:19.980	+41:11:32.509	0.0929	0.852	0.278	SF
106	25800960	WISEAJ153253.77+302059.1	15:32:53.774	+30:20:59.583	0.36113	0.635	0.321	AGN?
107	27444736	WISEAJ101756.90+390528.0	10:17:56.807	+39:05:27.832	0.05389	0.658	0.333	AGN?
108	27445760	WISEAJ095912.41+022302.2	09:59:12.396	+02:23:02.585	0.704	1.098	0.028	SF
109	27451904	WISEAJ100157.45+024118.0	10:01:57.411	+02:41:18.074	0.659	1.463	–	SF
110	28144128	GALEXASCJ014202.93+213103.1	01:42:02.913	+21:31:02.773	0.0696	2.047	–	SF

^a aorkey of the source as referenced in the CASSIS database.

^b The $EW_{6.2\mu m}^{PAH}$ are from L19, and $EW_{6.2\mu m}^{PAH} > 0.54$ was used to pre-select star-forming galaxies.

^c The WISE colours are from L19 and $W1 - W2 \leq 0.5$ was also used to pre-select star-forming galaxies.

^d Notes on the source. Only sources flagged “SF” were kept in our final sample of pure star-forming galaxies, and used to build our galaxy templates. For the rest, “Discarded” means that an issue with the SED was found, “Ambiguous” are those sources for which we did not find any evidence of AGN contamination, yet could not be fit with the model of S18, and “AGN?” are sources that could not be fit with the model of S18 and for which we found potential AGN contamination (see Appendix B).

Table C5: The *Herschel* fluxes of our sample of 110 pre-selected star-forming galaxies. A star is used to flag the fluxes of sources with potential IR blending. A machine-readable version of this table is available in the supplementary material, or directly at <https://tinyurl.com/ybe3ujdu>.

ID ^a	F70 (mJy)	Flag70 ^b	F100 (mJy)	Flag100	F160 (mJy)	Flag160	F250 (mJy)	Flag250	F350 (mJy)	Flag350	F500 (mJy)	Flag500
1	9741.47 ±293.51	Ext.	10859.77 ±351.16	Ext.	7846.16 ±247.35	Ext.	0.0	N/A	N/A	N/A	0.0	N/A
2	76828.31 ±2322.1	Ext.	122960.04 ±3706.27	Ext.	132490.04 ±3981.52	Ext.	66667.01 ±2004.41	Ext.	28547.82 ±861.78	Ext.	9746.59 ±99.05	Ext.
3	132596.84 ±3943.52	Ext.	165345.79 ±4863.89	Ext.	144007.39 ±4322.35	Ext.	58112.6 ±1746.66	Ext.	22945.77 ±693.47	Ext.	7141.51 ±80.95	Ext.
4	24455.75 ±734.81	Ext.	25054.55 ±755.45	Ext.	18442.76 ±556.46	Ext.	6072.96 ±185.17	Ext.	2538.51 ±80.86	Ext.	872.16 ±6.01	Ext.
5	20726.44 ±372.34	P.S.	22639.5 ±509.78	P.S.	16445.94 ±268.48	P.S.	6168.0 ±66.2	P.S.	2340.4 ±47.7	P.S.	746.1 ±7.7	P.S.
6	3638.25 ±125.37*	Ext.	4622.39 ±153.62*	Ext.	3610.76 ±113.8*	Ext.	1681.69 ±57.34*	Ext.	920.21 ±39.69*	Ext.	310.3 ±28.7*	Ext.
7	11814.1 ±358.48	Ext.	13957.96 ±423.3	Ext.	9845.92 ±298.6	Ext.	3591.23 ±110.12	Ext.	1463.15 ±48.61	Ext.	485.84 ±22.89	Ext.
8	0.0	N/A	0.0	N/A	0.0	N/A	3263.17 ±99.99	Ext.	1291.47 ±44.07	Ext.	416.2 ±21.5	P.S.
9	413171.63 ±12453.92	Ext.	844468.61 ±25376.43	Ext.	1082509.83 ±32486.58	Ext.	563003.54 ±16903.49	Ext.	246628.98 ±7417.37	Ext.	91687.38 ±2770.32	Ext.
10	0.0	N/A	3678.14 ±121.51	Ext.	3735.29 ±123.46*	Ext.	1800.97 ±60.64*	Ext.	838.65 ±33.64*	Ext.	291.5 ±18.62*	Ext.
11	9026.45 ±271.59	Ext.	14416.78 ±439.79	Ext.	13319.61 ±405.15	Ext.	5772.4 ±76.1	P.S.	0.0	N/A	0.0	N/A
12	1898.6 ±34.01	P.S.	2713.33 ±114.8	Ext.	2644.67 ±68.16	P.S.	1128.5 ±27.1	P.S.	332.4 ±35.8	P.S.	0.0	N/A
13	8204.28 ±197.44	P.S.	9595.42 ±291.38	Ext.	8253.34 ±262.95	Ext.	3425.13 ±111.79	Ext.	1624.45 ±59.69	Ext.	551.8 ±27.9	Ext.
14	0.0	N/A	0.0	N/A	0.0	N/A	333.9 ±9.2	P.S.	164.0 ±10.4	P.S.	70.7 ±8.7	P.S.
15	0.0	N/A	5136.31 ±184.09	Ext.	4538.62 ±140.36	Ext.	1730.7 ±21.7	P.S.	724.6 ±20.2	P.S.	257.7 ±13.2	P.S.
16	0.0	N/A	771.1 ±101.35	Ext.	802.92 ±42.07	Ext.	510.33 ±22.88	Ext.	248.8 ±15.1	P.S.	116.4 ±11.3	P.S.
17	0.0	N/A	1780.73 ±147.36*	Ext.	2238.11 ±75.17*	Ext.	1246.48 ±41.23*	Ext.	597.21 ±24.92*	Ext.	230.54 ±20.03*	Ext.
18	0.0	N/A	0.0	N/A	0.0	N/A	285.0 ±9.6	P.S.	105.8 ±9.8	P.S.	37.6 ±6.6	P.S.
19	0.0	N/A	0.0	N/A	0.0	N/A	1223.4 ±14.9	P.S.	529.6 ±15.7	P.S.	187.2 ±14.5	P.S.
20	0.0	N/A	141.14 ±11.9	P.S.	226.06 ±40.7	P.S.	138.7 ±14.3	P.S.	80.1 ±13.2	P.S.	46.2 ±8.0	P.S.
21	0.0	N/A	274.22 ±15.69	P.S.	310.14 ±54.98	P.S.	170.1 ±11.7	P.S.	106.6 ±14.3	P.S.	40.6 ±9.5	P.S.
22	0.0	N/A	424.6 ±21.71	P.S.	388.0 ±42.83	P.S.	145.0 ±8.2	P.S.	69.7 ±8.1	P.S.	28.8 ±6.6	P.S.
23	0.0	N/A	42.91 ±9.57	P.S.	0.0	N/A	81.0 ±7.5	P.S.	55.6 ±7.9	P.S.	0.0	N/A
24	0.0	N/A	0.0	N/A	85.44 ±27.79	P.S.	50.3 ±5.2	P.S.	18.4 ±5.5	P.S.	0.0	N/A
25	8367.15 ±166.77	P.S.	10251.75 ±208.7	P.S.	8405.31 ±131.48	P.S.	3233.3 ±34.3	P.S.	1228.4 ±26.7	P.S.	399.5 ±17.6	P.S.
26	9256.07 ±281.05	Ext.	13383.34 ±412.76	Ext.	11048.89 ±338.09	Ext.	4165.31 ±127.38	Ext.	1655.57 ±53.45	Ext.	599.4 ±42.8	P.S.
27	9371.64 ±266.45	Ext.	13741.39 ±419.49	Ext.	13445.16 ±415.99	Ext.	5480.94 ±166.42	Ext.	2248.34 ±70.23	Ext.	690.32 ±27.97	Ext.
28	13558.34 ±382.03	Ext.	19229.21 ±577.94	Ext.	18330.77 ±553.27	Ext.	7091.48 ±214.26	Ext.	2915.1 ±97.42	Ext.	920.96 ±34.82	Ext.
29	5460.93 ±96.62	P.S.	7033.01 ±165.66	P.S.	5884.24 ±130.56	P.S.	2645.0 ±36.0	P.S.	0.0	N/A	0.0	N/A
30	7247.4 ±112.76	P.S.	8145.78 ±157.63	P.S.	5555.98 ±89.2	P.S.	2487.0 ±30.2	P.S.	0.0	N/A	0.0	N/A
31	6989.24 ±115.03	P.S.	7875.39 ±182.89	P.S.	6629.73 ±115.57	P.S.	3056.0 ±34.2	P.S.	1482.4 ±32.8	P.S.	0.0	N/A
32	1988.94 ±76.01	Ext.	2756.2 ±184.6	Ext.	2644.67 ±68.16	P.S.	1128.5 ±27.1	P.S.	332.4 ±35.8	P.S.	0.0	N/A
33	9801.34 ±296.11	Ext.	17933.23 ±545.74	Ext.	19132.78 ±576.62	Ext.	9172.78 ±298.34	Ext.	3710.49 ±129.69	Ext.	1289.5 ±47.0	P.S.
34	8195.54 ±129.34	P.S.	10536.99 ±227.09	P.S.	9231.61 ±153.4	P.S.	3713.6 ±39.9	P.S.	1433.1 ±42.4	P.S.	488.39 ±23.78	Ext.
35	0.0	N/A	1903.1 ±37.81	P.S.	1756.63 ±47.73	P.S.	752.8 ±16.9	P.S.	301.2 ±22.1	P.S.	98.0 ±18.7	P.S.
36	0.0	N/A	662.85 ±29.16	P.S.	747.74 ±41.47	P.S.	322.0 ±14.0	P.S.	139.1 ±14.8	P.S.	53.05 ±11.54	Ext.
37	0.0	N/A	0.0	N/A	0.0	N/A	272.2 ±8.6	P.S.	156.7 ±10.4	P.S.	53.7 ±10.6	P.S.
38	0.0	N/A	0.0	N/A	0.0	N/A	155.6 ±8.6	P.S.	89.8 ±11.8	P.S.	39.7 ±8.9	P.S.
39	0.0	N/A	71.66 ±8.8	P.S.	145.41 ±16.76	Ext.	96.7 ±6.5	P.S.	53.7 ±14.5	P.S.	0.0	N/A

Table C5: continued.

40	0.0	N/A	423.44 ±13.04	P.S.	379.0 ±34.67	P.S.	168.9 ±8.5	P.S.	64.2 ±9.8	P.S.	0.0	N/A
41	0.0	N/A	615.08 ±13.75	P.S.	662.86 ±35.63	P.S.	353.7 ±10.9	P.S.	160.4 ±12.5	P.S.	63.4 ±8.7	P.S.
42	0.0	N/A	579.76 ±13.07	P.S.	697.71 ±44.93	P.S.	359.1 ±8.9	P.S.	153.1 ±10.8	P.S.	64.1 ±13.2	P.S.
43	0.0	N/A	0.0	N/A	0.0	N/A	169.4 ±10.8	P.S.	68.9 ±11.3	P.S.	32.8 ±8.2	P.S.
44	0.0	N/A	204.74 ±11.41	P.S.	161.89 ±32.35	P.S.	84.5 ±9.3	P.S.	30.2 ±7.3	P.S.	0.0	N/A
45	0.0	N/A	0.0	N/A	0.0	N/A	888.0 ±17.7	P.S.	395.0 ±15.1	P.S.	145.2 ±16.4	P.S.
46	0.0	N/A	0.0	N/A	0.0	N/A	169.8 ±7.0	P.S.	95.9 ±9.1	P.S.	48.1 ±7.3	P.S.
47	10442.88 ±317.26	Ext.	16275.94 ±498.82	Ext.	14909.87 ±460.49	Ext.	6072.41 ±184.19	Ext.	2381.11 ±74.15	Ext.	744.0 ±42.7	P.S.
48	6848.52 ±209.49	Ext.	9279.32 ±281.44	Ext.	7924.85 ±139.66	P.S.	3255.2 ±40.5	P.S.	1151.38 ±39.82	Ext.	359.98 ±16.24	Ext.
49	6848.15 ±145.69	P.S.	7148.31 ±200.22	P.S.	5336.09 ±143.11	P.S.	1818.5 ±100.6	P.S.	692.9 ±99.9	P.S.	245.5 ±42.1	P.S.
50	10615.53 ±177.66	P.S.	11005.06 ±243.28	P.S.	7636.94 ±126.75	P.S.	2574.2 ±36.6	P.S.	930.4 ±31.6	P.S.	322.7 ±35.9	P.S.
51	6386.05 ±194.64	Ext.	10985.9 ±334.99	Ext.	11159.27 ±339.08	Ext.	4903.65 ±149.87	Ext.	1974.93 ±62.95	Ext.	759.67 ±31.32	Ext.
52	8208.41 ±205.18	P.S.	10617.41 ±323.45	Ext.	9460.71 ±178.91	P.S.	3752.2 ±61.7	P.S.	1356.36 ±46.17	Ext.	0.0	N/A
53	16344.42 ±233.21	P.S.	16738.41 ±308.17	P.S.	10419.19 ±152.23	P.S.	3802.7 ±46.5	P.S.	1425.6 ±30.7	P.S.	475.1 ±24.1	P.S.
54	6783.22 ±204.97	Ext.	10996.73 ±338.7	Ext.	10744.17 ±327.98	Ext.	4486.81 ±136.89	Ext.	1889.56 ±60.18	Ext.	669.4 ±27.1	P.S.
55	5289.38 ±167.17	Ext.	7241.93 ±260.51	Ext.	6067.5 ±194.95	Ext.	2234.8 ±71.23	Ext.	898.4 ±33.1	P.S.	344.1 ±33.0	P.S.
56	9132.19 ±150.0	P.S.	10468.63 ±217.13	P.S.	7818.35 ±110.71	P.S.	3150.5 ±38.6	P.S.	1204.1 ±32.4	P.S.	378.7 ±20.0	P.S.
57	9362.75 ±152.87	P.S.	12643.23 ±262.83	P.S.	10568.18 ±152.76	P.S.	4516.5 ±55.2	P.S.	1727.5 ±36.7	P.S.	568.8 ±27.8	P.S.
58	10620.18 ±319.41	Ext.	14756.94 ±446.26	Ext.	12849.17 ±389.57	Ext.	4957.24 ±150.69	Ext.	2024.16 ±63.58	Ext.	657.7 ±28.8	P.S.
59	18165.25 ±552.48	Ext.	30979.71 ±935.55	Ext.	31511.84 ±951.86	Ext.	15573.2 ±468.72	Ext.	6692.38 ±202.99	Ext.	2475.01 ±9.13	Ext.
60	12754.23 ±227.12	P.S.	16390.63 ±284.21	P.S.	13311.77 ±198.77	P.S.	5390.3 ±57.0	P.S.	2046.0 ±47.6	P.S.	646.0 ±4.4	P.S.
61	7098.39 ±218.19	Ext.	9184.79 ±292.44	Ext.	7049.68 ±212.69	Ext.	2704.97 ±82.78	Ext.	1089.3 ±29.2	P.S.	369.0 ±6.6	P.S.
62	12653.92 ±381.96	Ext.	19077.3 ±576.67	Ext.	16099.9 ±484.24	Ext.	6765.05 ±204.67	Ext.	2698.47 ±84.79	Ext.	0.0	N/A
63	13395.59 ±403.03	Ext.	22902.86 ±688.6	Ext.	24577.9 ±743.47	Ext.	10838.21 ±326.2	Ext.	4548.65 ±138.93	Ext.	1604.5 ±0.6	P.S.
64	6831.23 ±204.78	Ext.	10361.12 ±315.44	Ext.	10523.89 ±320.32	Ext.	4549.39 ±138.97	Ext.	1877.07 ±60.32	Ext.	738.56 ±0.07	Ext.
65	9124.74 ±275.32	Ext.	12989.78 ±393.03	Ext.	12172.11 ±376.12	Ext.	4792.84 ±145.68	Ext.	1923.01 ±60.7	Ext.	598.81 ±0.81	Ext.
66	0.0	N/A	298.1 ±151.57	Ext.	247.48 ±40.89	P.S.	135.5 ±7.8	P.S.	61.4 ±8.5	P.S.	31.45 ±0.83	Ext.
67	0.0	N/A	0.0	N/A	0.0	N/A	170.6 ±9.2	P.S.	93.4 ±8.9	P.S.	30.9 ±0.2	P.S.
68	4460.08 ±139.89	Ext.	0.0	N/A	6191.08 ±199.25	Ext.	3124.89 ±96.71	Ext.	1285.1 ±48.12	Ext.	367.7 ±8.4	P.S.
69	0.0	N/A	95.04 ±5.59	P.S.	80.54 ±12.48	P.S.	49.3 ±9.6	P.S.	0.0	N/A	0.0	N/A
70	0.0	N/A	0.0	N/A	0.0	N/A	2456.67 ±79.84	Ext.	1179.84 ±46.8	Ext.	460.87 ±2.76	Ext.
71	13609.17 ±411.84	Ext.	16929.43 ±521.21	Ext.	12225.91 ±370.85	Ext.	4518.3 ±138.36	Ext.	1768.73 ±57.1	Ext.	566.8 ±0.9	P.S.
72	0.0	N/A	5091.2 ±161.03	Ext.	5690.75 ±177.95	Ext.	3072.36 ±98.0	Ext.	1718.59 ±59.48	Ext.	885.16 ±2.45	Ext.
73	0.0	N/A	0.0	N/A	0.0	N/A	312.2 ±11.1	P.S.	126.1 ±10.5	P.S.	41.7 ±0.8	P.S.
74	0.0	N/A	0.0	N/A	0.0	N/A	371.3 ±21.6	P.S.	135.2 ±18.1	P.S.	50.8 ±0.5	P.S.
75	1720.41 ±69.22	Ext.	3041.65 ±105.84	Ext.	2459.83 ±100.89	Ext.	1078.77 ±39.59	Ext.	482.63 ±27.35	Ext.	215.64 ±0.99	Ext.
76	0.0	N/A	9437.41 ±336.09	Ext.	8549.14 ±262.02	Ext.	3987.9 ±122.69	Ext.	1712.73 ±55.58	Ext.	581.57 ±0.64	Ext.
77	35.45 ±1.97	P.S.	39.41 ±2.3	P.S.	31.42 ±9.86	P.S.	0.0	N/A	0.0	N/A	0.0	N/A
78	51.02 ±1.93	P.S.	56.79 ±2.66	P.S.	40.59 ±11.54	P.S.	0.0	N/A	0.0	N/A	0.0	N/A
79	42.42 ±1.73	P.S.	54.87 ±2.08	P.S.	44.31 ±6.03	P.S.	0.0	N/A	0.0	N/A	0.0	N/A
80	50.19 ±2.43	P.S.	55.82 ±3.84	P.S.	46.42 ±7.11	P.S.	0.0	N/A	0.0	N/A	0.0	N/A

Table C5: continued.

81	0.0	N/A	0.0	N/A	0.0	0.0	N/A	972.8 ±18.0	P.S.	417.5 ±20.9	P.S.	148.4 ±15.3	P.S.
82	0.0	N/A	329.58 ±11.03	P.S.	423.62 ±27.78	0.0	P.S.	188.1 ±33.6	P.S.	82.9 ±15.4	P.S.	0.0	N/A
83	0.0	N/A	533.28 ±21.48	P.S.	496.95 ±33.22	0.0	P.S.	232.1 ±12.2	P.S.	94.3 ±12.0	P.S.	0.0	N/A
84	90.97 ±12.54	P.S.	120.45 ±12.06	P.S.	106.24 ±20.64	0.0	P.S.	52.6 ±6.3	P.S.	26.9 ±8.7	P.S.	0.0	N/A
85	0.0	N/A	114.43 ±11.31	P.S.	155.43 ±21.8	0.0	P.S.	64.1 ±7.7	P.S.	0.0	N/A	0.0	N/A
86	0.0	N/A	577.26 ±12.62	P.S.	475.67 ±34.81	0.0	P.S.	216.8 ±10.1	P.S.	73.4 ±9.9	P.S.	0.0	N/A
87	0.0	N/A	1319.22 ±92.64	Ext.	1199.16 ±37.42	0.0	P.S.	530.5 ±12.0	P.S.	233.25 ±16.02	Ext.	86.0 ±8	P.S.
88	0.0	N/A	679.75 ±19.08	P.S.	689.01 ±33.42	0.0	P.S.	311.1 ±9.4	P.S.	147.6 ±20.9	P.S.	0.0	N/A
89	0.0	N/A	0.0	N/A	267.08 ±24.24	0.0	P.S.	137.8 ±10.2	P.S.	67.7 ±14.8	P.S.	0.0	N/A
90	0.0	N/A	1919.42 ±283.67	Ext.	1334.84 ±30.28	0.0	P.S.	609.2 ±10.8	P.S.	256.1 ±14.4	P.S.	92.0 ±10.8	P.S.
91	0.0	N/A	547.71 ±16.44	P.S.	592.41 ±39.91	0.0	P.S.	305.82 ±16.23	Ext.	138.21 ±11.77	Ext.	52.85 ±9.38	Ext.
92	0.0	N/A	400.66 ±14.59	P.S.	513.61 ±29.56	0.0	P.S.	207.1 ±7.2	P.S.	101.2 ±7.8	P.S.	39.3 ±8.1	P.S.
93	0.0	N/A	339.86 ±13.41	P.S.	458.26 ±37.3	0.0	P.S.	272.4 ±19.2	P.S.	129.8 ±26.5	P.S.	0.0	N/A
94	0.0	N/A	168.23 ±17.51	P.S.	152.46 ±33.1	0.0	P.S.	95.5 ±7.1	P.S.	41.1 ±9.2	P.S.	0.0	N/A
95	0.0	N/A	584.73 ±17.73	P.S.	548.5 ±42.05	0.0	P.S.	256.0 ±8.5	P.S.	99.6 ±9.2	P.S.	0.0	N/A
96	0.0	N/A	695.37 ±14.84	P.S.	756.22 ±30.86	0.0	P.S.	383.6 ±6.9	P.S.	169.9 ±7.4	P.S.	47.1 ±7.4	P.S.
97	0.0	N/A	241.6 ±11.0	P.S.	372.41 ±38.94	0.0	P.S.	168.9 ±13.5	P.S.	82.1 ±12.6	P.S.	0.0	N/A
98	0.0	N/A	97.26 ±13.42	P.S.	129.65 ±41.52	0.0	P.S.	37.2 ±8.3	P.S.	0.0	N/A	0.0	N/A
99	0.0	N/A	538.14 ±15.47	P.S.	714.95 ±41.19	0.0	P.S.	368.4 ±12.4	P.S.	146.5 ±13.3	P.S.	42.9 ±10.5	P.S.
100	0.0	N/A	250.62 ±15.75	P.S.	183.67 ±36.58	0.0	P.S.	104.4 ±8.4	P.S.	52.8 ±8.2	P.S.	0.0	N/A
101	0.0	N/A	329.63 ±15.85	P.S.	397.61 ±40.38	0.0	P.S.	168.7 ±11.4	P.S.	87.6 ±12.4	P.S.	0.0	N/A
102	0.0	N/A	428.26 ±11.0	P.S.	364.89 ±37.16	0.0	P.S.	173.0 ±10.8	P.S.	74.4 ±10.6	P.S.	0.0	N/A
103	0.0	N/A	533.0 ±20.71	P.S.	519.56 ±32.06	0.0	P.S.	239.0 ±7.2	P.S.	101.4 ±7.1	P.S.	37.5 ±8.5	P.S.
104	0.0	N/A	0.0	N/A	392.48 ±23.92	0.0	P.S.	237.5 ±7.6	P.S.	117.1 ±11.6	P.S.	0.0	N/A
105	0.0	N/A	160.29 ±17.75	P.S.	167.59 ±33.92	0.0	P.S.	96.2 ±8.2	P.S.	44.1 ±7.5	P.S.	0.0	N/A
106	0.0	N/A	101.13 ±3.77	P.S.	125.12 ±7.14	0.0	P.S.	82.1 ±12.3	P.S.	41.9 ±12.8	P.S.	0.0	N/A
107	0.0	N/A	97.32 ±6.37	P.S.	108.3 ±13.92	0.0	P.S.	60.4 ±7.6	P.S.	30.5 ±7.8	P.S.	0.0	N/A
108	0.0	N/A	16.07 ±2.06	P.S.	25.73 ±6.52	0.0	P.S.	22.1 ±5.1	P.S.	0.0	N/A	0.0	N/A
109	0.0	N/A	28.57 ±2.51	P.S.	59.54 ±6.16	0.0	P.S.	59.8 ±8.1	P.S.	44.6 ±9.7	P.S.	0.0	N/A
110	0.0	N/A	50.08 ±5.5	P.S.	102.1 ±15.92	0.0	P.S.	46.1 ±8.4	P.S.	0.0	N/A	0.0	N/A

^a ID of the source as in Table C4.^b Indicates whether it is a point source (P.S.) or an extended source (Ext.) at a given wavelength. The fluxes for point sources are from the HPDP, and the fluxes for extended sources have been re-calculated to include the extended flux (see Appendix A).

This paper has been typeset from a \LaTeX file prepared by the author.

Table C6. The best fitting parameters of the model of S18 for our sample of 55 pure star-forming galaxies. A machine-readable version of this table is available in the supplementary material, or directly at <https://tinyurl.com/ybkypz94>.

ID ^a	$\log_{10}(M_{\text{dust}}/M_{\odot})$	T_{dust} (K)	$\log_{10}(M_{\text{PAH}}/M_{\odot})$	T_{PAH} (K)	$\tau_{9.7}$ ^b
2	9.613	26.37	9.641	63.825	1.416
3	9.665	31.493	9.812	14.54	2.47
7	9.471	33.992	9.577	18.732	1.68
13	10.103	29.542	10.381	32.63	7.0*
14	9.183	32.153	9.313	23.295	1.949
15	9.945	30.171	10.483	50.462	1.299
16	9.112	24.147	9.658	20.067	1.245
18	9.389	31.287	9.762	26.777	1.83
19	9.692	25.488	10.335	57.678	15.0*
23	10.565	23.737	11.289	29.541	0.392
25	10.626	33.491	10.869	14.837	2.653
26	10.52	31.496	10.933	42.753	1.758
27	9.98	29.866	10.097	15.971	2.534
28	9.971	28.347	10.184	30.026	5.0*
29	10.363	31.508	10.252	35.126	2.124
33	10.021	26.393	10.477	22.377	30.0*
37	11.94	35.427	11.997	19.931	20.0*
39	11.643	34.955	11.436	58.968	1.339
40	10.104	35.148	10.269	15.632	2.343
41	10.045	29.106	10.335	15.103	2.283
42	9.64	25.247	10.274	16.793	1.592
43	9.798	29.059	10.023	24.476	2.257
44	9.679	33.539	10.098	21.426	1.943
46	9.037	21.069	9.406	25.324	0.749
51	9.746	26.772	10.278	61.16	1.509
54	9.694	27.477	10.183	63.484	1.812
55	10.223	31.781	10.444	15.139	2.169
58	9.803	30.919	10.215	52.785	2.038
59	9.726	25.231	9.904	63.709	1.584
61	10.444	32.638	10.662	32.084	2.218
62	9.814	29.856	9.97	35.195	2.142
63	10.104	26.775	10.661	61.115	2.427
65	9.836	30.524	10.218	50.89	1.855
66	9.755	32.127	10.189	34.13	2.035
68	10.099	29.869	10.442	24.211	1.613
70	8.067	24.118	8.34	36.41	1.59
72	7.656	22.141	8.189	21.43	0.549
76	9.604	28.653	9.996	37.796	1.989
77	9.796	43.835	9.499	47.666	0.011
78	10.224	42.41	10.001	41.998	1.033
79	9.835	38.42	9.793	36.339	0.979
81	9.406	30.926	9.712	26.414	2.268
87	10.036	31.265	10.299	20.76	2.105
88	8.964	27.401	9.328	19.478	6.0*
90	9.455	31.279	9.687	36.823	2.505
94	8.62	26.393	9.117	22.912	1.369
95	9.989	29.873	10.545	19.164	2.357
96	9.995	27.08	9.843	23.777	2.257
99	9.857	25.242	10.525	16.653	1.498
102	9.735	30.159	10.156	28.824	1.731
104	9.632	22.628	10.045	32.576	1.46
105	9.489	27.113	9.781	24.969	1.392
108	10.719	33.626	11.237	39.105	2.552
109	10.761	25.788	11.338	32.098	2.25
110	8.622	21.556	9.313	25.185	0.0

^a ID of the source as in Table C4.^b Total optical depth at 9.7 μm . Values with a star have been fixed prior to the fit.